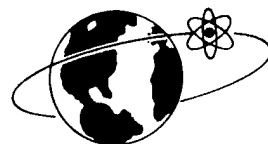


# SC-RR-68-132

SC-RR-68-132  
August 1968

**AEROSPACE  
NUCLEAR  
SAFETY**



## FREE-FALL ROTATION AND AERODYNAMIC MOTION OF RECTANGULAR PLATES

A. C. Bustamante, 9513  
Aerospace Nuclear Safety Department 9510

**DISTRIBUTION STATEMENT A**  
Approved for Public Release  
Distribution Unlimited

20011015 092

LOVELACE FOUNDATION  
DOCUMENT LIBRARY

**Reproduced From  
Best Available Copy**

# SANDIA LABORATORIES



OPERATED FOR THE UNITED STATES ATOMIC ENERGY COMMISSION BY SANDIA CORPORATION | ALBUQUERQUE, NEW MEXICO; LIVERMORE, CALIFORNIA

36345

Issued by Sandia Corporation,  
a prime contractor to the  
United States Atomic Energy Commission

### **LEGAL NOTICE**

This report was prepared as an account of Government sponsored work. Neither the United States, nor the Commission, nor any person acting on behalf of the Commission:

A. Makes any warranty or representation, expressed or implied, with respect to the accuracy, completeness, or usefulness of the information contained in this report, or that the use of any information, apparatus, method, or process disclosed in this report may not infringe privately owned rights; or

B. Assumes any liabilities with respect to the use of, or for damages resulting from the use of any information, apparatus, method, or process disclosed in this report.

As used in the above, "person acting on behalf of the Commission" includes any employee or contractor of the Commission, or employee of such contractor, to the extent that such employee or contractor of the Commission, or employee of such contractor prepares, disseminates, or provides access to, any information pursuant to his employment or contract with the Commission, or his employment with such contractor.

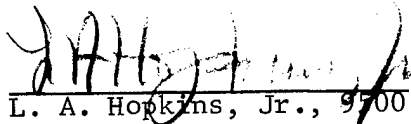
Printed in the United States of America  
Available from  
Clearinghouse for Federal Scientific and Technical Information  
National Bureau of Standards, U. S. Department of Commerce  
Springfield, Virginia 22151  
Price: Printed Copy \$3.00; Microfiche \$0.65

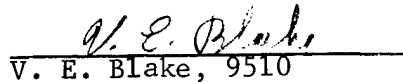
SC-RR-68-132

FREE-FALL ROTATION AND AERODYNAMIC MOTION  
OF RECTANGULAR PLATES

A. C. Bustamante, 9513  
Sandia Laboratories, Albuquerque

Approved by:

  
L. A. Hopkins, Jr., 9500

  
V. E. Blake, 9510

ABSTRACT

The aerodynamic motion of rectangular plates observed in 18 free-fall drop tests is analyzed and described. In most of the drops, the plates autorotated; the autorotation was independent of the plates' initial attitude. The autorotation generated a small lifting force which caused the plates to experience a gliding and spiraling motion.

August 1968

## SUMMARY

The aerodynamic motion of rectangular plates observed in 18 free-fall drop tests is analyzed and described. In most of the drops, the plate autorotated; the autorotation was independent of the plates' initial attitude. The autorotation generated a small lifting force which caused the plates to experience a gliding and spiraling motion.

The angular rate around the minimum inertia axis of each plate was obtained from camera data. A curve and the corresponding equation were used in fitting the data. The curves obtained indicate that the plates exhibited the typical characteristics of an autorotating body, with a peak buildup of angular rate and a decay to a steady-state value.

Trajectory data were obtained for all but two of the tests. Equations were derived which define the drag coefficient as a function of velocity. These equations indicate a decrease in drag coefficient with an increase in velocity. There was good agreement between the calculated velocities and the experimentally determined velocities; this was an additional indication that the plates experienced autorotational motion.

The maximum dispersion of the plates which were dropped from 2000 feet above terrain was within a circle 1000 feet in radius; the plates dropped from 10,000 feet above terrain were dispersed within a circle 6000 feet in radius. In general, the plates suffered little damage at impact, and most of them impacted on their longer side.

## TABLE OF CONTENTS

	<u>Page</u>
Introduction . . . . .	5
General Theory and Background . . . . .	5
Description of Tests . . . . .	8
Test Analysis and Discussion . . . . .	9
Aerodynamic Motion . . . . .	9
Drag Coefficients . . . . .	23
Velocity . . . . .	26
Altitude/Range Data . . . . .	27
Critical Reynolds Number . . . . .	32
Impact Characteristics . . . . .	32
Summary and Conclusions . . . . .	34
REFERENCES . . . . .	38
APPENDIX -- Methods Used in Obtaining Equations of Angular Rate Versus Time and of Drag Coefficient as a Function of Velocity . . . . .	39

## FREE-FALL ROTATION AND AERODYNAMIC MOTION OF RECTANGULAR PLATES

### Introduction

A study was undertaken to investigate the free-flight motion of rectangular plates because components having this configuration will reenter the earth's atmosphere as parts of radioisotopic power generators. For some of the planned missions, it is desired that these components survive the reentry environment and remain intact after impacting the earth's surface. It is necessary to know what free-flight motion the plates exhibit during the terminal phase of the flight in order to assess the plates structural integrity and trajectory characteristics. In addition, it is planned to investigate the free-flight motion of these configurations in a hypersonic environment.

The first part of the study was a drop-test program in which rectangular plates were freely dropped from altitudes of 2000 and 10,000 feet above terrain. These tests were conducted in order to obtain the aerodynamic motion and free-flight trajectory characteristics of the plates. The results and analysis of 18 drop tests conducted at the Tonopah Test Range in Nevada are presented.

### General Theory and Background

This study was undertaken to investigate the motion exhibited by a rectangular flat plate during free flight and to determine the dependence of this motion on initial conditions. Before proceeding into the actual study, it is worthwhile to present the general theory which describes the free motion such a plate should undergo. A flat rectangular plate in free flight will generally have a tumbling motion. Tumbling is defined in this report as a free body rotation, predominantly about an axis perpendicular to the airstream but not always because a combination of motions may often be discerned. However, it is felt that a rectangular flat plate would generally experience an autorotational

motion. In this report, autorotation is defined as rotation about a fixed axis which is perpendicular to the airstream. This rotation increases to a peak value and then achieves a steady state rate without the aid of an external force. Reference 1 gives an excellent treatment of tumbling motion and, therefore, no detailed theories or descriptions of this motion are given here. It is believed that a rectangular plate will continuously autorotate about an axis which is free in flight. This behaviour may be compared to the motion of a strip of paper of aspect ratio two or more. When dropped in still air, the strip rotates and descends along an inclined path. Aerodynamically, this motion may be explained by the fact that turbulent flow requires a certain time to form. This is illustrated by Figure 1.

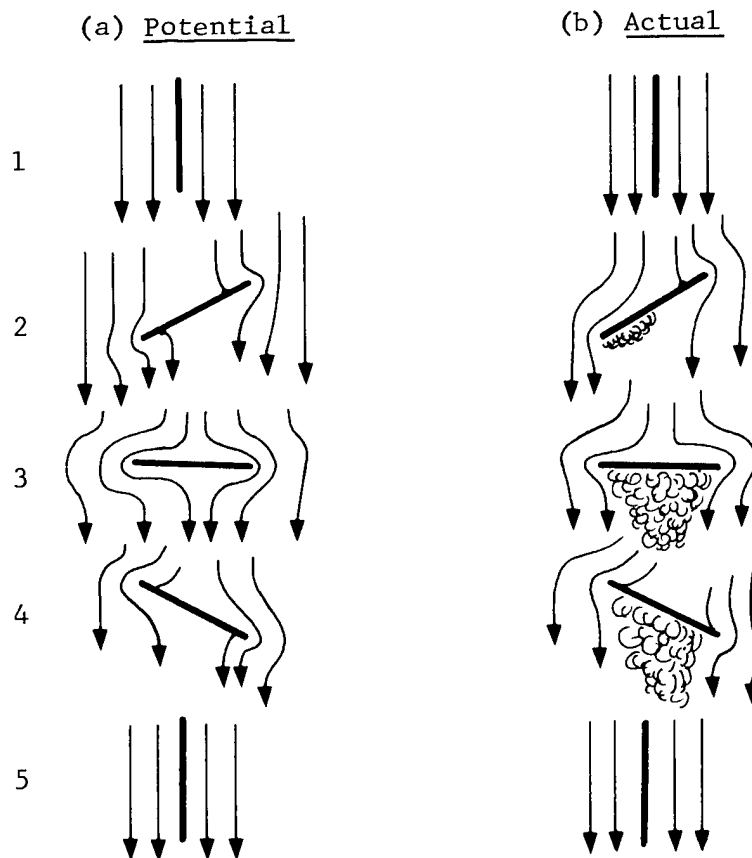


Figure 1. Comparison of potential and actual flow over a strip of paper

Potential flow is generally formed at the instant that flow begins over a body and it is so called because it can be calculated by use of the potential theory of aerodynamics. In Figure 1 (a), the steady-state potential flow around the strip is shown in five consecutive positions. In position (a)1 no torque is exerted by the flow on the strip. In position (a)2, the theoretical flow has two stagnation points, S, of no velocity and of maximum pressure. The position of the strip is such that the stream exerts a clockwise driving torque on the strip. The flow in position (a)3 is symmetrical, and no torque is exerted. Position (a)4 appears the same as position 2(a), but the torque is now acting counterclockwise and, since the strip is still rotating clockwise, amounts to a retarding torque. In the quarter revolution between (a)1 and (a)3, the flow performs positive work on the strip, but between (a)3 and (a)5, it performs exactly the same amount of negative work on it.

For potential flow where positions (a)2 and (a)4 are identical, the stream performs zero work during a full revolution, and neither damping nor self-excitation takes place. However, the actual flow differs from the potential flow and is shown in Figure 1(b). Between (b)1 and (b)3, turbulence behind the plate builds up gradually, and between (b)3 and (b)5 this turbulent air is washed away with the stream. Because of this, positions (b)2 and (b)4 differ; (b)2 resembles the potential-flow position much more than does (b)4. The effect of turbulence on the plates in position 2 is primarily to diminish the torque exerted by the stream on the plate. Similarly, in position (b)4 the retarding torque is less than that of (a)4, but the "less" is more pronounced in position 4 than in position 2. Therefore, there is more positive work performed between (b)1 and (b)3 than there is negative work between (b)3 and (b)5, and net positive work results from a full revolution. This gives rise to the self-excited rotation or "autorotation" of the plate.

Besides a torque, the flow also exerts a sidewise force on the plate. The flow in Figure 1 (b)2 resembles the flow around an airplane wing, and the plate experiences a lift force to the right. Similarly, in (b)4 there is a lift force to the left, but this force is smaller than (b)2 because the turbulence is much further developed ("stalled" airplane wing). Thus, there is a net lift force to the right during a full revolution. This explains the inclined fall of the paper strip.



The preceding discussion has provided a qualitative view of the existence of autorotation. This discussion is not complete because other forces can contribute to autorotation. This introduction into the autorotation phenomenon was presented so that the data presented in this report will be more easily understandable in terms of autorotation. The plates in this study have six-degrees-of-freedom available, and, consequently, their motion will not be purely autorotational but will be influenced by several possible impressed aerodynamic forces which can induce a complex motion, particularly when gyroscopic effects are added.

### Description of Tests

A total of 18 free-fall drop tests was conducted in which rectangular flat plates were freely dropped in various attitudes. These tests were conducted from altitudes of 2000 and 10,000 feet above terrain. A Kaman H-43 helicopter was used as the drop helicopter, and a Bell G3B helicopter was used for photographic coverage. During the test, the H-43 helicopter was flown at approximately zero air relative velocity, and the plates were dropped from the rear of the helicopter. This was done in order to minimize any initial disturbance or motions that might have been imparted to the plates by the downwash or wake of the helicopter. As a result of the precautions described above, it is believed that the initial motion of the plates were minimally influenced by the helicopter's wake or motion.

The tests were conducted at Sandia Laboratories' Tonopah Test Range, Tonopah, Nevada, which is quite heavily instrumented with ground cameras and radars. Both radar and ground optical tracking cameras were used to obtain trajectory and photographic data. In addition, the chase helicopter had a photographer on board who hand-tracked the drops with a 16-mm movie camera.

Two different rectangular plates were used: a 32- x 27- x 0.69-inch plate with hemicylindrical edges and a 48- x 18- x 0.50-inch plate with square edges. The physical characteristics, weights, and moments of inertia are shown in Table I.

TABLE I  
Physical Characteristics of Plates

<u>Dimensions</u> (inches)	<u>Weight</u> (lbs)	<u>Moments of Inertia</u>		
		<u>Ixx</u> (slug-ft <sup>2</sup> )	<u>Iyy</u> (slug-ft <sup>2</sup> )	<u>Izz</u> (slug-ft <sup>2</sup> )
No. 1 - 32 x 27 x 0.69	40±1/4	1.199	0.5098	0.693
No. 2 - 48 x 18 x 0.50	44±1/4	2.08	0.257	1.812

The test program was conducted in two separate series. In the first series, eight drop tests were conducted with Plate No. 1 on July 11 and 12, 1966. The plate was tricolored (black, yellow, and orange) to make it easily visible and to aid in obtaining angular rates (Figure 2). The second series was conducted on August 15 and 16, 1966; six drops were conducted with Plate No. 1 and four with Plate No. 2. Both plates had varicolored geometric designs to aid in tracking and obtaining angular rates (Figure 3). The plates were dropped 2000 and 10,000 feet and at seven different initial attitudes (Table II).

### Test Analysis and Discussion

#### Aerodynamic Motion

The main objectives of the test were to investigate the type of motion that a rectangular plate experiences in free flight and to determine if this motion is independent of the initial conditions or disturbances. Of secondary importance were the determination of the impact characteristics of a plate and its terminal velocity. The tests were conducted at Sandia Laboratories Tonopah Test Range in Nevada. Instrumentation consisted of optical range cameras for trajectory and photographic coverage; in addition, photographic data were provided by a chase helicopter. The motion on all 18 drop tests was analyzed by studying the film data. The plates were released in seven different attitudes, with some of the attitudes repeated. The two altitudes of release were 2000 and 10,000 feet above terrain.

In each test except Test No. 258-19, the plates went into an autorotational mode (see Table II). In Tests 258-13, -16, and -17, the plates were dropped in a flat attitude and remained in this attitude

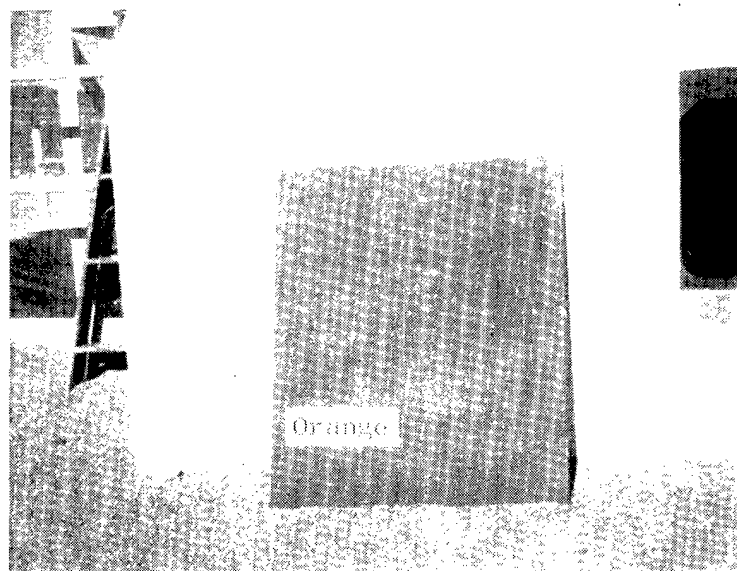
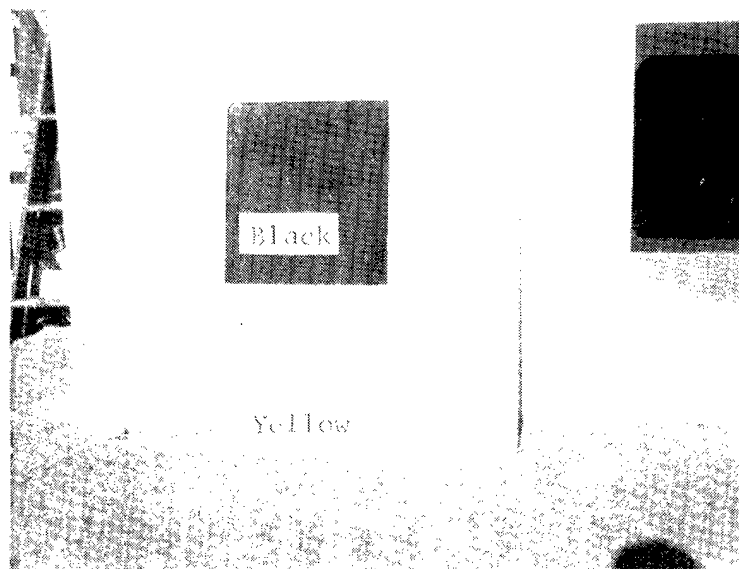


Figure 2. Color scheme for Plate No. 1  
(first test series)

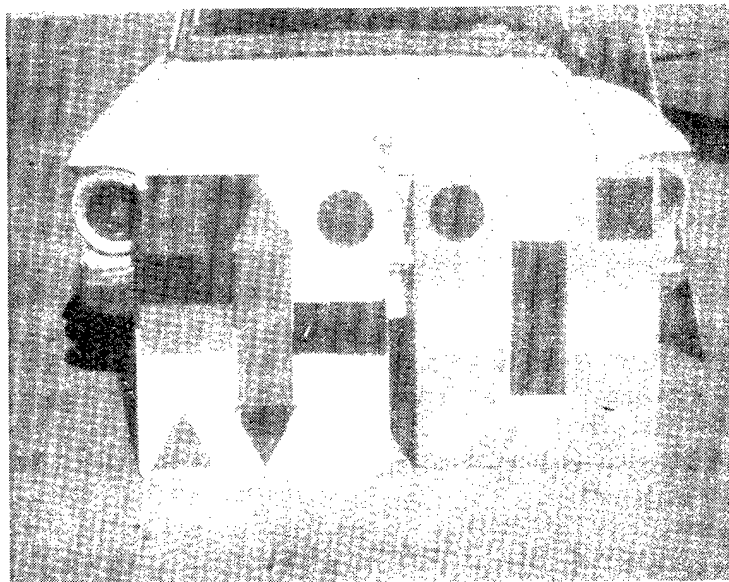


Plate No. 1

Colors: yellow, orange, black, green, white

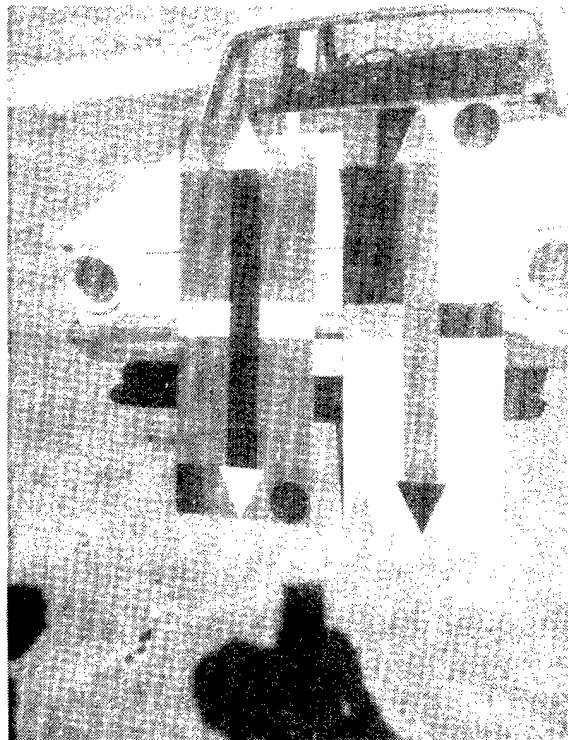
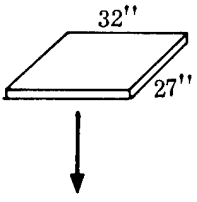
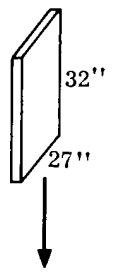
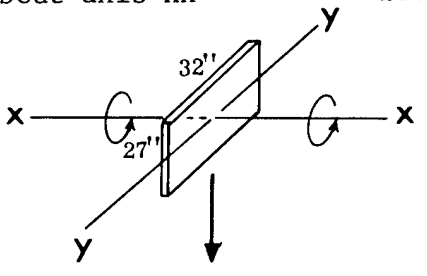
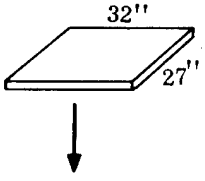


Plate No. 2

Figure 3. Color scheme for Plates Nos. 1 and 2  
(second test series)

TABLE II

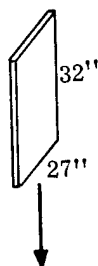
Test Summary

<u>Test No.</u>	<u>Initial Attitude</u>	<u>Altitude Above Terrain (ft)</u>	<u>Final Motion</u>
258-10	Flat	2000	Autorotating
			
258-11	Edge on	2000	Autorotating
			
258-12	Rotate plate about axis xx	2000	Autorotating
			
258-13	Flat	10,000	Flat till 90 seconds, then started autorotating
			

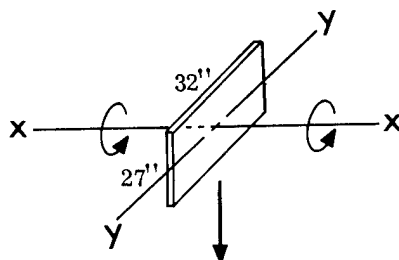
(continued on next page)

TABLE II (cont)

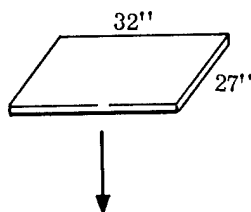
<u>Test No.</u>	<u>Initial Attitude</u>	<u>Altitude Above Terrain (ft)</u>	<u>Final Motion</u>
258-14	Edge on	10,000	Autorotating



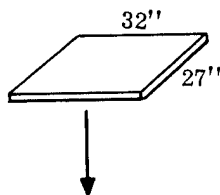
258-15	Rotate plate about axis xx	10,000	Autorotating
--------	----------------------------	--------	--------------



258-16	Flat	10,000	Flat till 50 seconds, then started auto-rotating
--------	------	--------	--

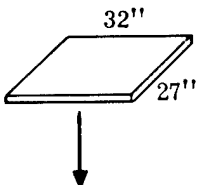
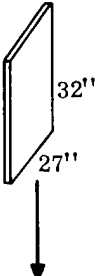
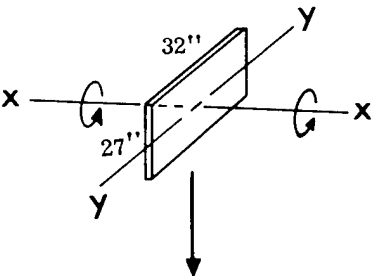
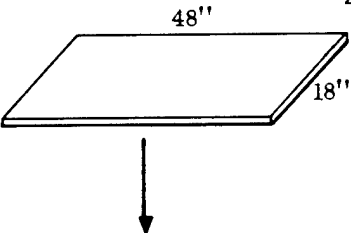


258-17	Flat	10,000	Flat till 55 seconds, then started auto-rotating
--------	------	--------	--



(continued on next page)

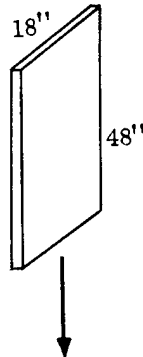
TABLE II (cont)

<u>Test No.</u>	<u>Initial Attitude</u>	<u>Altitude Above Terrain (ft)</u>	<u>Final Motion</u>
258-18	Flat	2000	Autorotating
			
258-19	Edge on	2000	Flat (broadside) till impact
			
258-20	Rotate plate about axis xx	2000	Autorotating
			
258-21	Flat	2000	Autorotating
			

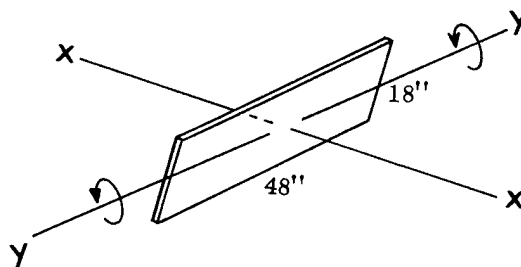
(continued on next page)

TABLE II (cont)

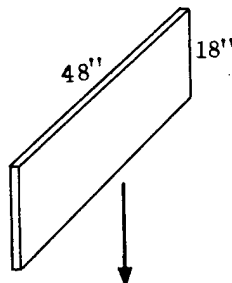
<u>Test No.</u>	<u>Initial Attitude</u>	<u>Altitude Above Terrain (ft)</u>	<u>Final Motion</u>
258-22	Edge on	2000	Autorotating



258-23	Rotation about yy axis	2000	Autorotating
--------	------------------------	------	--------------



258-24	Edge on	2000	Autorotating
--------	---------	------	--------------



258-25	Horizontal sliding-out motion (long edge)	10,000	Autorotating
--------	--	--------	--------------

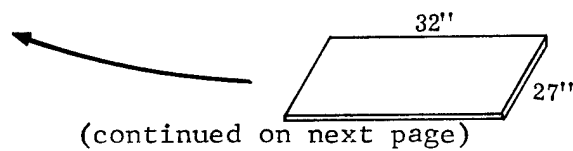
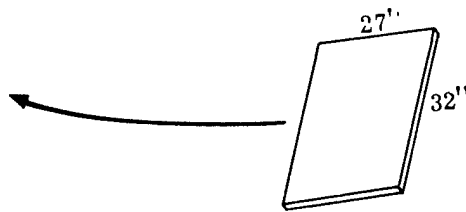


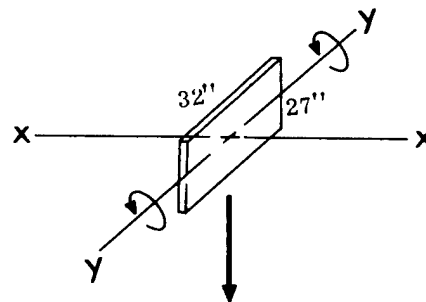


TABLE II (cont)

Test No.	Initial Attitude	Altitude Above Terrain (ft)	Final Motion
258-26	Horizontal sliding-out motion (short edge)	10,000	Autorotating



258-27	Rotation about yy axis	10,000	Autorotating
--------	------------------------	--------	--------------



for approximately 50 to 90 seconds before they went into an autorotational mode. The flat attitude (or  $\alpha = 90^\circ$ ) is a statically stable position for the plates. In each case in which a plate autorotated,\* the plates entered the autorotating mode by building up a rocking amplitude in a vertical plane. The plate's first full revolution of rotation was completed by rotating in a plane inclined  $45^\circ$  to  $60^\circ$  from the vertical. Simply, then, the plate did not have enough kinetic energy to rotate over "top dead center." However, rotation was achieved about an axis inclined to a position requiring less potential energy to support the rotation. After rotation was well established, the plate in some cases returned to vertical.

---

\*There were cases where the plates started autorotating almost immediately. This occurred mostly when an initial angular rate was imparted to the plate.

The motion of the plates was irregular. This is understandable since Plate No. 1 was nearly square and had a low aspect ratio. A more stable rotation can be achieved by increasing the aspect ratio, i.e., making a longer rectangle. This was the case for Plate No. 2, whose aspect ratio was 2.67 compared to Plate No. 1's aspect ratio of 1.12. For Plate No. 2, the rotational rate was higher and more nearly regular than it was for Plate No. 1. This regular and irregular motion is a function of the dynamic moment which, in turn, depends on the moment of inertia. This is illustrated by the dynamic-moment equation

$$I\ddot{\alpha} = M(\alpha) + M(A) \quad (1)$$

where:  $\alpha$  = Angle of attack

$M(\alpha)$  = Static aerodynamic moment, for  $\alpha$  constant

$M(A)$  = Net driving or damping moment resulting from a plate's rotation; will be referred to as auto-rotational moment.

$I$  = Moment of inertia about axis of rotation.

The above equation can be analyzed qualitatively considering Figure 4.

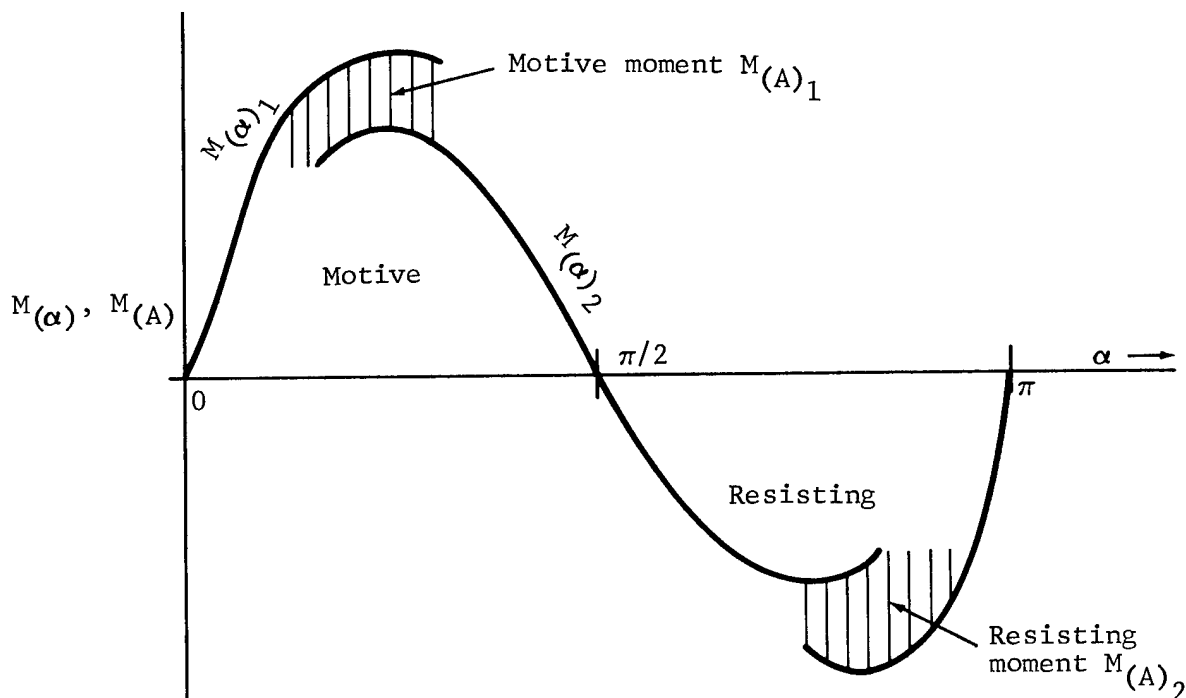


Figure 4. Variation of aerodynamic and autorotational moments with angle of attack

The above curve shows the variation of the moments  $M(\alpha)$  and  $M(A)$  with  $\alpha$ . If the integral  $\int_0^\pi M(\alpha) d\alpha$  has a positive value, it represents the motive energy of the moment  $M(\alpha)$  during the half revolution, which means that the net autorotational moment is driving, i.e.,  $M(A) = M(A)_1 - M(A)_2$  where now  $M(A)_1 > M(A)_2$ .<sup>\*</sup> For steady state motion

$$\int_0^\pi (M(\alpha) + M(A)) d\alpha = 0, \quad (2)$$

that is the motive energy  $M(A)_1$  is now balanced by the resisting energy  $M(A)_2$ . These moments are represented by the shaded areas in Figure 4. In the motive interval, the autorotational moment is causing autorotation, and for the rest of the period it is retarding autorotation. In the motive interval, a plate must store up enough kinetic energy to clear the second interval. Consequently, the motion cannot be sustained unless the moment of inertia of the plate is sufficiently high; otherwise, the rotation stops in a position where the plate starts to slide. In general, this explains why the plates with an aspect ratio near 1 have an irregular steady motion, while the plates with an aspect ratio of 2.67 have a more regular rotation; this results from the reduced chord. In general, it can be said that the basic free-flight motion of the plates was an autorotational mode, with the possibility of a broadside mode. The autorotational mode is much more predominant; the broadside mode is a special case. Analysis of the photographic data clearly indicates that the motion of the plates is independent of the initial conditions and that the final motion of a plate is either autorotational or a broadside attitude (see Table II).

The autorotational rate of the plates was read from the photographic film. It was difficult to obtain a single-degree-of-freedom rotational rate from the film because of the compound motion. This compound motion consists of the plate rotating about a tilt axis and, at the same time, precessing and translating (Figure 5). The plate is rotating about the yy axis which is perpendicular to the zz axis; the zz axis is tilted from a vertical axis. Also, there is a precessional

---

<sup>\*</sup>NOTE: This autorotational net moment can be either damping or driving, i.e.,  $M(A)_1 \gtrless M(A)_2$ .

motion superimposed; this motion has an angular rate,  $\Omega$ , around the vertical axis.

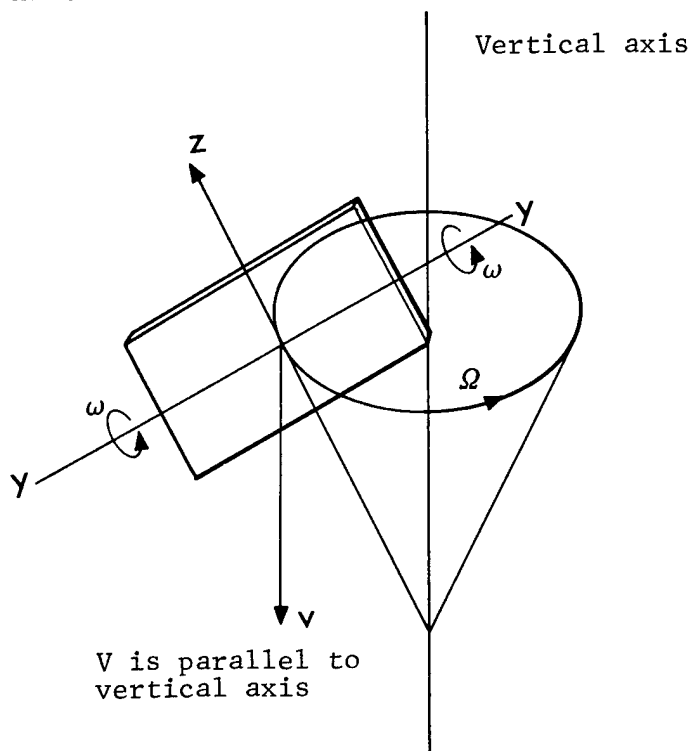


Figure 5. Diagram of plate's compound motion

Average angular rotational rates around the plate's axis of minimum inertia were obtained from the film data as a function of time for the plates; the rates are shown in Figure 6 for some of the tests. Since these rates are fairly well scattered, a least square computer technique was used to fit the angular rate data. Two methods of solution were used, "normal" least squares and orthogonal polynomials; the normal least square method gave the best fit. (See Appendix for technique). Using this technique, angular rate curves versus time were obtained for two of the tests and are shown in Figures 7 and 8 along with their representative equation. These curves exhibit the typical characteristics of an autorotating body with a peak buildup of angular rate and a decay to a steady-state value of approximately 5 rps. In general, the dynamic data obtained from these tests are fairly qualitative, so no specific results or analysis can be obtained. However, they do show that the plates have a compound autorotational motion and that the final motion of a plate is independent of its initial condition. These conclusions are based on analysis of the film data. In order to

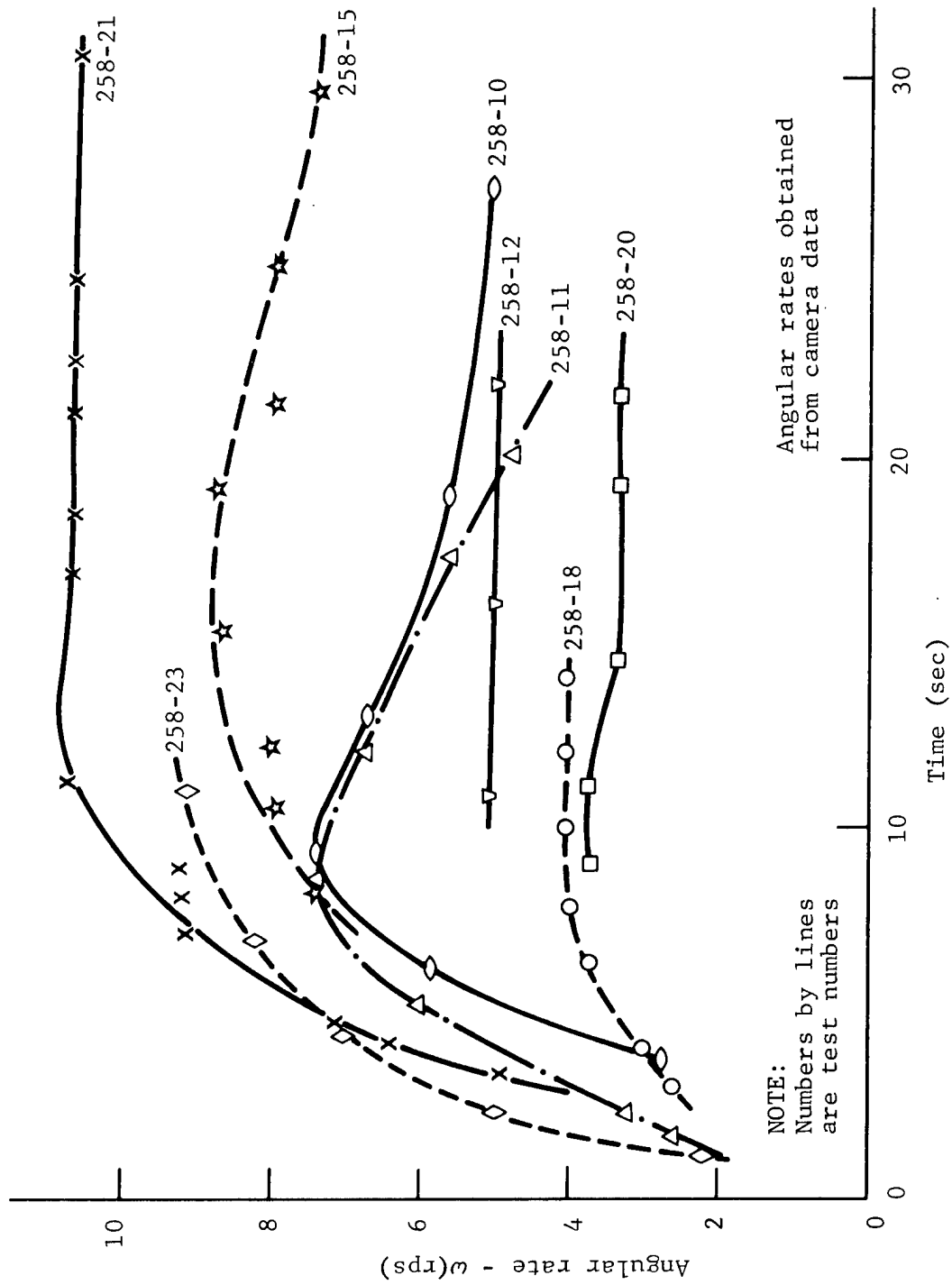


Figure 6. Plate's average angular rate obtained from camera data

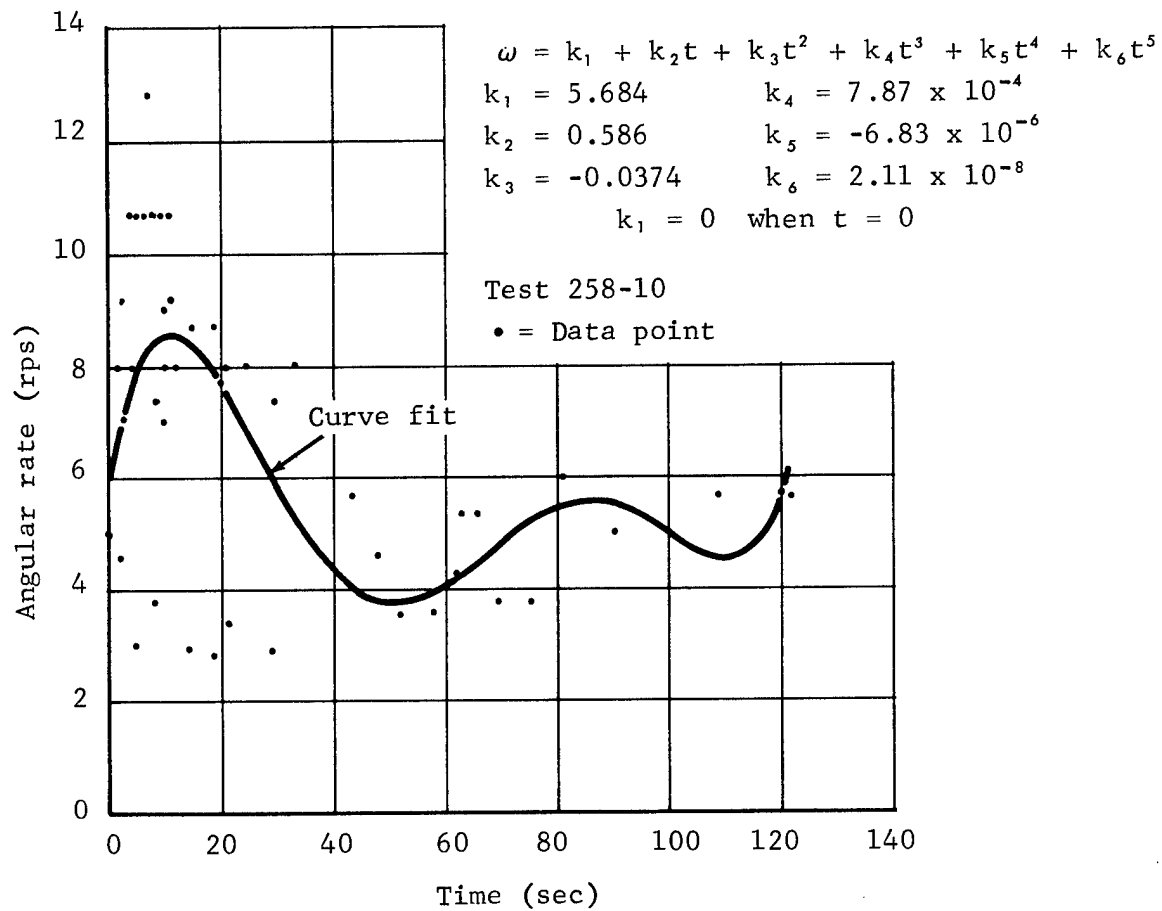


Figure 7. Curve fit of angular rate data for one drop test

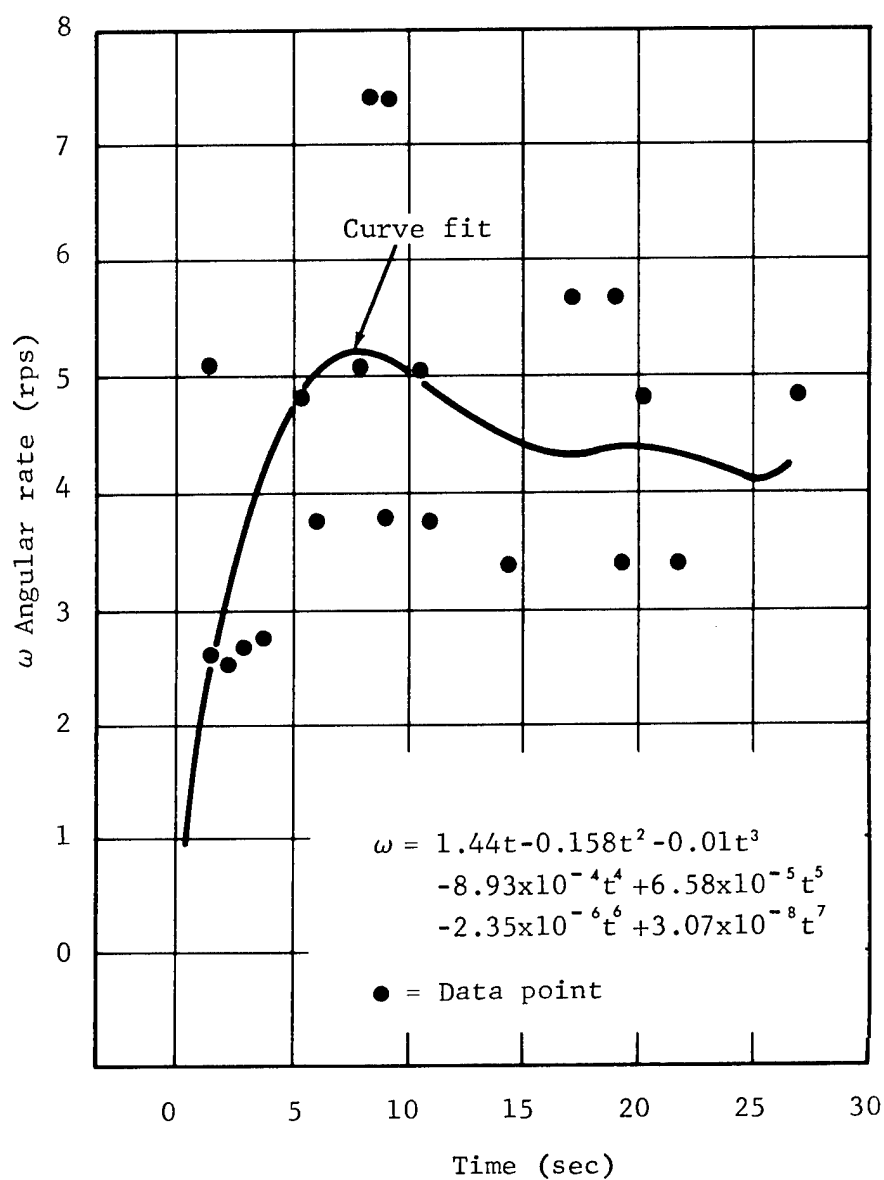


Figure 8. Curve fit of angular rate data for one drop test

do a complete, detailed analysis of this motion, the full 6-degree-of-freedom aerodynamic coefficients are required. This is planned for future studies where the dynamic aerodynamic coefficients will be obtained from wind-tunnel tests and then used to predict analytically the motion of the plate.

### Drag Coefficients

The drag coefficient ( $C_D$ ) of the plates was calculated as a function of time, velocity, and Mach number from the trajectory data\* obtained from the ground-based tracking cameras. The referenced area used for the coefficient was based on the 6 ft<sup>2</sup> broadside area of the plate. A typical drag coefficient versus time plot for three drop tests is shown in Figure 9. The plate in Test 258-13 remained in a flat, rocking attitude for 90 seconds before autorotating; in Tests 258-16 and 258-17, the plates remained in a flat, rocking attitude for roughly 50 seconds before autorotating. As indicated in Figure 9, the drag remains fairly constant with time until the plates go into an autorotating mode, at which time the curve shows oscillations in the data. These oscillations result from the variations in the trajectory caused by the gliding and spiraling effects of the plate. Also, some of these variations result from the manner in which the data are smoothed and reduced in order to obtain the drag coefficient.

The drag-coefficient data were used to obtain an equation for  $C_D$  as a function of velocity. The drag data for each test were curve-fitted, using a least-squares fit computer program technique. This method is presented in the Appendix. First and second order equations were obtained from this curve-fit program. In general, the first-order equation was satisfactory, and the equations were of the form

$$C_D = K_1 - K_2 V, \quad (3)$$

where

$V$  = velocity

$K_1, K_2$  are arbitrary constants.

A typical drag coefficient versus velocity curve and its fit are shown in Figure 10. For each test,  $K_1$  and  $K_2$  had different values; however, for the tests considered, the constants ranged in value as shown below:

$$1.50 < K_1 < 4.00$$

$$0.0050 < K_2 < 0.0300.$$

---

\*The complete trajectory data (i.e., range, altitude, velocity, acceleration, etc., versus time) were obtained for all tests except Tests 258-19 and 258-22. No data were obtained for these tests because the plates were mistracked.



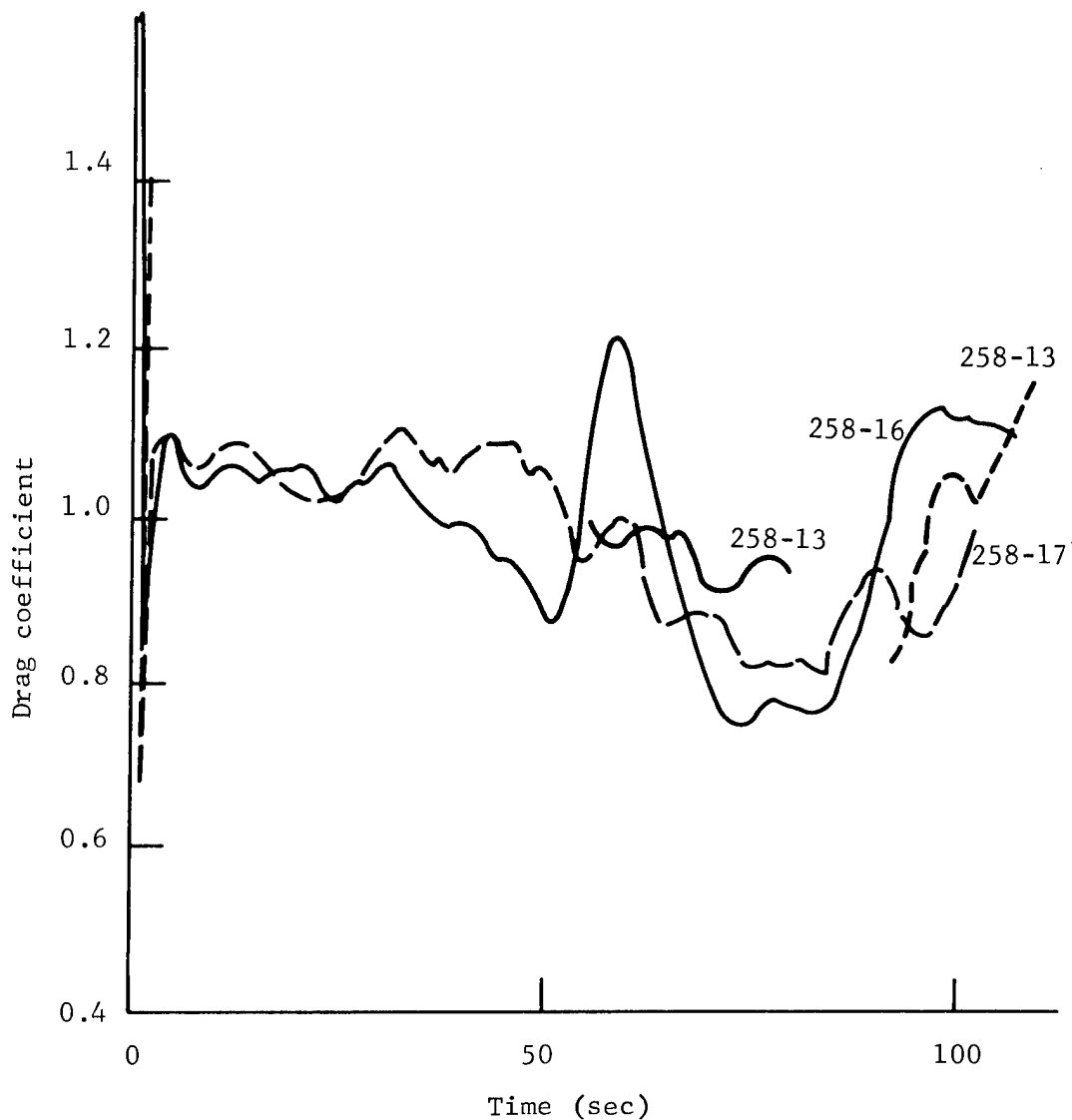


Figure 9. Variation of drag coefficient of plate during its flight

An attempt was made to determine if the constants in Equation (3) were dependent in any way on the initial attitude of the plates and if the constants could be correlated from test to test. No dependency or correlation was found. The drag coefficient was calculated for a velocity of 90 fps for each initial attitude. These average drag values are shown below as a function of initial attitude.

Initial Attitude	$C_D$
Flat	0.980
Rotating	0.940
Sliding out	1.025
Edge on	0.955

These drag coefficients compare quite well with the drag coefficient of a plate normal to the flow at subsonic speeds (see Reference 2).

Equation (3) and Figure 10 show the drag decreasing with increasing velocity. At first, this might appear aerodynamically perverse since, generally, drag increases with increasing velocity. However, for a rotating flat plate for a given velocity or Reynolds number, the drag will decrease with increasing velocity. It is important to point out that this is true only for a certain limited velocity range and that Equation (3) applies only for a certain velocity range. In this case the decrease of drag coefficient with velocity can be explained by analyzing the local flow over the rotating plate. This flow is analogous, in the limit (i.e., a large rotational rate,  $\omega$ , to the flow over a cylinder. Therefore, for certain  $\omega/V$  velocity ratios, the separation on the plate is delayed, and, consequentially, the wake (pressure) drag decreases.

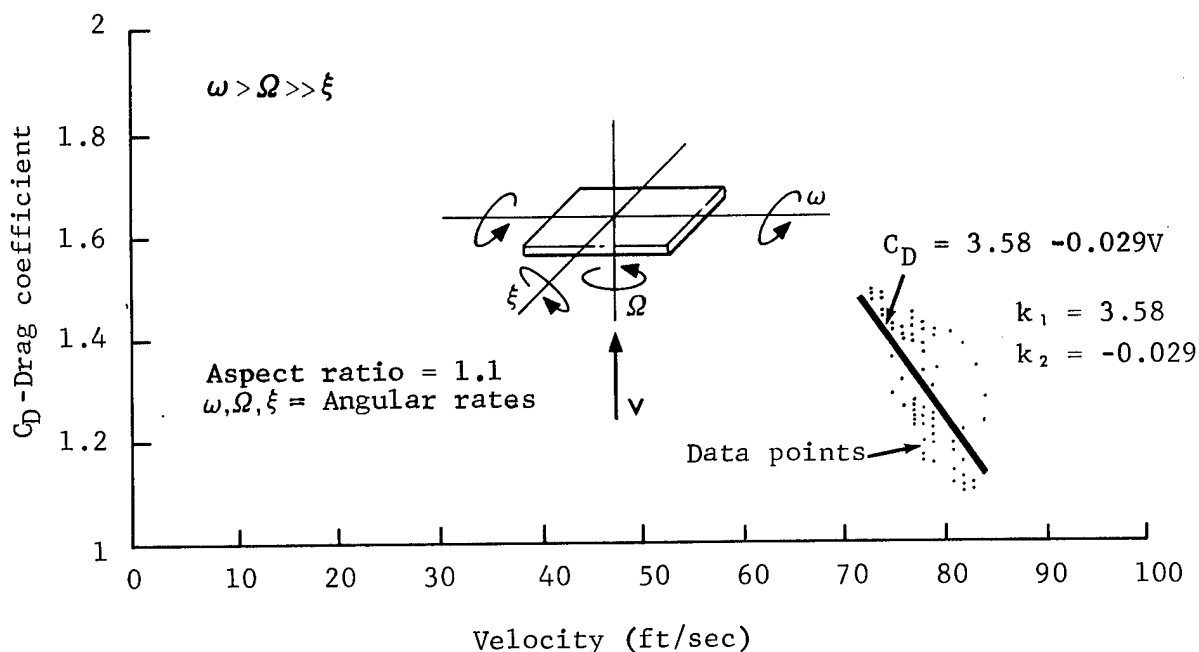


Figure 10. Variation of plate's drag coefficient with velocity

Equations of the form of Equation (3) were obtained and plotted for each drop test and are shown in the appendix.

### Velocity

Velocity data were obtained for each drop test except Tests 258-19 and 258-22. These data are derived from the trajectory data provided by the tracking cameras. Figures 11 and 12 show some typical variations

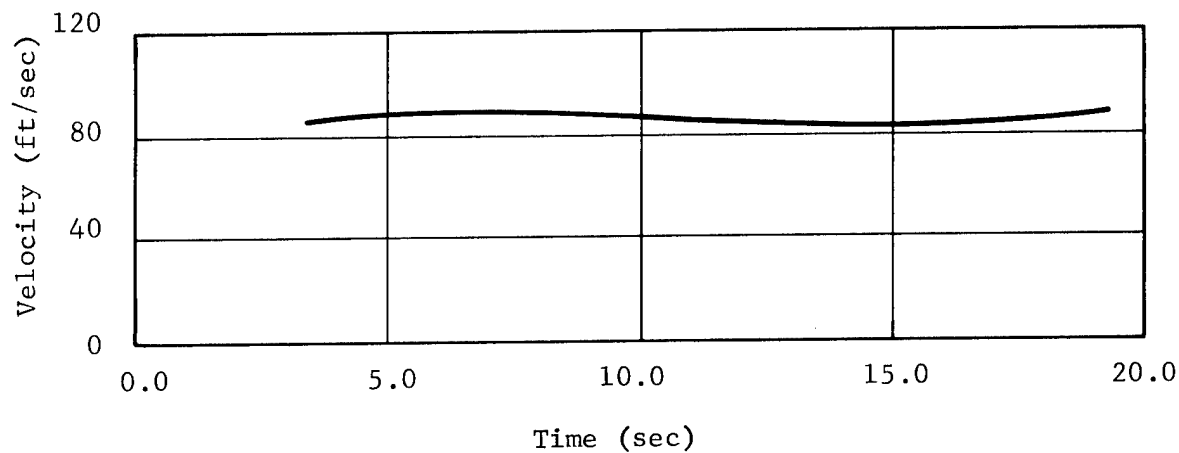


Figure 11. Typical variation of plate velocity with time

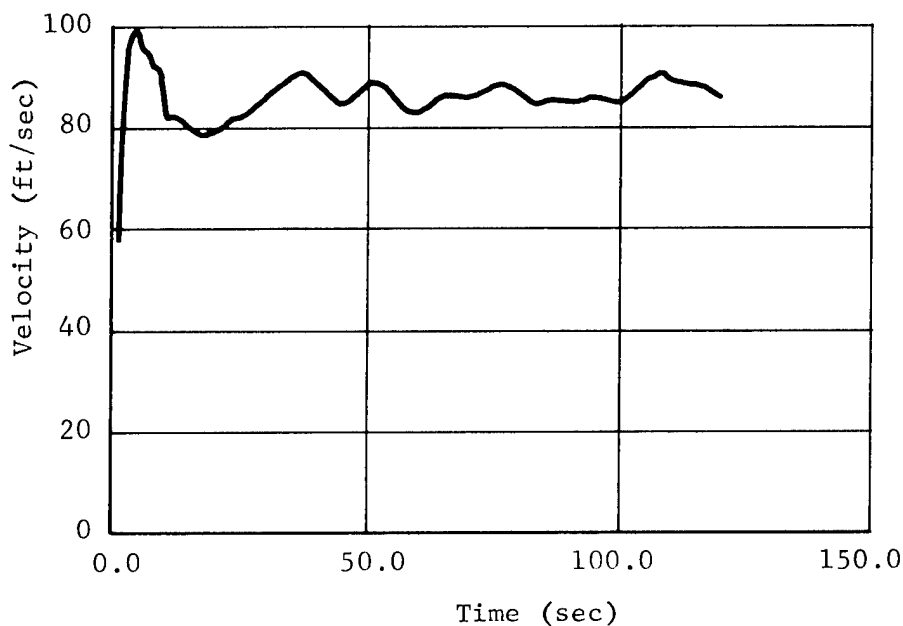


Figure 12. Typical variation of plate velocity with time

of velocity with time. In Figure 12, the oscillations in the velocity versus time curve result from the smoothing and data techniques used in obtaining the velocity.

Prior to the actual tests, the terminal velocity for the plate was calculated as a function of altitude, this was done for various plate attitudes (Figures 13 and 14). In addition, Figure 13 gives the velocity for the 10,000-foot drops, and Figure 14, gives the velocities for the 2000-foot drops. It is evident from Figures 13 and 14 that the velocities reached in the tests fall between the two curves which indicate plate rotation about its short and long axes ( $W/C_D A = 6.06$  and  $9.5$ ); this is where the data should fall since the actual rotational motion of the plates was composed of these two motions. However, there are two exceptions in Figure 14 (2000-foot drops); the velocities from Tests 18 and 23 do not fall between these two curves; this could be the result of an error in the trajectory data.

In general, the terminal velocities obtained from the tests agree quite well with the predicted velocities as shown in Figures 13 and 14.

#### Altitude/Range Data

One of the items of interest in the drop tests of the plates was the range/altitude data. These data are helpful in determining the dispersion of the plates. Since the plates are autorotating, circulation is induced which generates a lift force. This force tends to impart a gliding or spiraling trajectory to the plates. If a gliding trajectory is imparted to a plate, it will generally sail and have a greater range than if it were falling without a lifting influence. The altitude versus range data were plotted for all the tests,\* (Figures 15 and 16), and some of the spiraling trajectories are evident in these figures. It also can be seen that the maximum range for the 10,000-foot drops was 6000 feet, and for the 2000-foot drops, it was 1000 feet. Using the altitude/range data, it was determined that for the 10,000-foot drops the maximum  $L/D$  developed by the plate was 0.70 and the minimum was 0.333. For the 2000-foot drops, the maximum  $L/D$  of the plate was 0.400 and the minimum was 0.100. Essentially, these  $L/D$  ratios show that some appreciable lift was generated by the rotating

---

\*Except Nos. 19 and 22; no data were obtained for these drops.

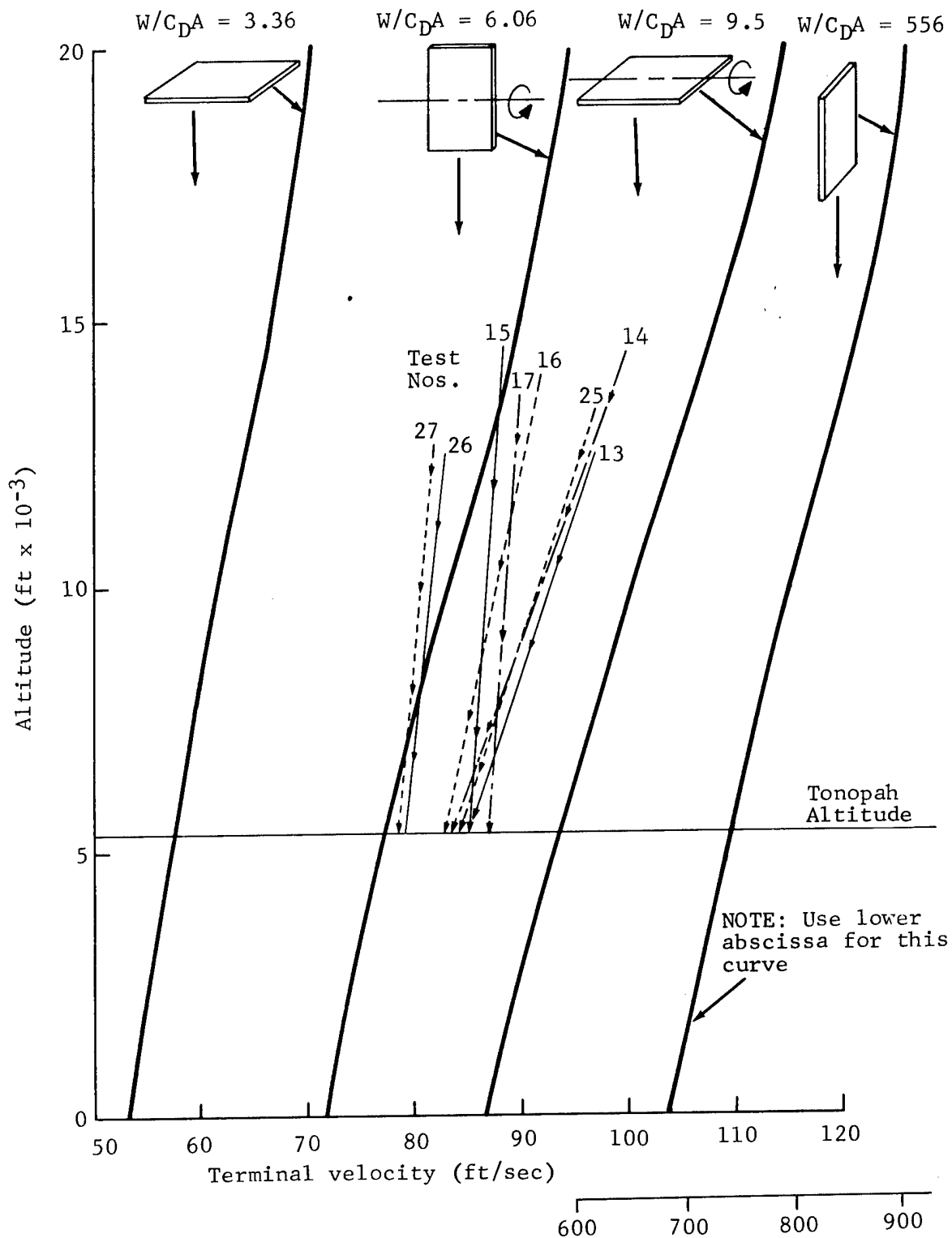


Figure 13. Terminal velocity for plates dropped from 10,000 feet above terrain

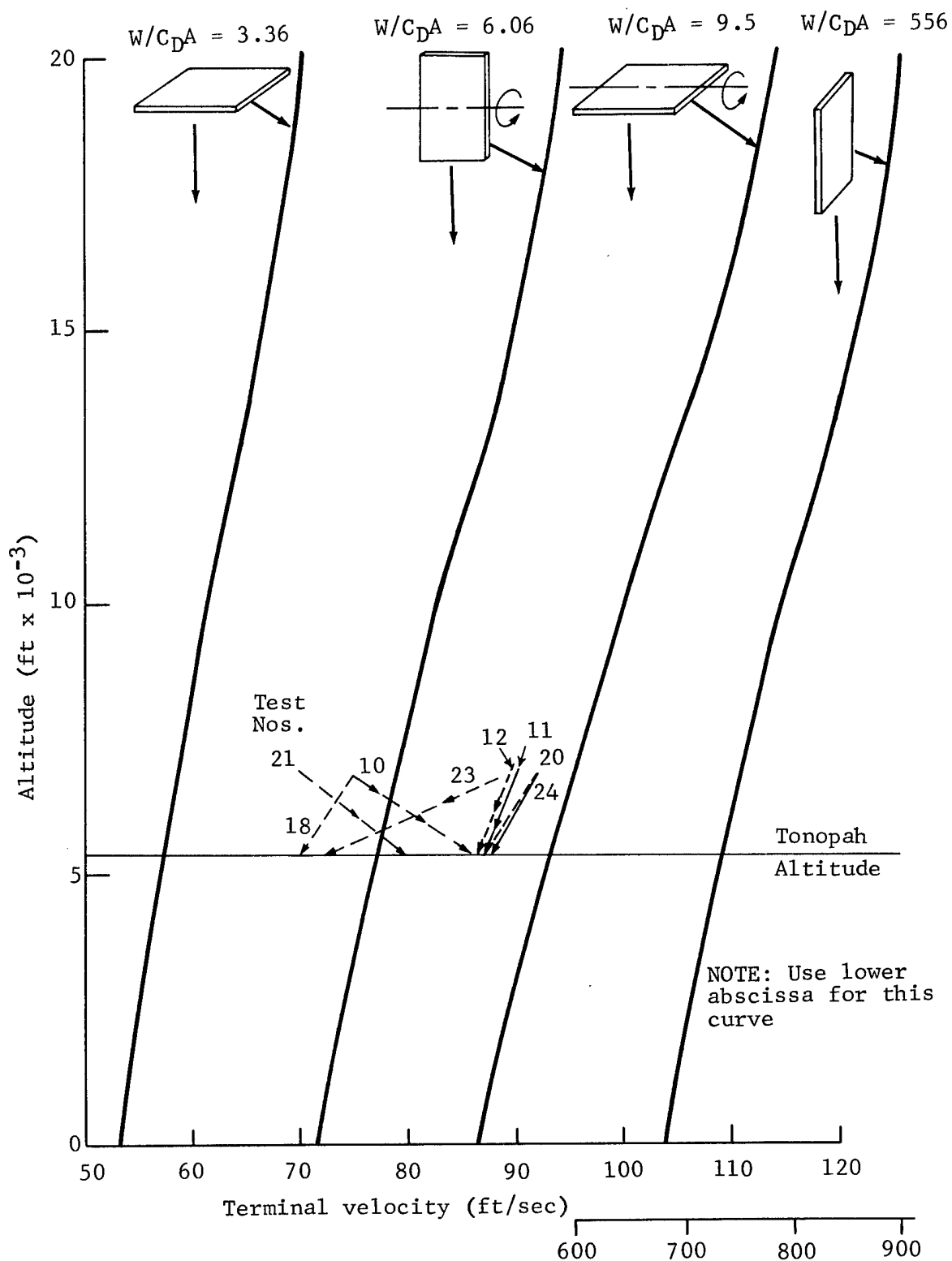


Figure 14. Terminal velocity for plates dropped from 2000 feet above terrain

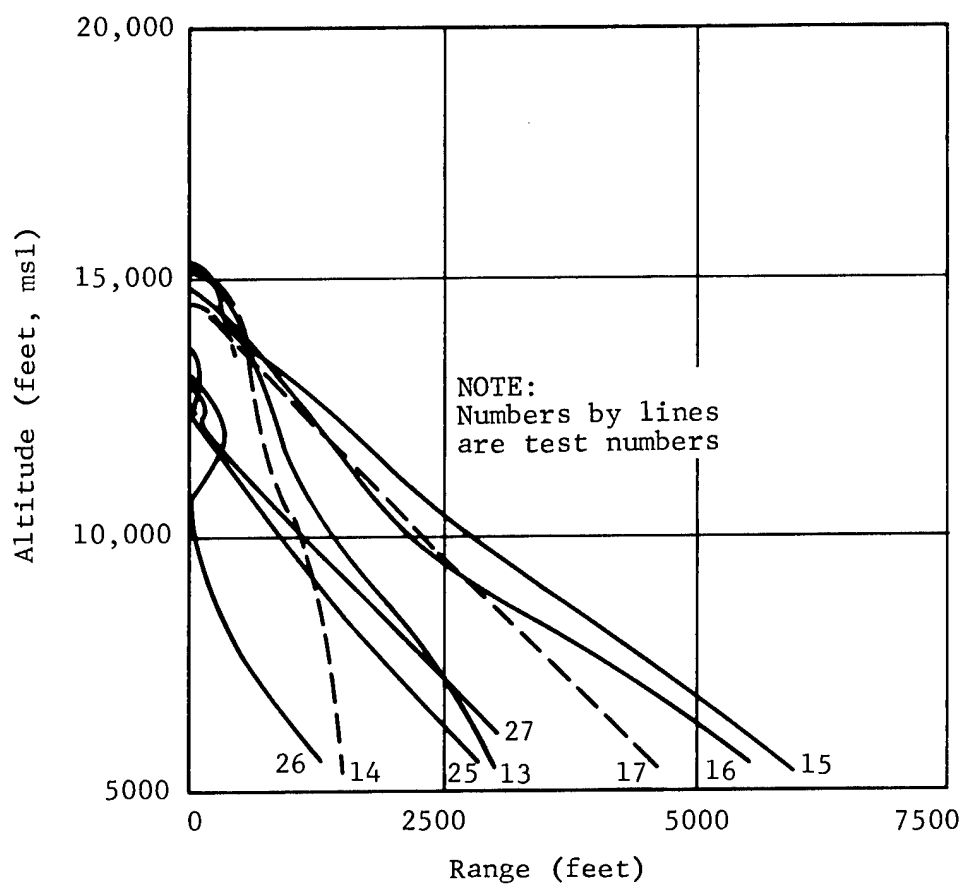


Figure 15. Variation of altitude with range for drops from 10,000 feet above terrain

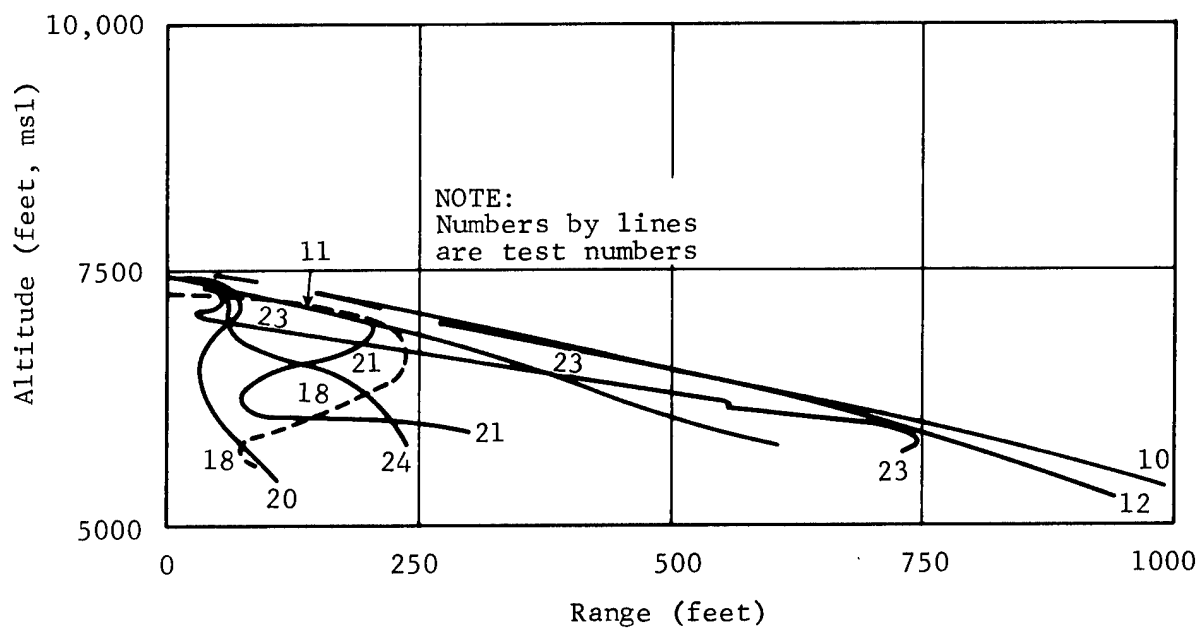


Figure 16. Variation of altitude with range for drops from 2,000 feet above terrain

flat plates; since the autorotational motion was irregular, these L/D ratios were fairly low.

An attempt was made to see if there was a correlation of range (maximum or minimum) with initial attitude; as was expected, none was obtained. The impact range for the various initial attitudes is shown in Figure 17.

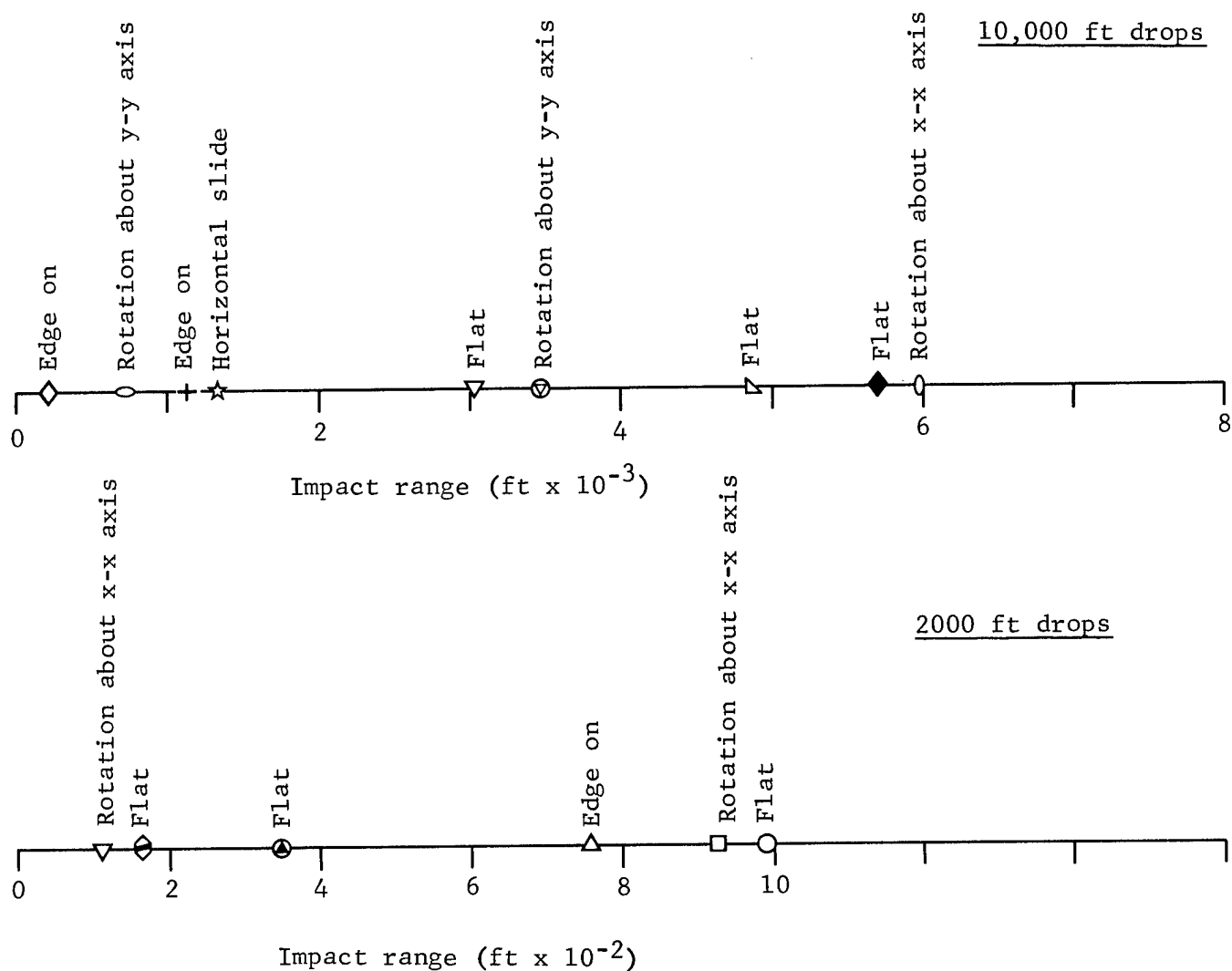


Figure 17. Impact range for various initial attitudes of plates



### Critical Reynolds Number

It is worthwhile to discuss the critical Reynolds number,\* and to determine if the plates in these tests were in turbulent or laminar flow (below or above critical Reynolds number). It is generally assumed that, for steady-state flow on a flat plate at  $\alpha = 0^\circ$  with carefully controlled conditions and a very smooth surface, the critical Reynolds number is generally  $5 \times 10^5$ . For the same plate at  $\alpha = 90^\circ$ , the flow is generally considered to be turbulent and the critical Reynolds number is not considered. The cases of  $\alpha = 0^\circ$  and  $90^\circ$  are the two extremes for a tumbling body, and the flow on a tumbling body is not in steady state. In addition to the stream turbulence, the transition Reynolds number depends on the manner in which the pressure in the flow and the velocity vary along the surface. When the pressure gradient is favorable (positive), the critical Reynolds number increases. A flow deceleration along the surface decreases the Reynolds number for transition. In the case of the tumbling or autorotating flat plate, the flow on either side of the plate reverses direction twice per revolution; hence, the critical Reynolds number should be lower than  $5 \times 10^5$  for the dynamic case. It is assumed, therefore, that the flow on the tumbling flat plate is predominantly turbulent, and therefore the drag coefficient is for turbulent flow. Even under steady-flight conditions and at ambient temperature the plate would be in turbulent flow (See Figure 18). Based on the plate's dimension of 27 inches, the Reynolds number would be greater than 500,000.

### Impact Characteristics

An item of interest and concern in these tests was the condition of Plate No. 1 at impact. Other items of interest were the attitude and velocity of the plates at impact. The impact velocities were obtained from the trajectory data and are shown in Figure 19. The velocities range from a minimum of 73 ft/sec to a maximum of 88 ft/sec. The average impact velocity was 83 fps. As can be seen in Figure 19, the impact velocity was fairly independent of the release altitude. The kinetic energy of the plate at impact, based on an impact velocity of 88 fps, was 4810 ft-lbs. The TNT equivalent of this kinetic energy is 0.05 ounces. Obviously, the plate's energy at impact is quite

---

\*Critical Reynolds number is defined as termination of laminar separation.

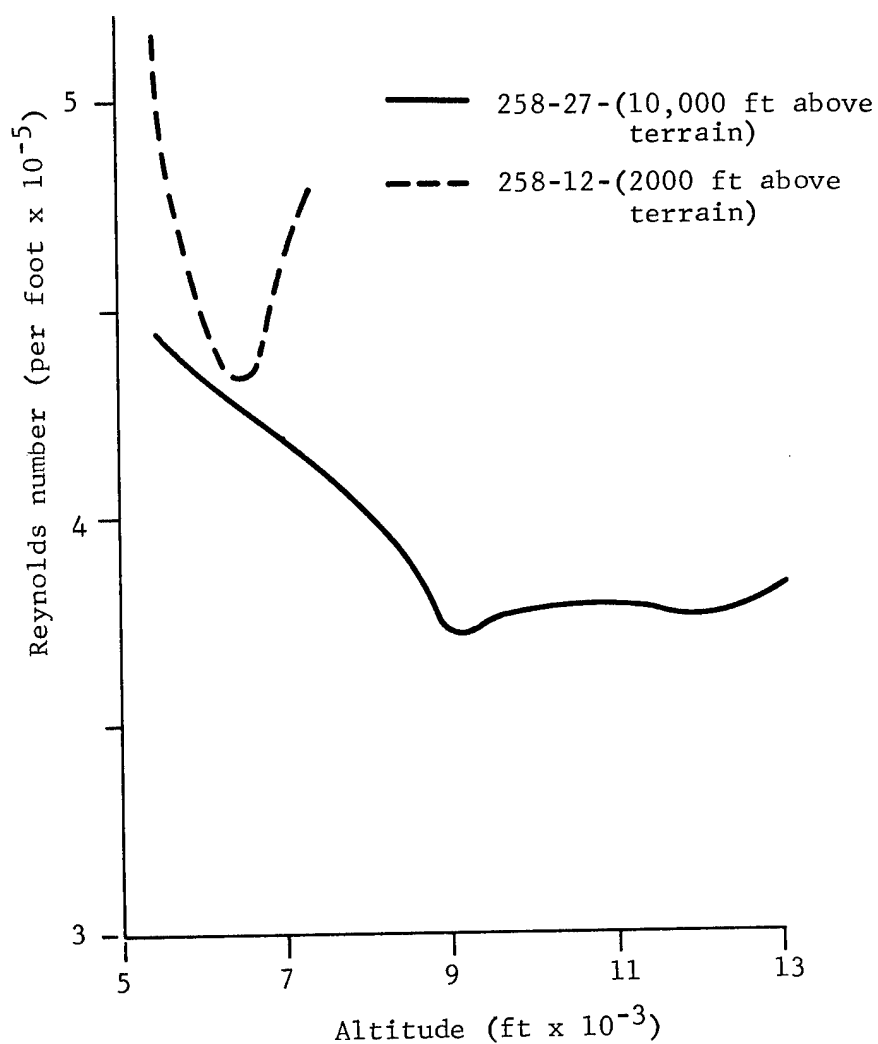


Figure 18. Reynolds number variation with altitude for two drop tests

Test No.

- ⊙ 258-10
- △ 258-11
- 258-12
- ▽ 258-13
- ◇ 258-14
- ⊖ 258-15
- ☆ 258-16
- ⊕ 258-17
- 258-18
- 258-20
- ▼ 258-21
- ◆ 258-23
- ★ 258-24
- ⦿ 258-25
- 258-26
- ⊗ 258-27

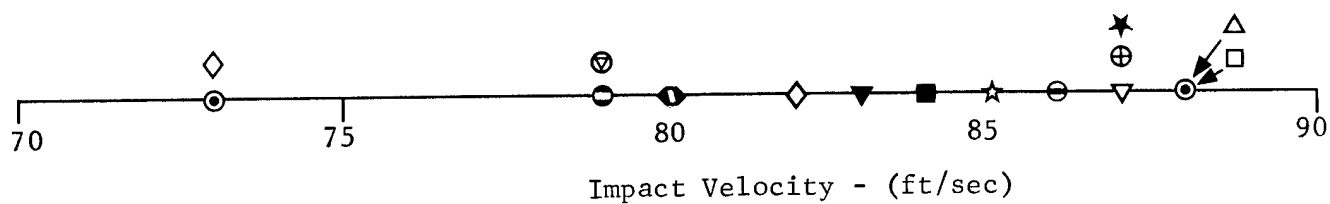


Figure 19. Plate impact velocity for the various drops

small, and damage to a structurally designed plate should be either small or nonexistent.

Figure 20 shows two plates as they appeared after impact. Table III gives the damage to and attitude of each plate at impact. Most of the plates impacted on the long side; this indicates that the free-flight motion of the plate was predominantly rotation about the minimum axis of rotation which in this case is the xx axis (Table III). The indentations made by the plates were generally from 3- to 5-inches deep and approximately 4-inches wide. The plates in general did not sustain severe or extensive damage; in fact, for Tests 258-16 and -17, the plates used were the same ones originally tested in Tests 258-13 and -14. In general, it is felt that the impact loading on the plates was not severe, and that a properly designed structural plate would encounter little, if any, damage.

#### Summary and Conclusions

The results of these tests show that the free-flight motion of these rectangular plates displayed compounded autorotational characteristics. This motion was the same (in general) for each drop, and was independent of the initial conditions. The predominant rotation of the plate was about its minimum axis of inertia; this motion was further compounded by the rotation about another vertical axis, thus introducing gyroscopic effects. The motion data was obtained primarily from photographic data. Angular rates were obtained from the photographic data and fitted with a least square curve which gave the angular rate as a function of time. This curve exhibited the typical autorotational rate characteristics, with a peak build-up in angular rate followed by decay to a steady-state value. For the curves obtained, this steady-state rate was 5 rps.

Trajectory data were obtained for all tests except two. By using these data, drag coefficients for the plates were obtained. Also determined were expressions which related the drag coefficient as a function of velocity. These expressions showed a decrease of drag coefficient with velocity. This was attributed to the reduction of turbulence, i.e., the reduction of separation on the plate, which in turn reduced the pressure drag. These expressions were obtained for each drop test.



Figure 20. Plates after impact

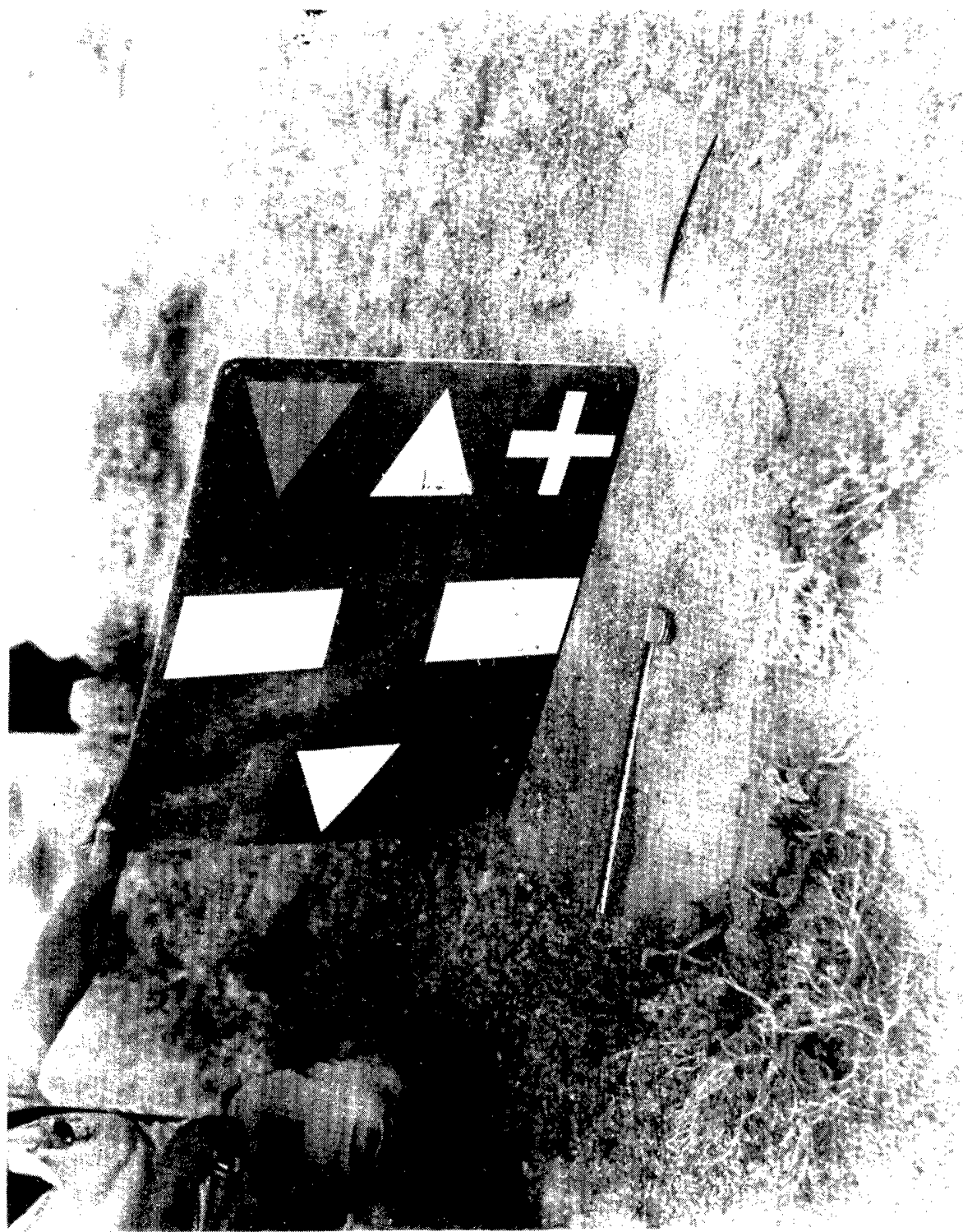
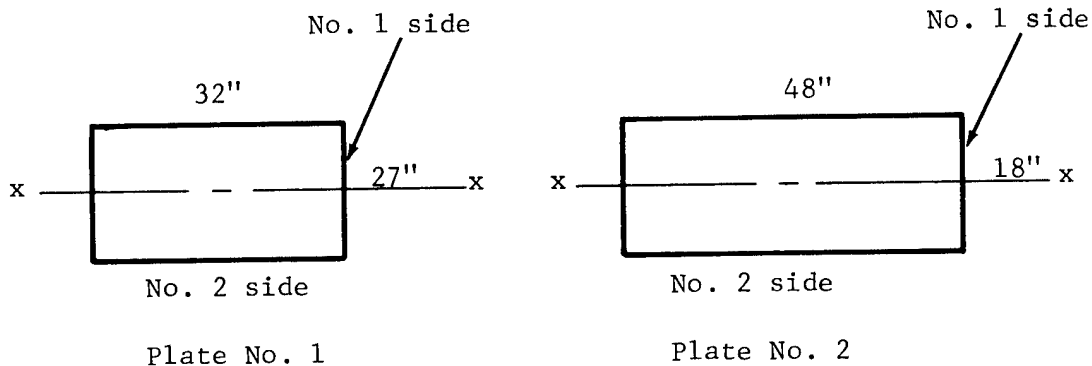


Figure 20. Plates after impact  
(cont)

TABLE III  
Impact Characteristics

<u>Test No.</u>	<u>Configuration</u>	<u>Attitude at Impact</u>	<u>Condition of Plate Following Impact</u>
258-10	Plate No. 1	Landed on No. 1 side	Slightly damaged
258-11	Plate No. 1	Landed on corner	Plate split
258-12	Plate No. 1	Landed on No. 2 side	Minor damage
258-13	Plate No. 1	Landed on No. 1 side	Good
258-14	Plate No. 1	Landed on No. 2 side	Good
258-15	Plate No. 1	Landed on No. 2 side	Fair
258-16	Plate No. 1	Landed on No. 2 side	Fair
258-17	Plate No. 1	Landed on No. 2 side	Destroyed
258-18	Plate No. 1	Landed on No. 2 side	Good
258-19	Plate No. 1	Landed on corner	Badly bowed
258-20	Plate No. 1	Landed on corner	Badly bowed and splintered
258-21	Plate No. 2	Landed on No. 2 side	Not applicable
258-22	Plate No. 2	Landed on corner and No. 1 side	Not applicable
258-23	Plate No. 2	Landed on No. 2 side	Not applicable
258-24	Plate No. 2	Landed on No. 1 side	Not applicable
258-25	Plate No. 1	Landed on corner and No. 1 side	Badly damaged
258-26	Plate No. 1	Landed on No. 2 side	Badly damaged
258-27	Plate No. 1	Landed on No. 2 side	Good



The velocity for each drop test was also obtained. The velocity as a function of altitude obtained from the tests was compared against that predicted, and the agreement was good. This comparison further showed that the plates exhibited autorotational motion.

Range and altitude data obtained from these tests provided information on dispersion characteristics of the plates. The maximum dispersion of the plates which were dropped from 2000 feet above terrain was within a circle 1000 feet in radius; the plates dropped from 10,000 feet above terrain were dispersed within a circle 6000 feet in radius. These data also showed that the autorotational motion of the plate generated some appreciable lift forces.

Based on the Reynold's number criterion, it was determined that the plates were in turbulent flow throughout the flight.

The impact data on the plates showed that the model plates generally suffered little at impact. Impact velocities for the plates were obtained, and it was determined that the plates impacted predominantly on the long side.

#### REFERENCES

1. Smith, A. M. O., "On the Motion of a Tumbling Body," Journal of Aeronautical Sciences, Vol. 20, February 1953.
2. Horner, S. F., Fluid Dynamic Drag, (published by the author), 1958.

## APPENDIX

Methods Used in Obtaining Equations of Angular Rate  
Versus Time and of Drag Coefficient as a  
Function of Velocity



## Appendix

### Methods Used in Obtaining Equations of Angular Rate Versus Time and of Drag Coefficient as a Function of Velocity

This appendix presents the method used to obtain equations of angular rate versus time and of drag coefficient as a function of velocity. The first order equations of drag coefficient versus velocity obtained for each test are presented in Table A-I, and plots are shown in Figures A-1 through A-32. Shown in these plots are the linear-fit line of the data and the error that exists between the computed value and the actual data value. As is evident, the error is generally small.

The following is a description of the method used. This method was formulated by the Mathematical Computing Services Division of Sandia Laboratories, Albuquerque.

#### Curve-Fit Technique

A least-squares technique is used to fit the points in the data set. This minimizes the sum of the squares of the differences between the polynomial and the data-set values. Two solution methods are used, "normal" least squares and orthogonal polynomials. Using "normal" least squares assumes a solution of the form

$$Y = A_0 + A_1X + A_2X^2 + \dots + A_nX^n . \quad (A-1)$$

The least-squares procedure leads to a system of  $n + 1$  equations which are solved for the values of  $A$  by the use of a double precision matrix inversion routine. This method begins to lose its stability above degree 11, and an alternate solution technique must be used.

Orthogonal polynomials assumes a solution of the form

$$Y = a_0 + a_1Q_1 + a_2Q_2 + \dots + a_nQ_n , \quad (A-2)$$

TABLE A-I

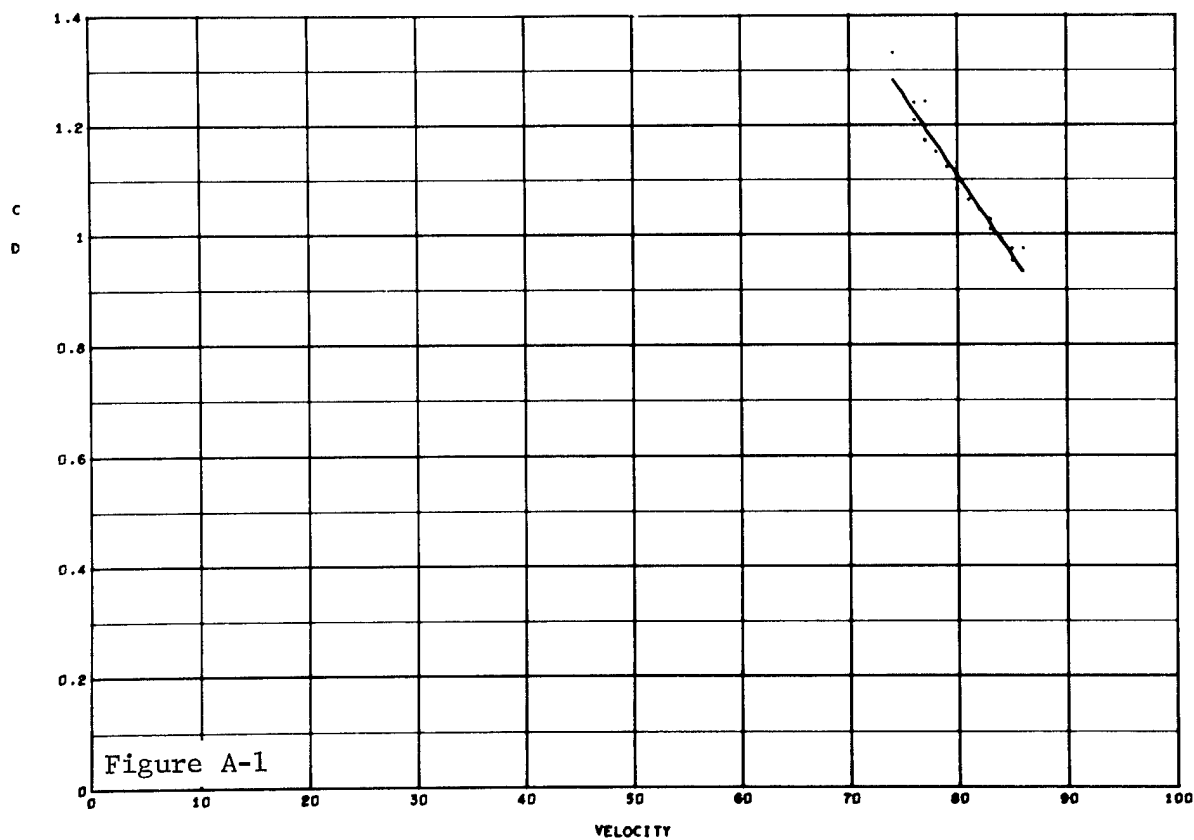
First and Second Order Equations of Drag Coefficient  
( $C_D$ ) Versus Velocity

Test No.*	First-Order Equation	Second-Order Equation
258-10	$C_D = 3.469 - 0.0295V$	$C_D = 12.58 - 0.257V + 0.0014V^2$
258-11	$C_D = 1.837 - 0.00978V$	$C_D = 6.76 - 0.124V + 0.00067V^2$
258-12	$C_D = 3.115 - 0.0248V$	$C_D = 7.83 - 0.134V + 0.00063V^2$
258-13	$C_D = 2.382 - 0.0156V$	$C_D = -2.95 - 0.106V + 0.000695V^2$
258-14	$C_D = 1.917 - 0.0104V$	$C_D = 3.03 - 0.035V + 0.000135V^2$
258-15	$C_D = 3.267 - 0.025V$	$C_D = 19.17 - 0.39V + 0.00209V^2$
258-16	$C_D = 1.613 - 0.0070V$	$C_D = -0.0263 + 0.039V - 0.00031V^2$
258-17	$C_D = 1.503 - 0.00585V$	$C_D = -0.0599 + 0.039V - 0.00031V^2$
258-18	$C_D = 2.421 - 0.0132V$	$C_D = -3.23 + 0.016V - 0.00136V^2$
258-20	$C_D = 2.982 - 0.0227V$	$C_D = 3.673 - 0.042V + 0.000135V^2$
258-21	$C_D = 4.6159 - 0.04104V$	$C_D = 1.799 + 0.0442V - 0.000629V^2$
258-23	$C_D = 3.020 - 0.0214V$	$C_D = 2.309 - 0.00037V - 0.000150V^2$
258-24	$C_D = 2.352 - 0.01586V$	$C_D = 1.404 + 0.00952V - 0.000164V^2$
258-25	$C_D = 2.674 - 0.01844V$	$C_D = 7.089 - 0.1179V + 0.0005565V^2$
258-26	$C_D = 2.811 - 0.01968V$	$C_D = -6.240 + 0.2031V - 0.00137V^2$
258-27	$C_D = 3.584 - 0.0292V$	$C_D = -0.1097 - 0.2184V - 0.00121V^2$

\*No velocity data obtained for Tests 258-19 and 258-22.

Figures A-1 through A-32  
Curve fits of drag coefficient  
versus velocity and  
error versus velocity

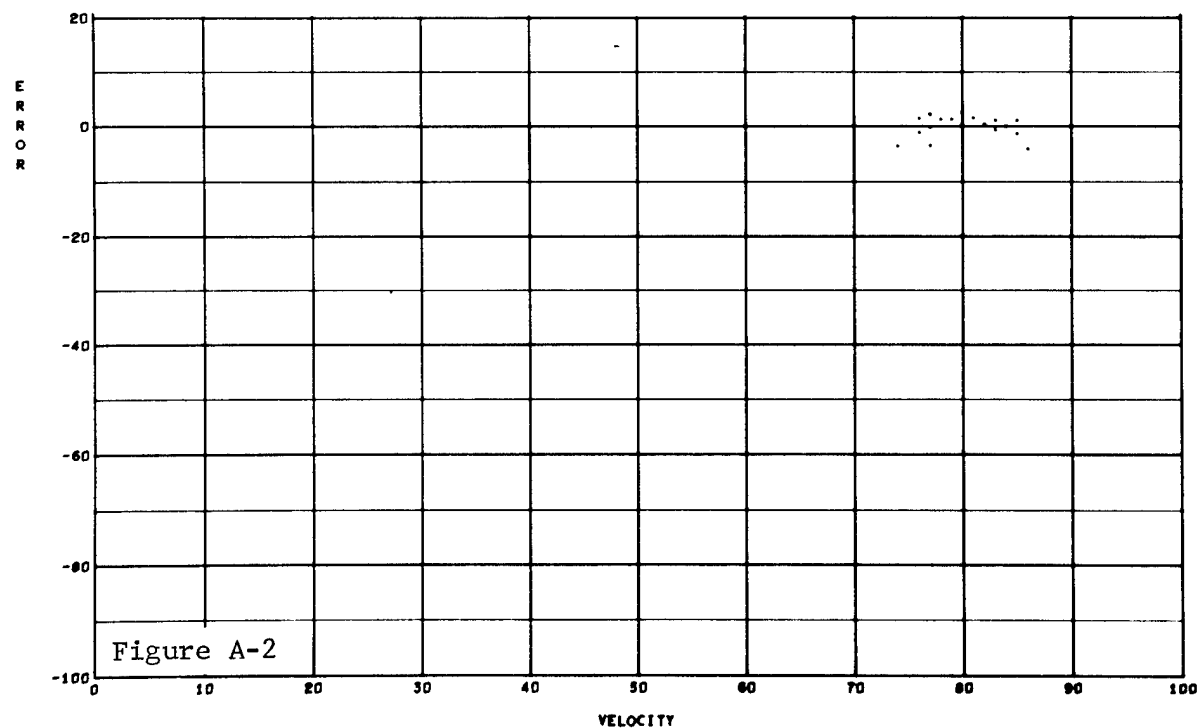
NOTE: Velocity is in feet per second.  
Error is in percent.



VELOCITY VS. C/D

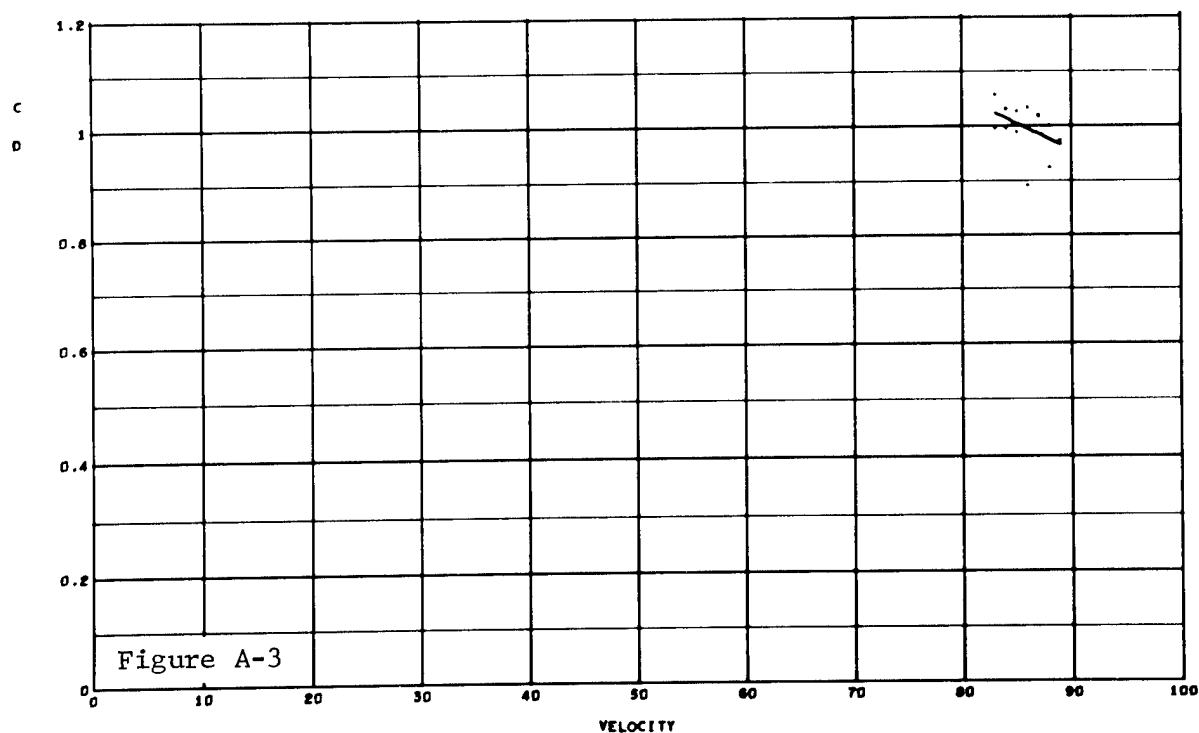
PASS 1 ZONE 1 TEST 258 10

DEGREE 1 LEAST SQUARES



VELOCITY VS. ERROR

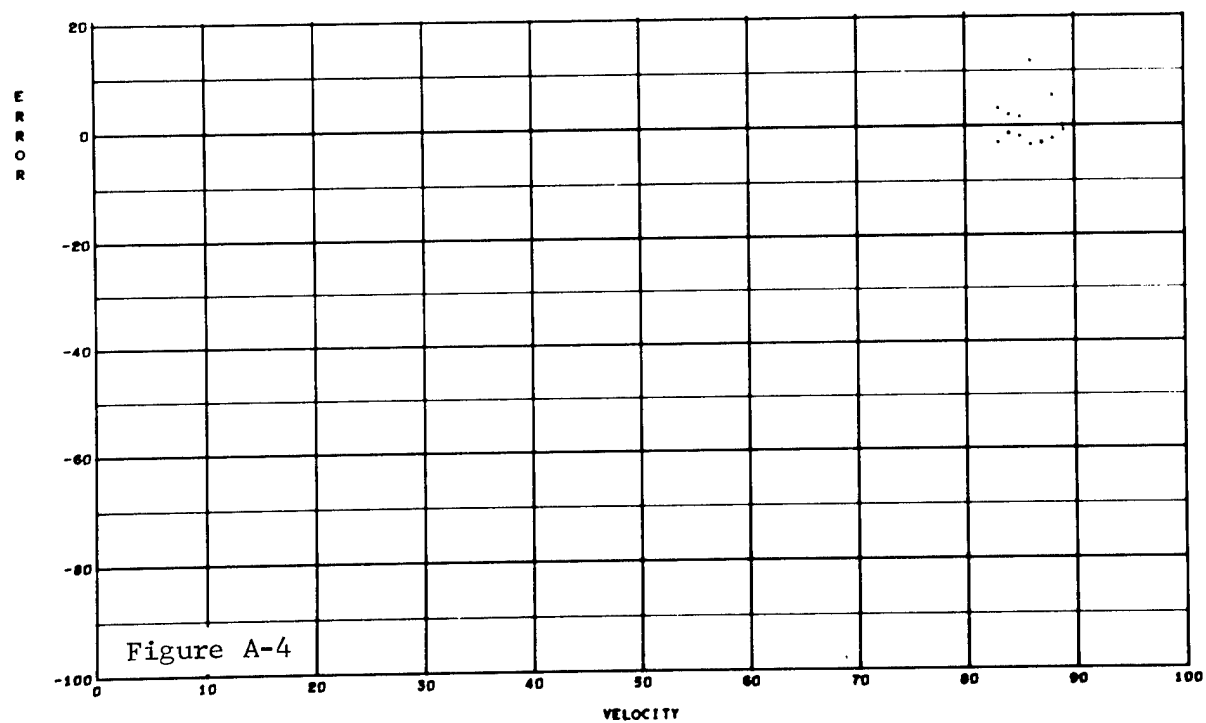
PASS 1 ZONE 1 TEST 258 10



VELOCITY VS. C D

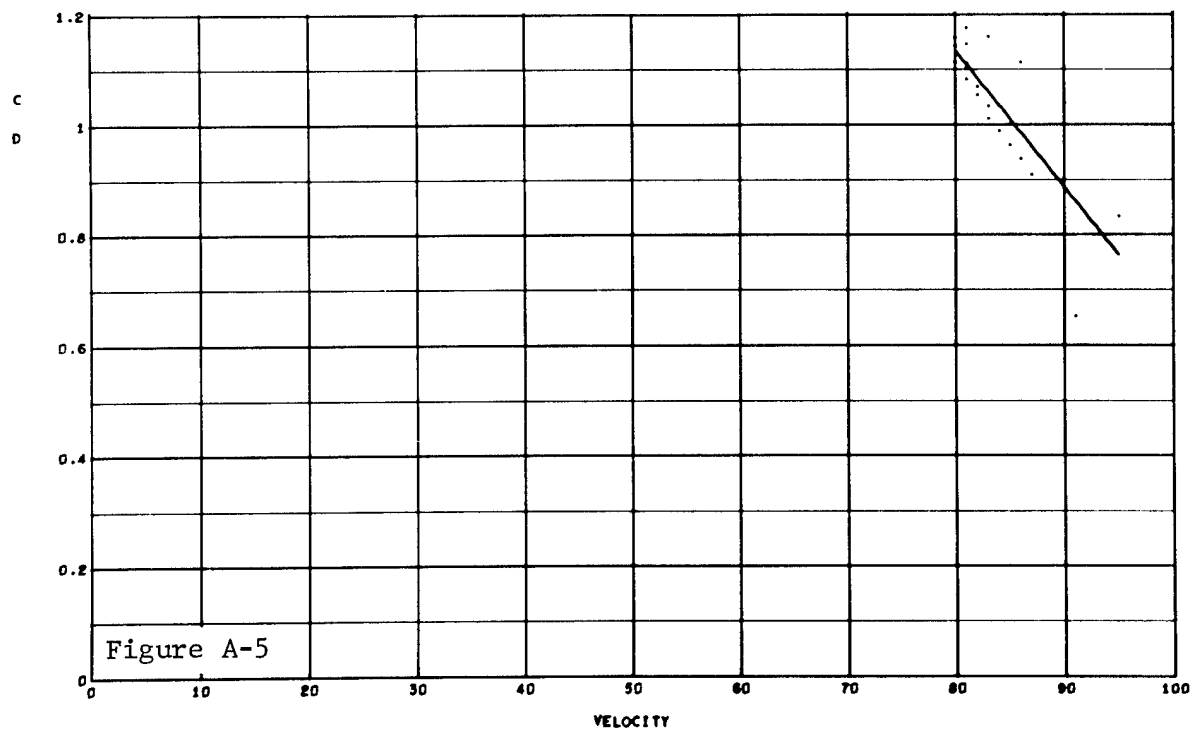
PASS 1 ZONE 1 TEST 258 11

DEGREE 1 LEAST SQUARES



VELOCITY VS. ERROR

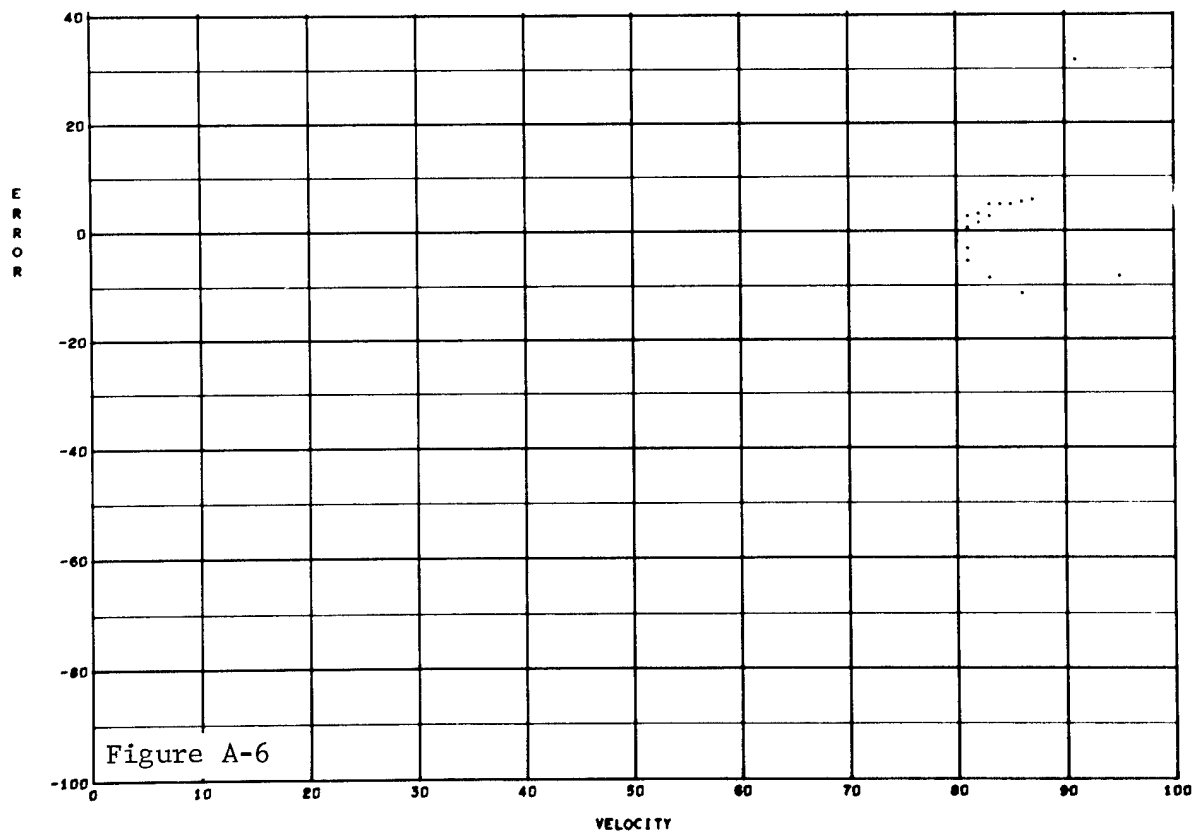
PASS 1 ZONE 1 TEST 258 11



VELOCITY VS. C D

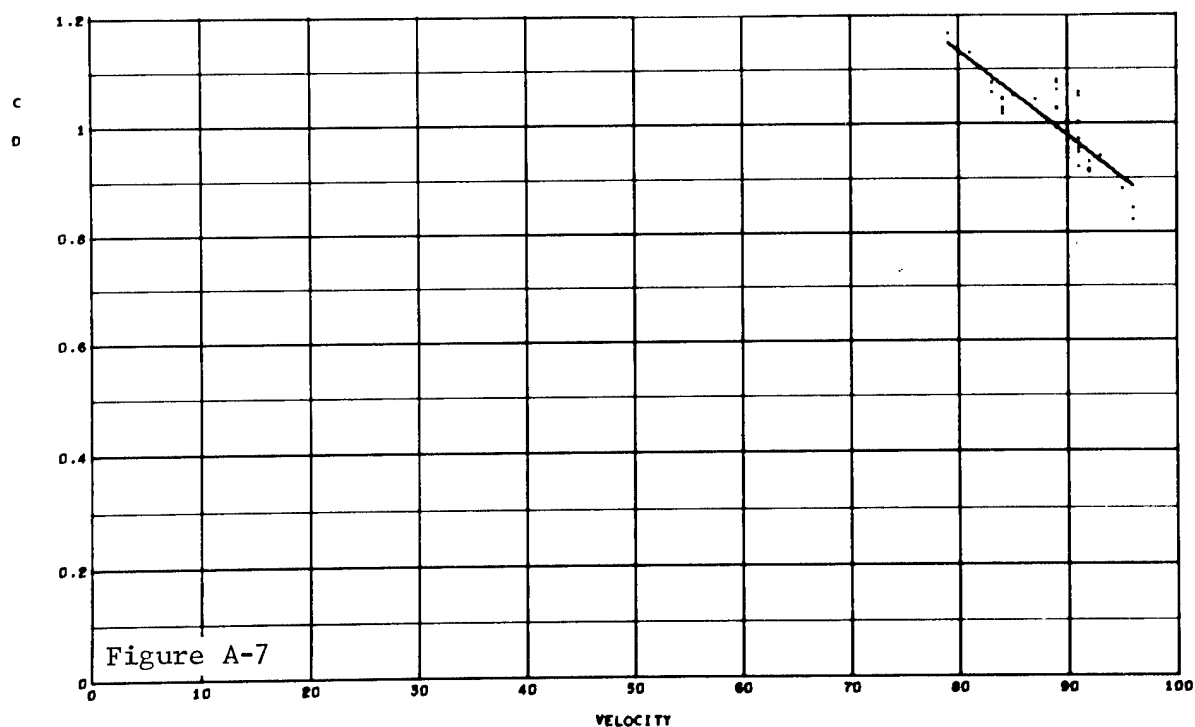
PASS 1 ZONE 1 TEST 250 12

DEGREE 1 LEAST SQUARES



VELOCITY VS. ERROR

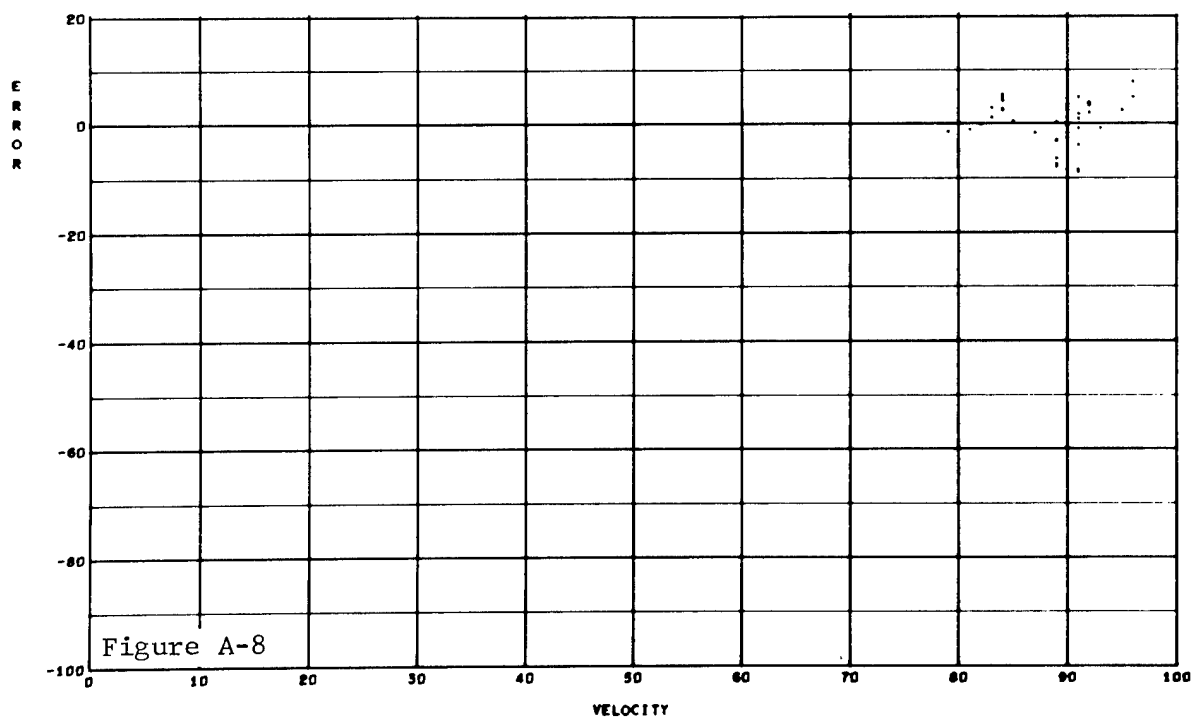
PASS 1 ZONE 1 TEST 250 12



VELOCITY VS. C D

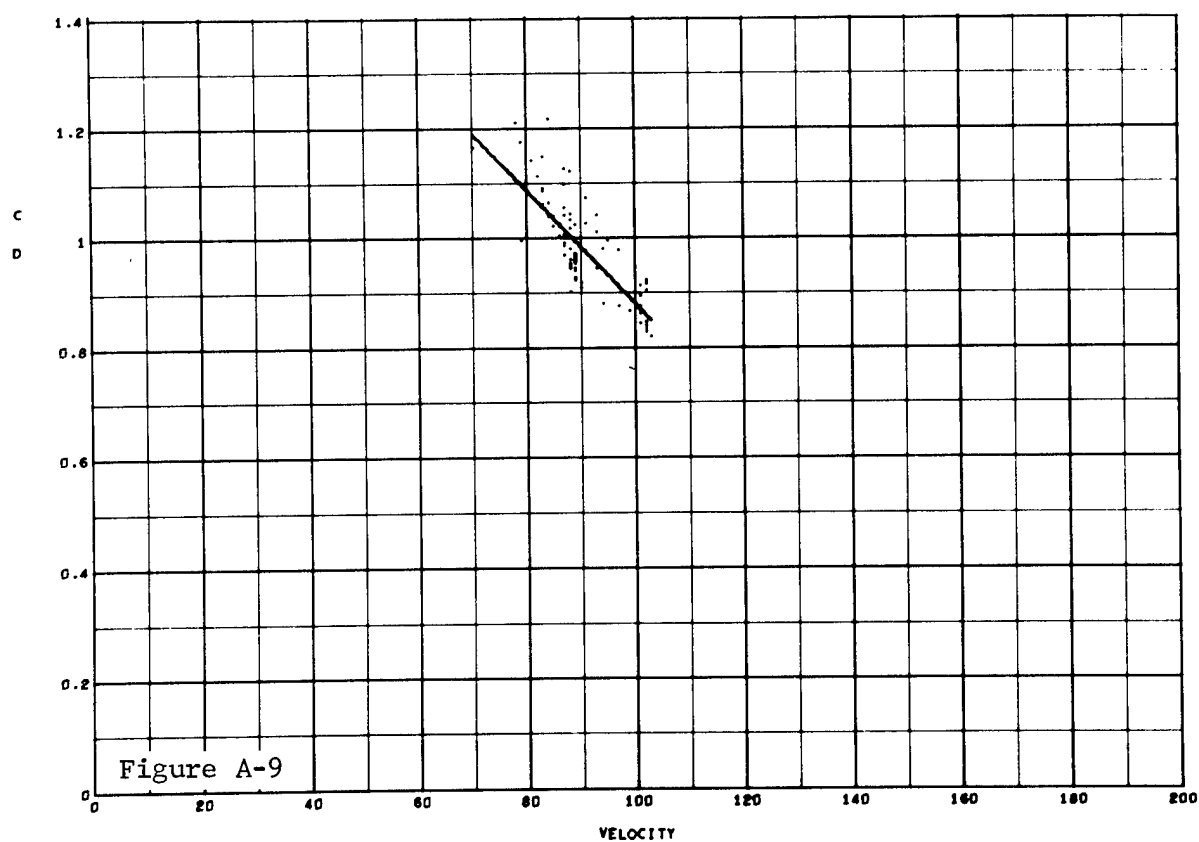
PASS 1 ZONE 1 TEST 250 13

DEGREE 1 LEAST SQUARES

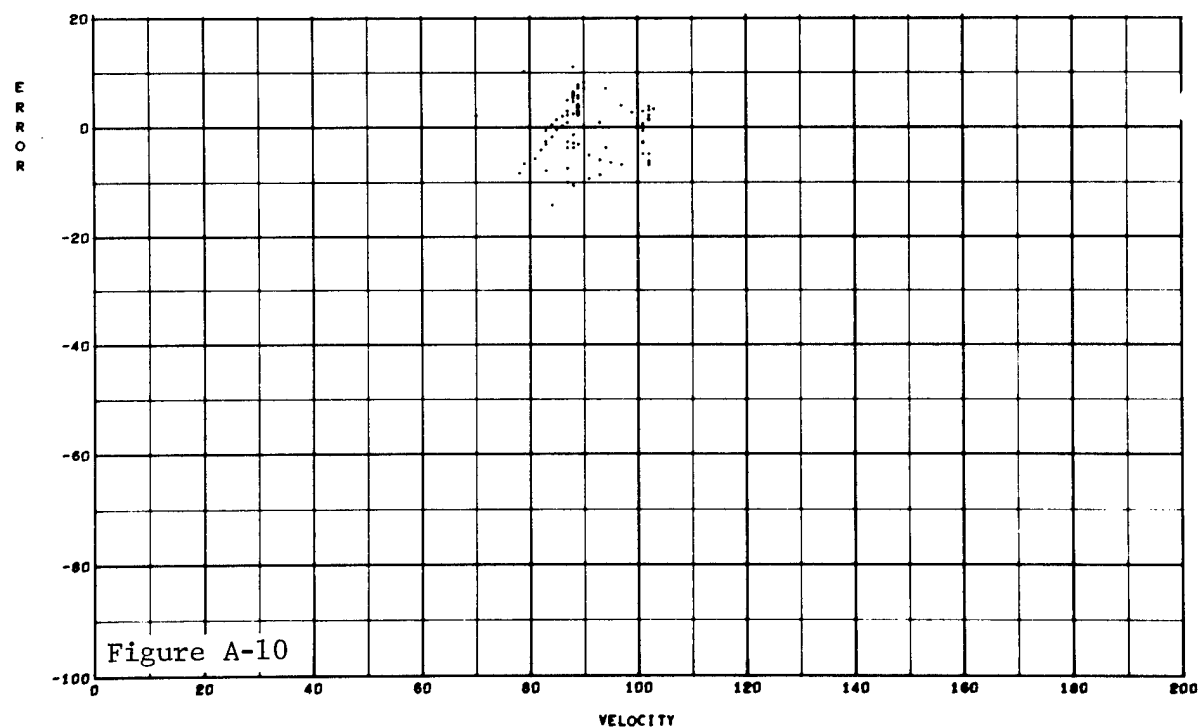


VELOCITY VS. ERROR

PASS 1 ZONE 1 TEST 250 13

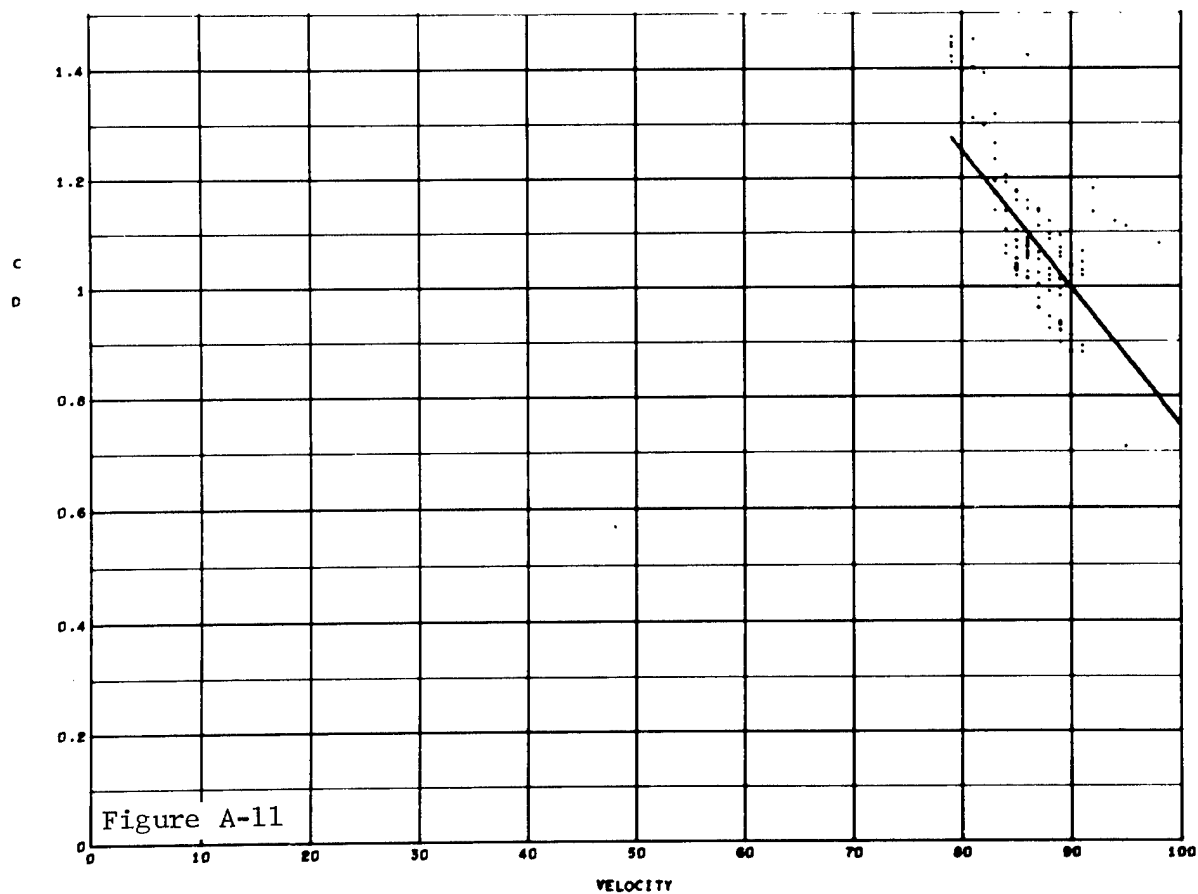


VELOCITY VS. C D      PASS 1    ZONE 1    TEST 258 14      DEGREE 1    LEAST SQUARES



VELOCITY VS. ERROR      PASS 1    ZONE 1    TEST 258 14

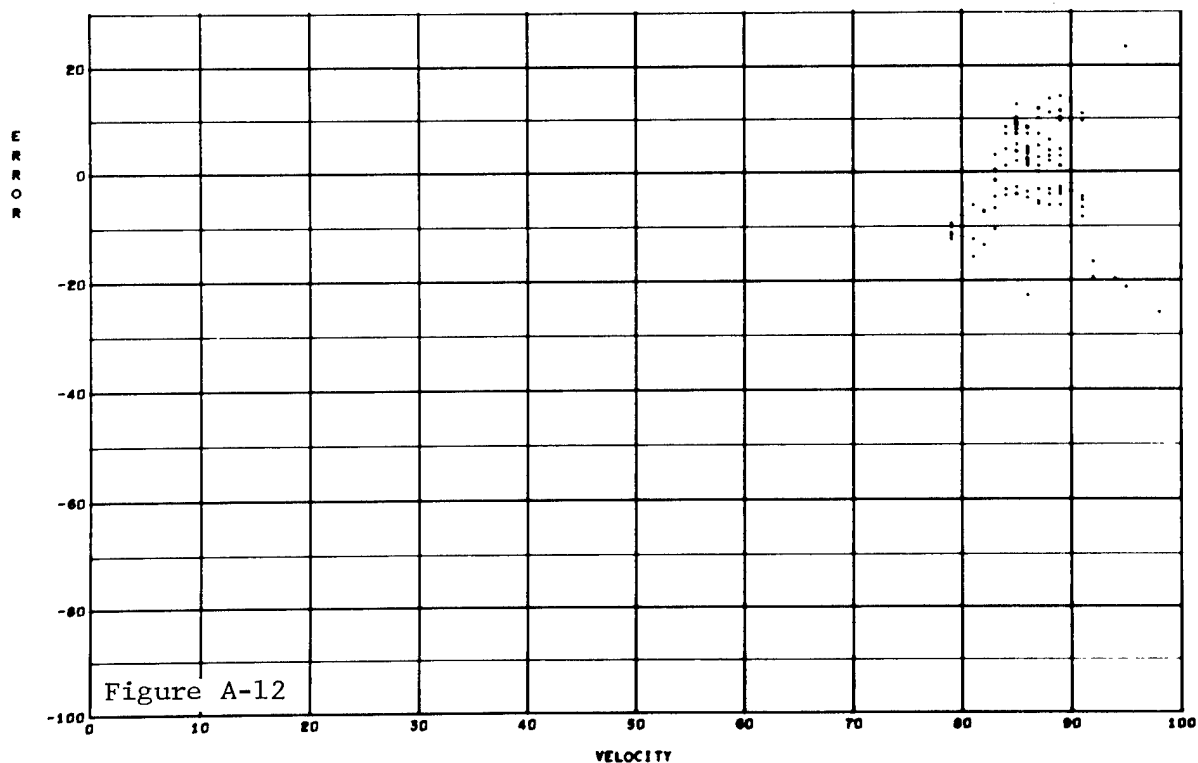




VELOCITY VS. C/D

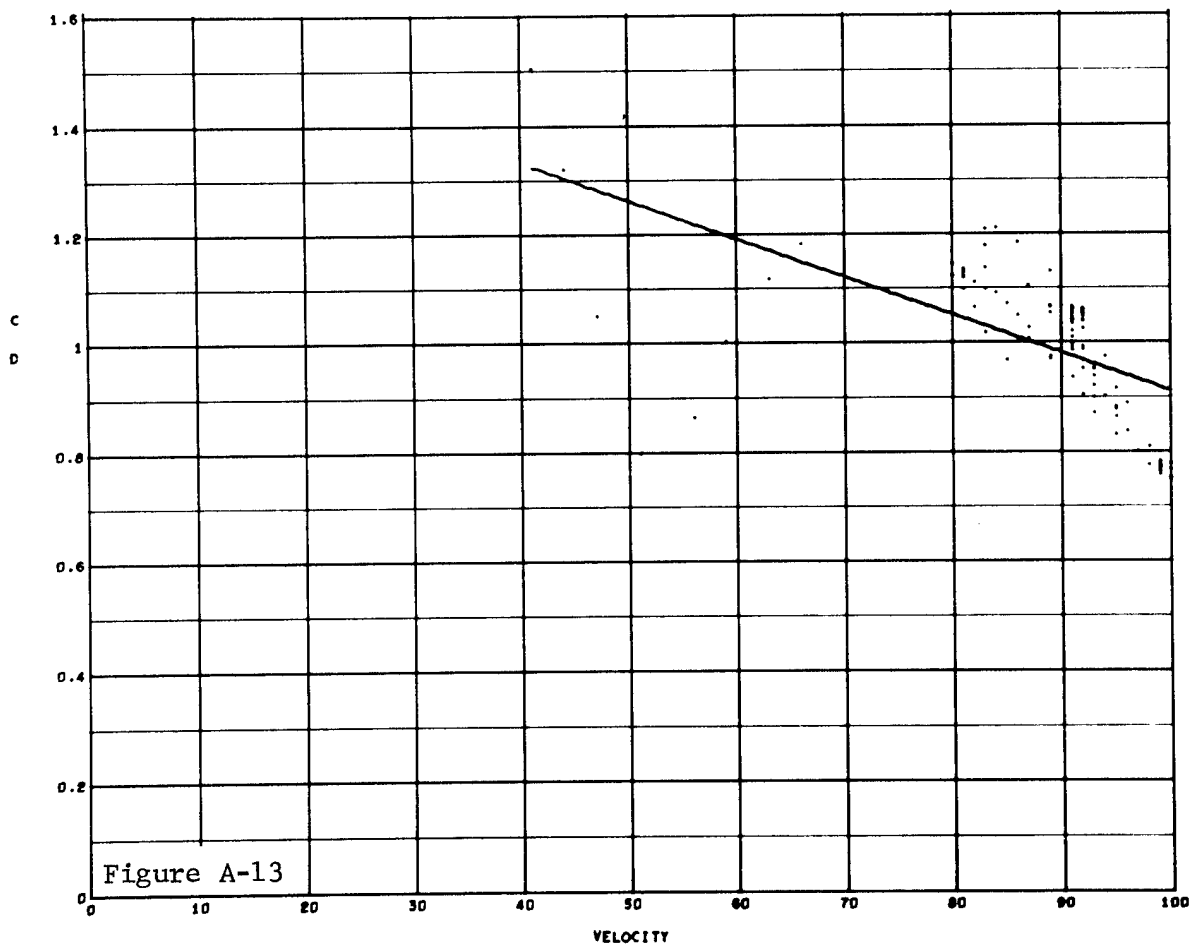
PASS 1 ZONE 1 TEST 250 15

DEGREE 1 LEAST SQUARES



VELOCITY VS. ERROR

PASS 1 ZONE 1 TEST 250 15



VELOCITY VS. C D

PASS 1 ZONE 1

TEST 258 16

DEGREE 1 LEAST SQUARES

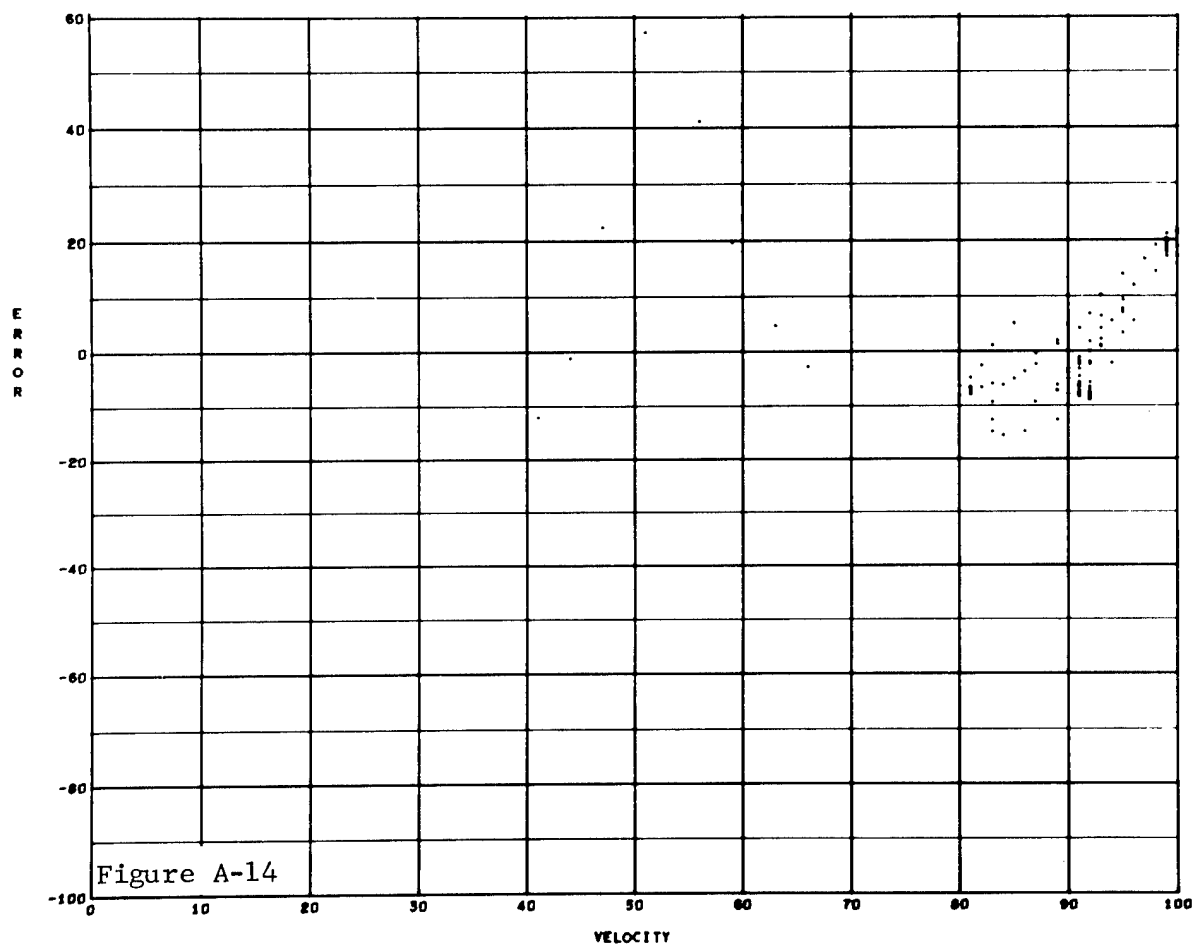
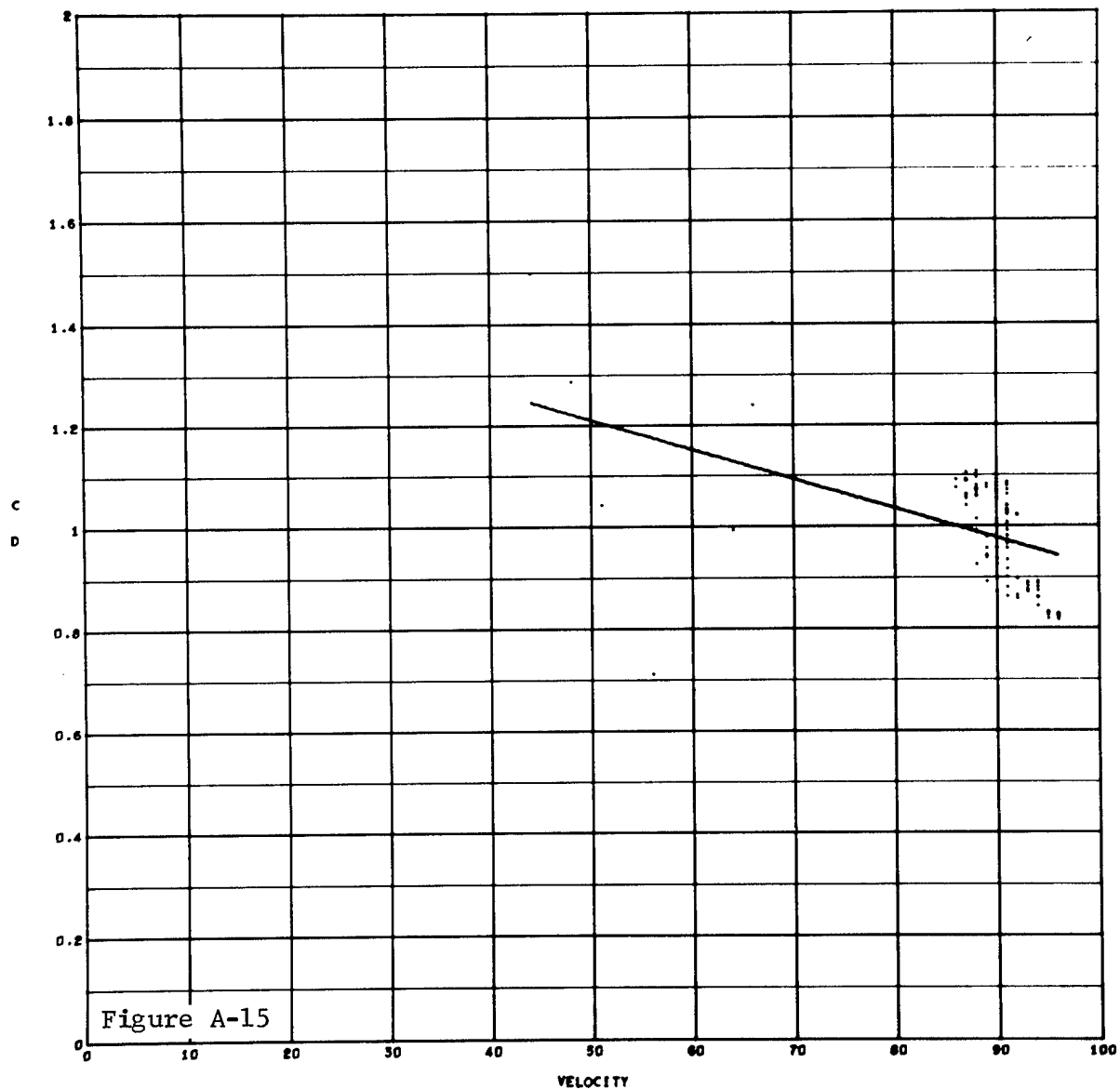


Figure A-14

VELOCITY VS. ERROR

PASS 1 ZONE 1 TEST 256 16



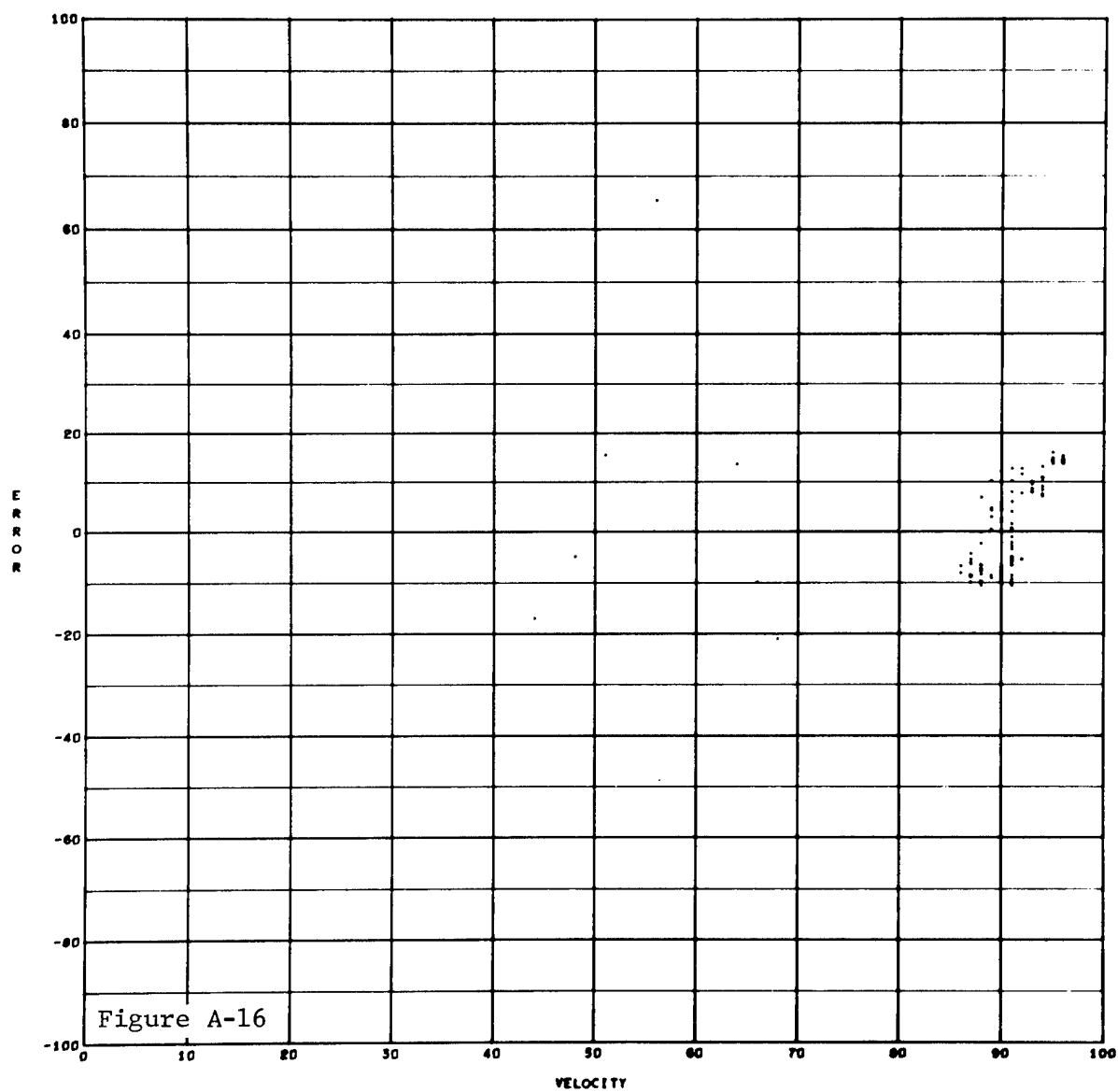
VELOCITY VS. C D

PASS 1 ZONE 1

TEST 250 17

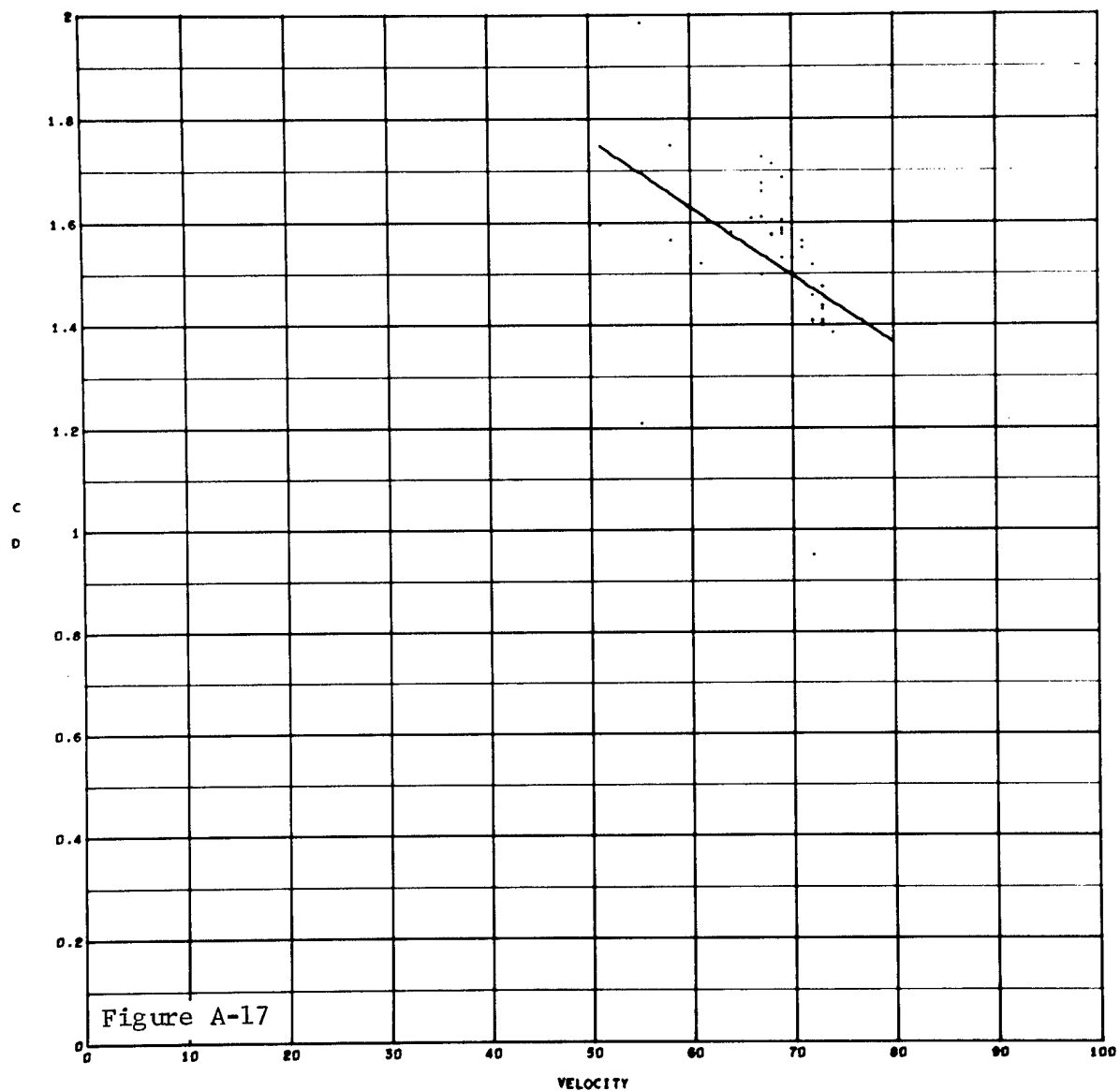
DEGREE 1

LEAST SQUARES



VELOCITY VS. ERROR

PASS 1 ZONE 1 TEST 258 17



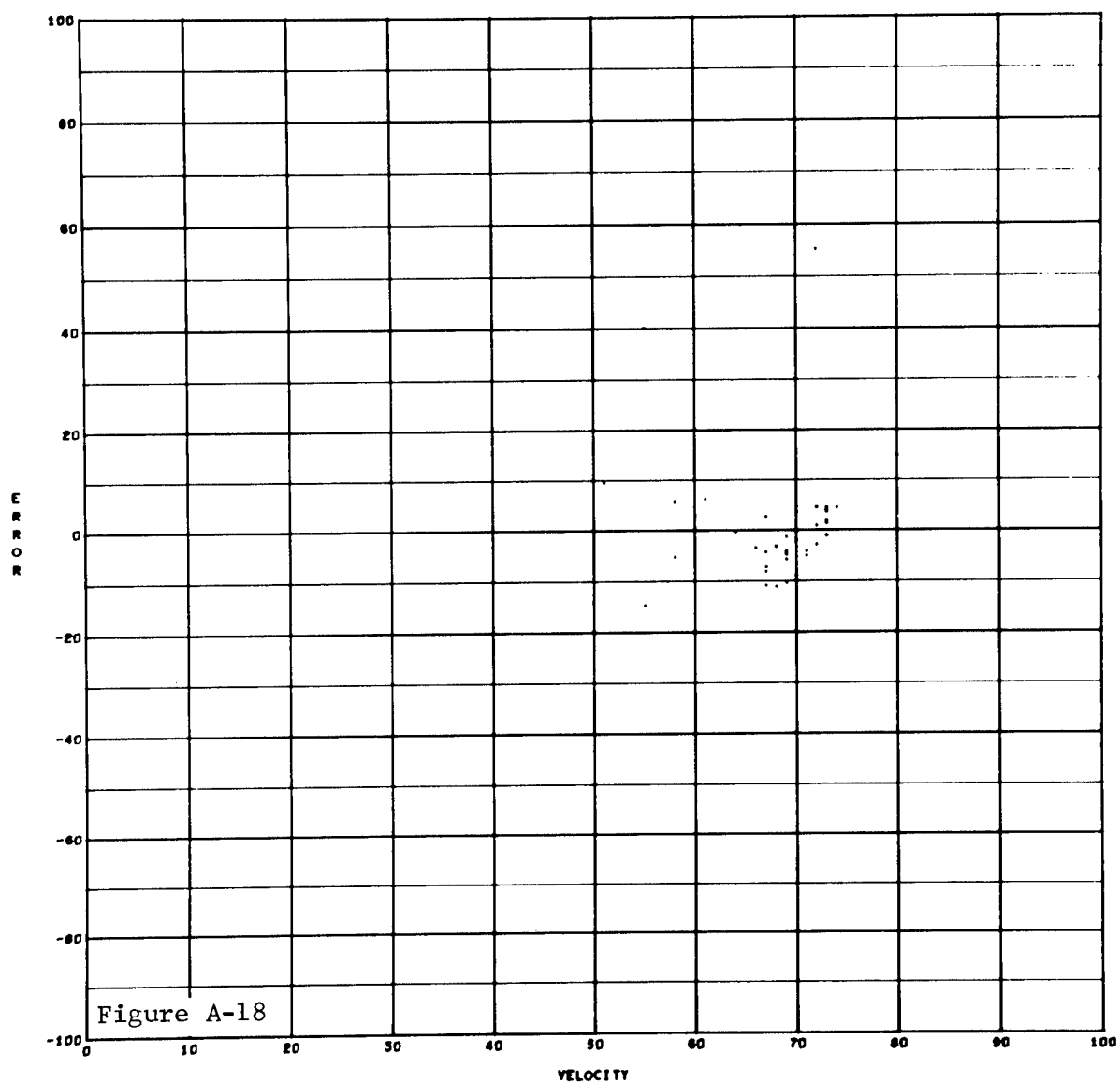
VELOCITY VS. C D

PASS 1 ZONE 1

TEST 250 10

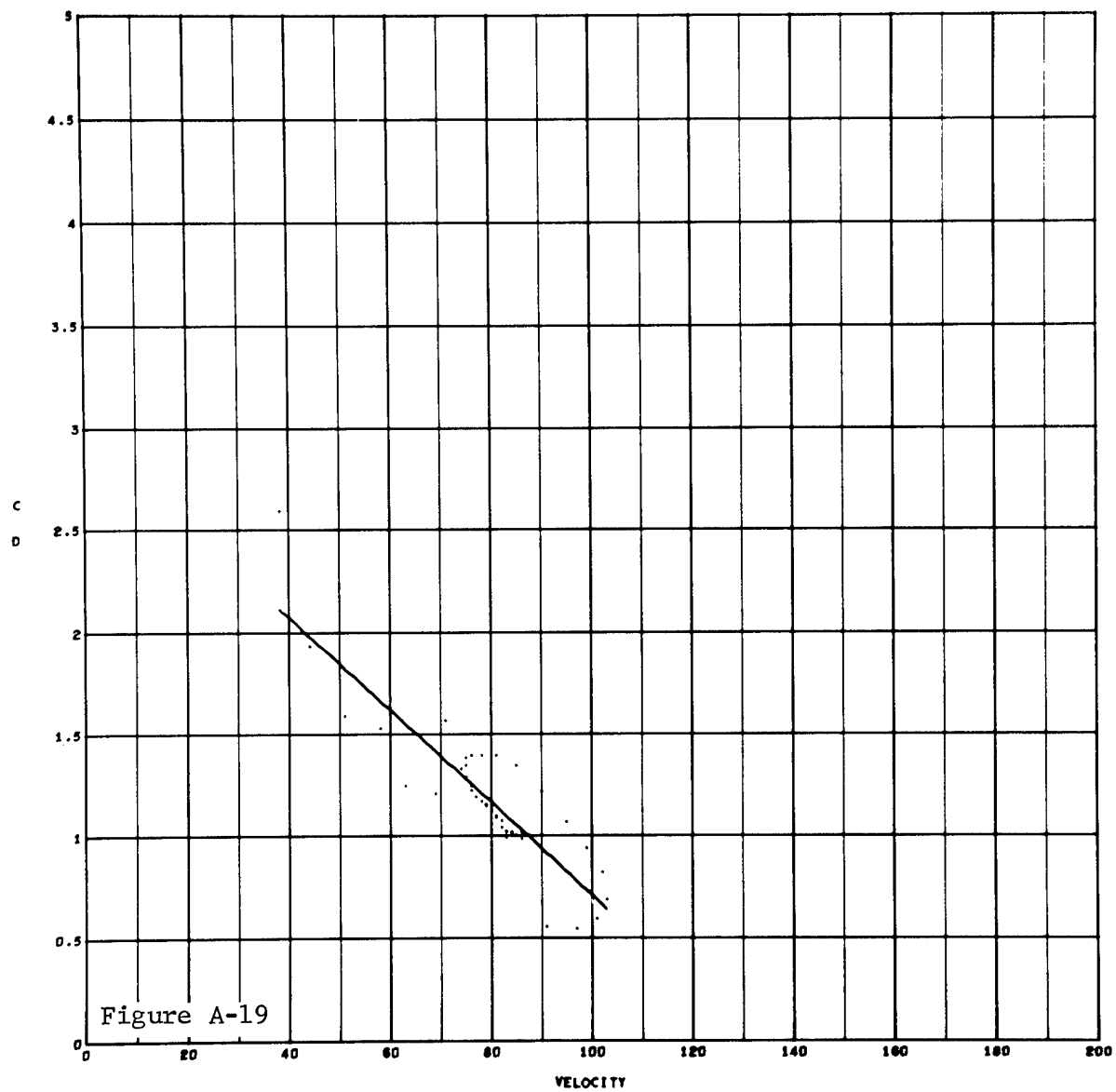
DEGREE 1

LEAST SQUARES



VELOCITY VS. ERROR

PASS 1 ZONE 1 TEST 258 18



VELOCITY VS. C D

PASS 1 ZONE 1 TEST 258 20

DEGREE 1 LEAST SQUARES



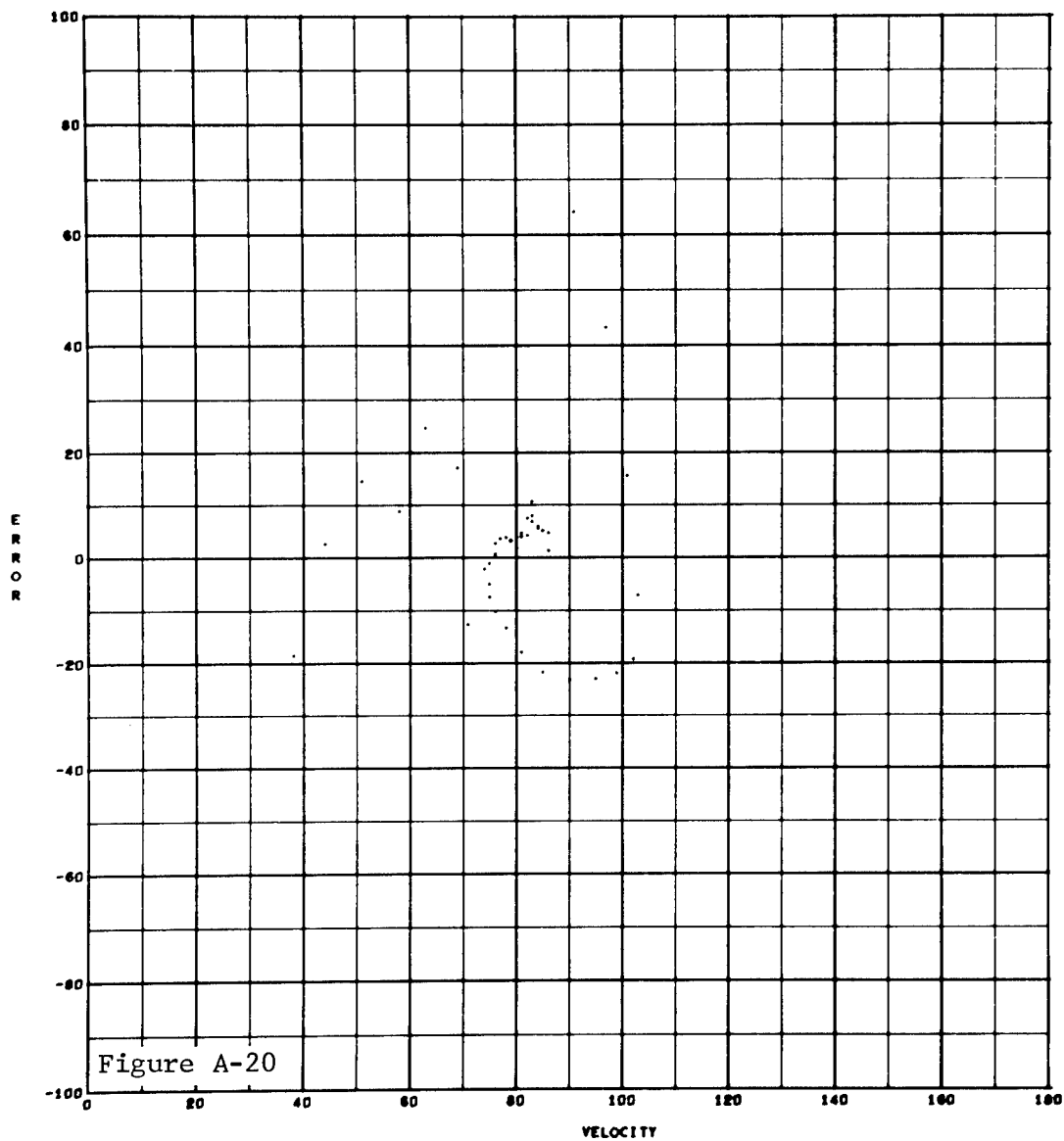
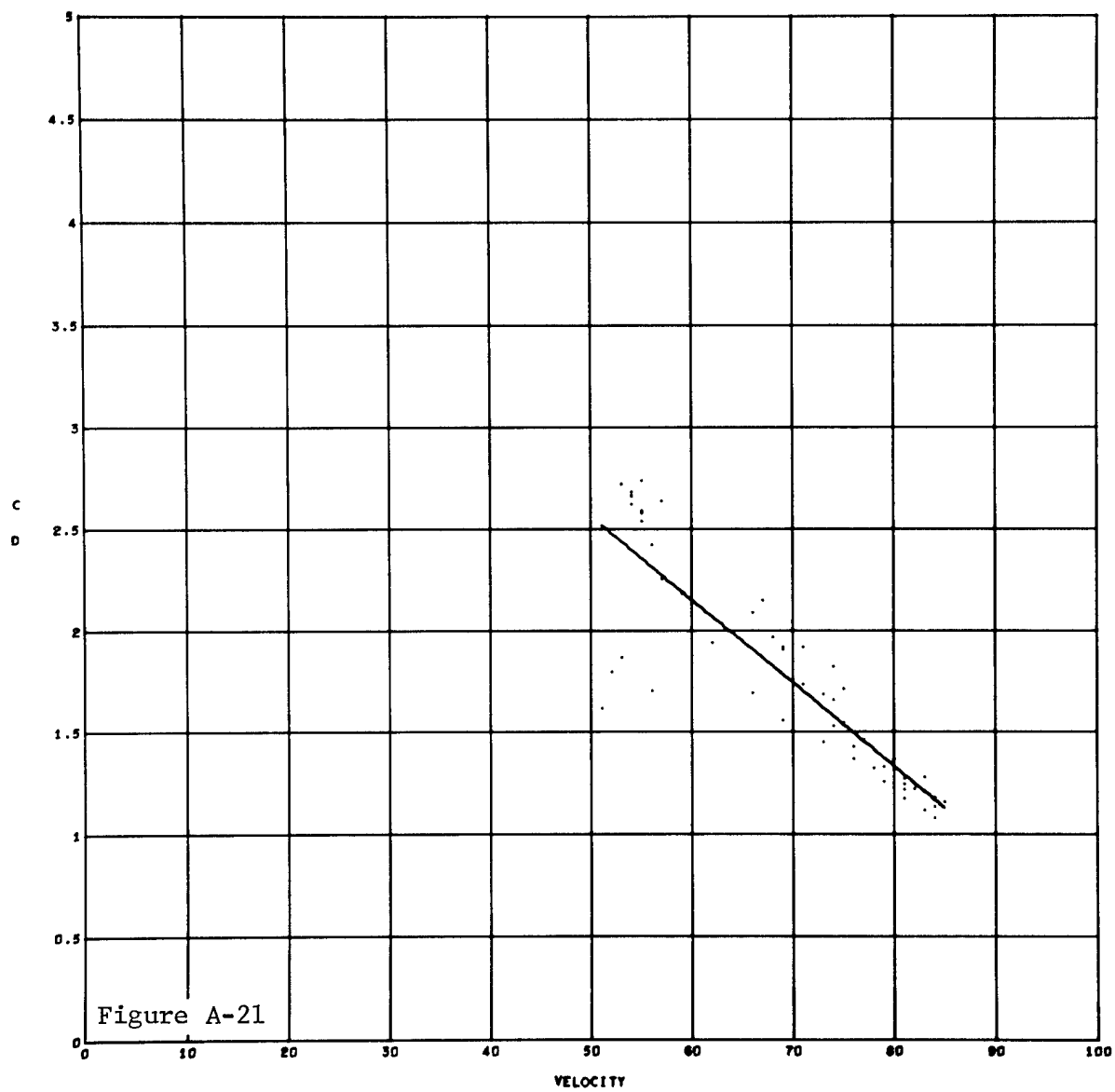


Figure A-20

VELOCITY VS. ERROR

PASS 1 ZONE 1 TEST 250 20



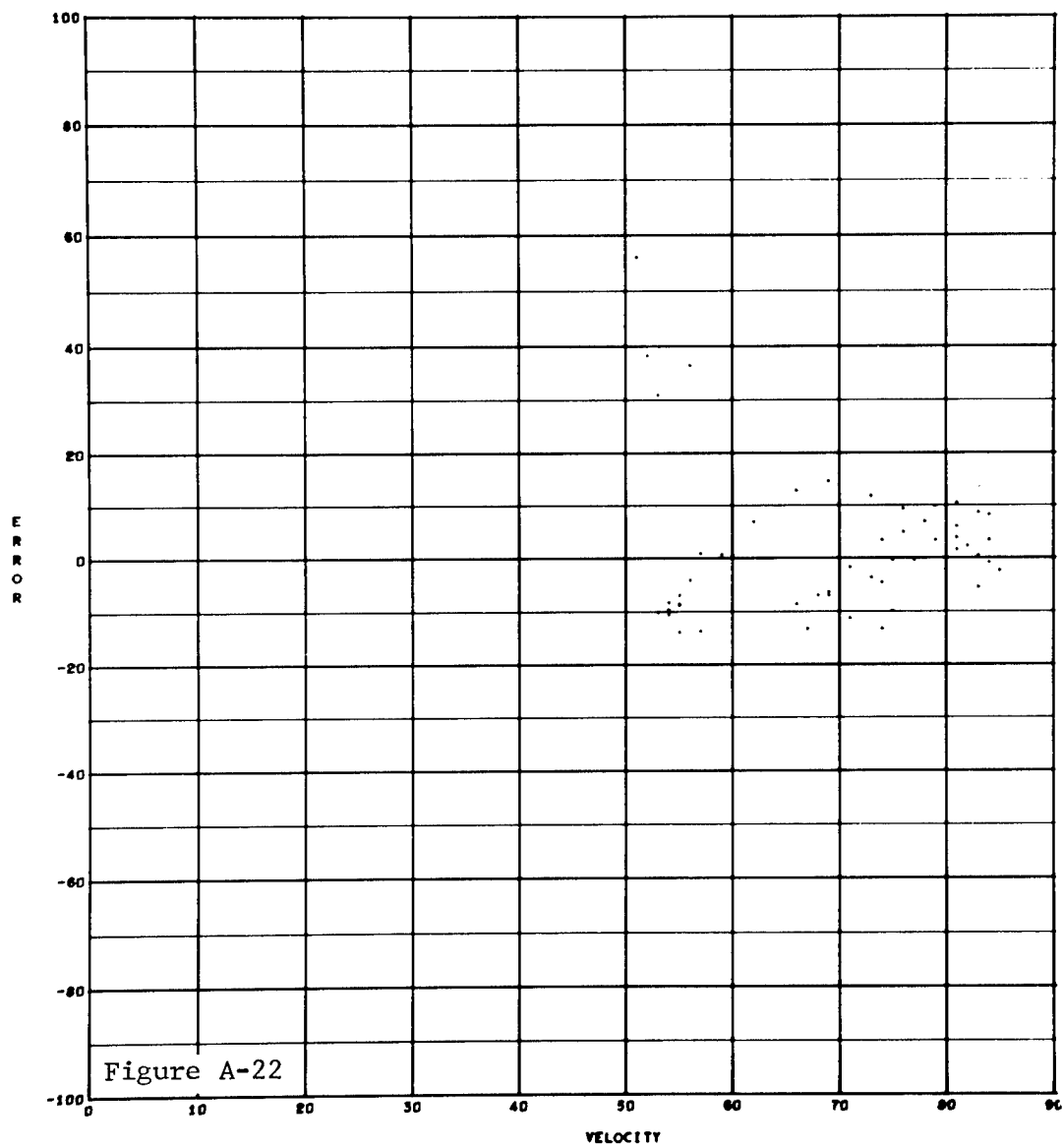
VELOCITY VS. C D

PASS 1 ZONE 1

TEST 250 21

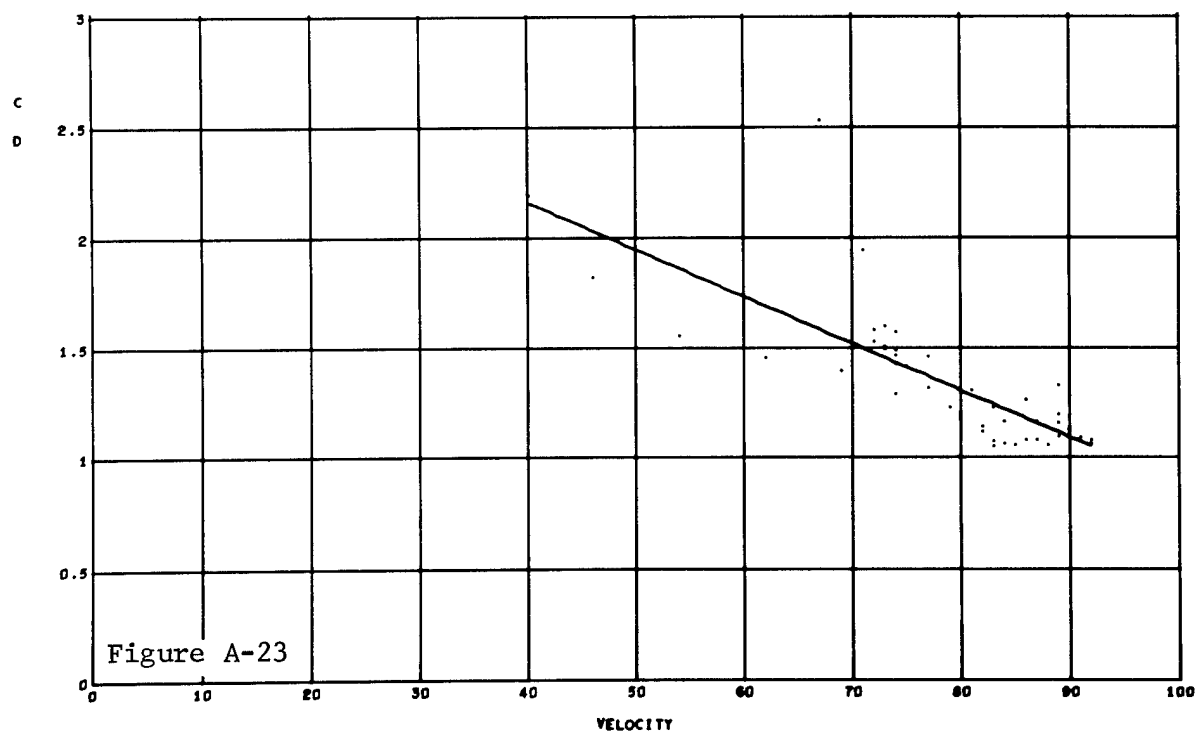
DEGREE 1

LEAST SQUARES



VELOCITY VS. ERROR

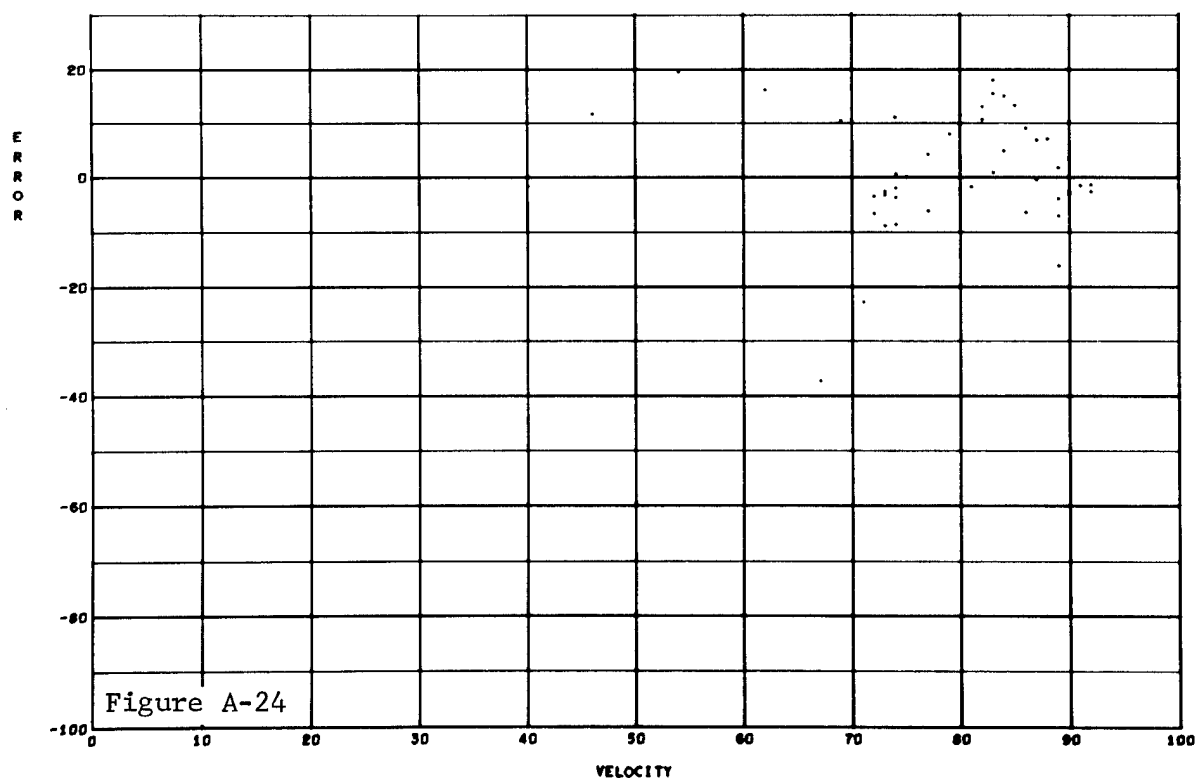
PASS 1 ZONE 1 TEST 256 21



VELOCITY VS. C D

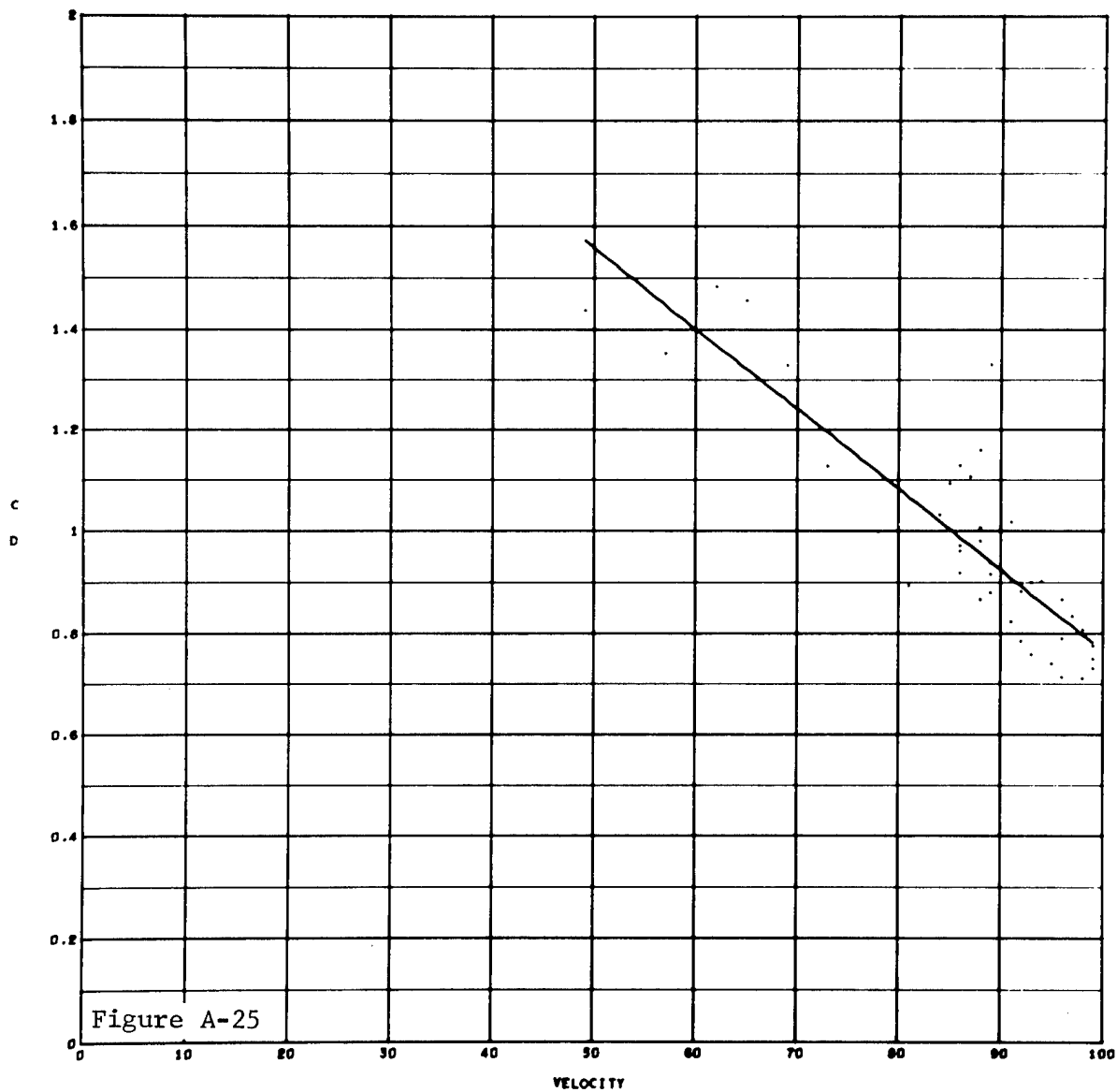
PASS 1 ZONE 1 TEST 258 23

DEGREE 1 LEAST SQUARES



VELOCITY VS. ERROR

PASS 1 ZONE 1 TEST 258 23



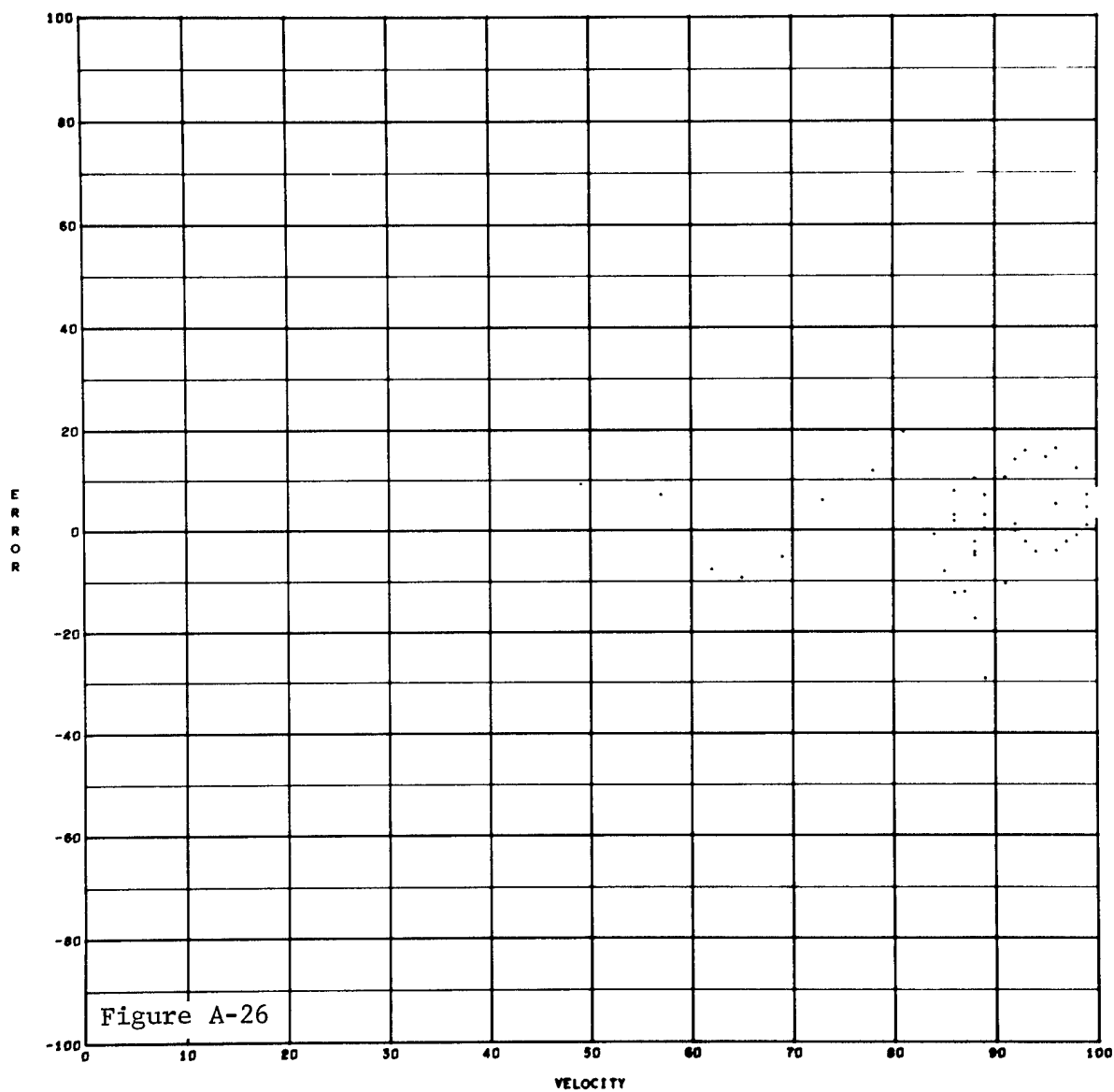
VELOCITY VS. C D

PASS 1 ZONE 1

TEST 250 24

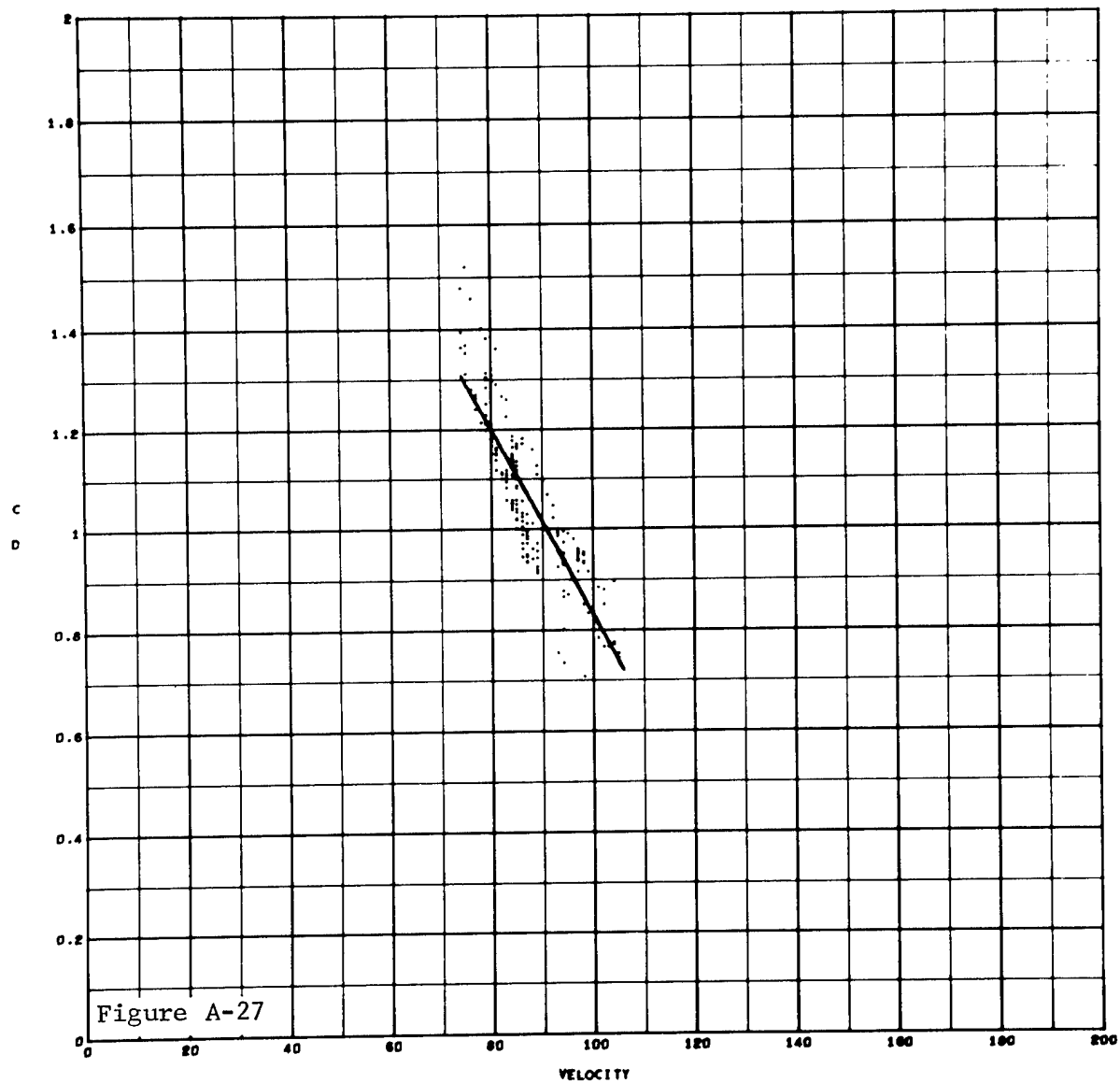
DEGREE 1

LEAST SQUARES



VELOCITY VS. ERROR

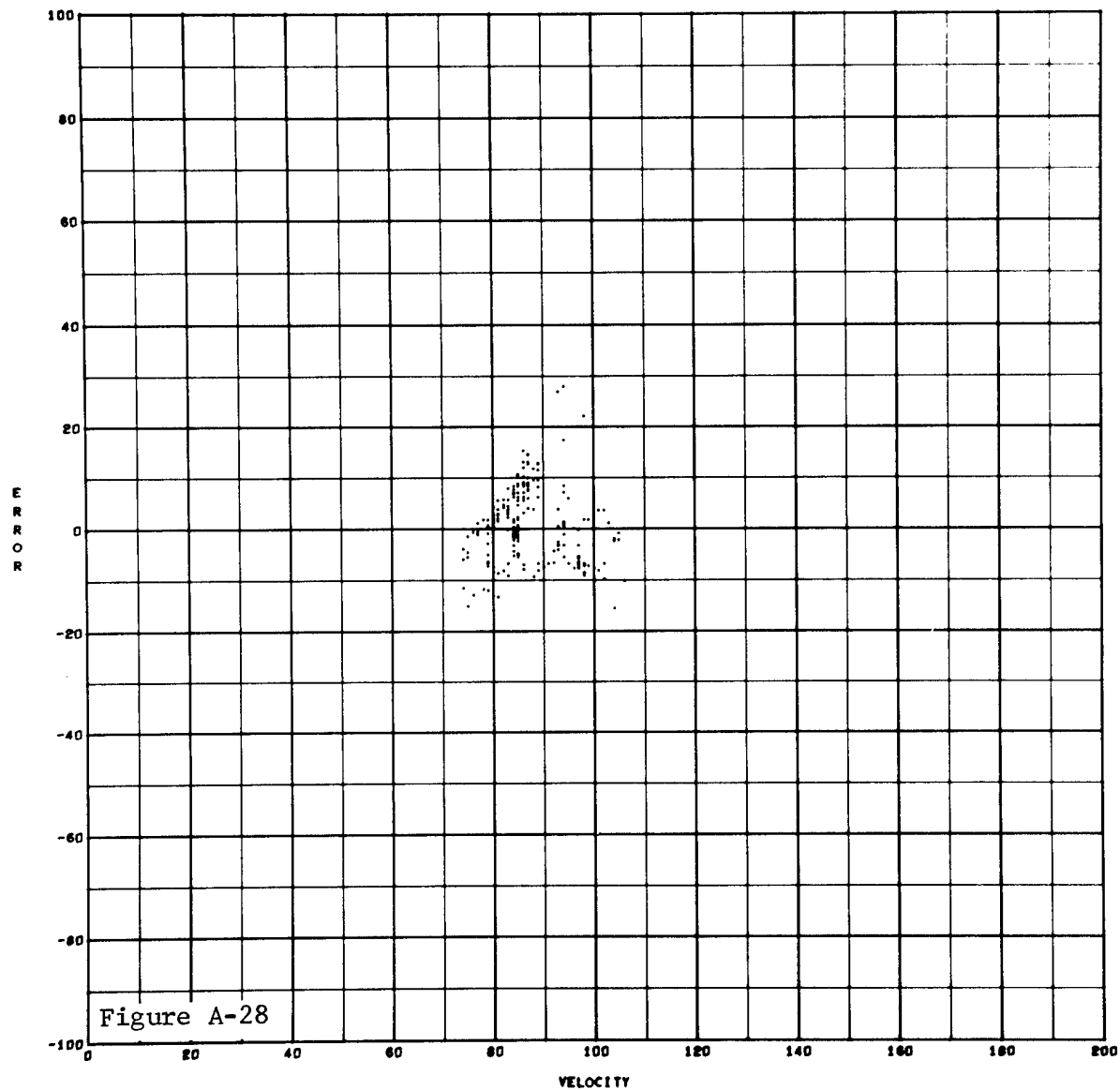
PASS 1 ZONE 1 TEST 258 24



VELOCITY VS. C/D

PASS 1 ZONE 1 TEST 250 25

DEGREE 1 LEAST SQUARES



VELOCITY VS. ERROR

PASS 1 ZONE 1 TEST 250 25



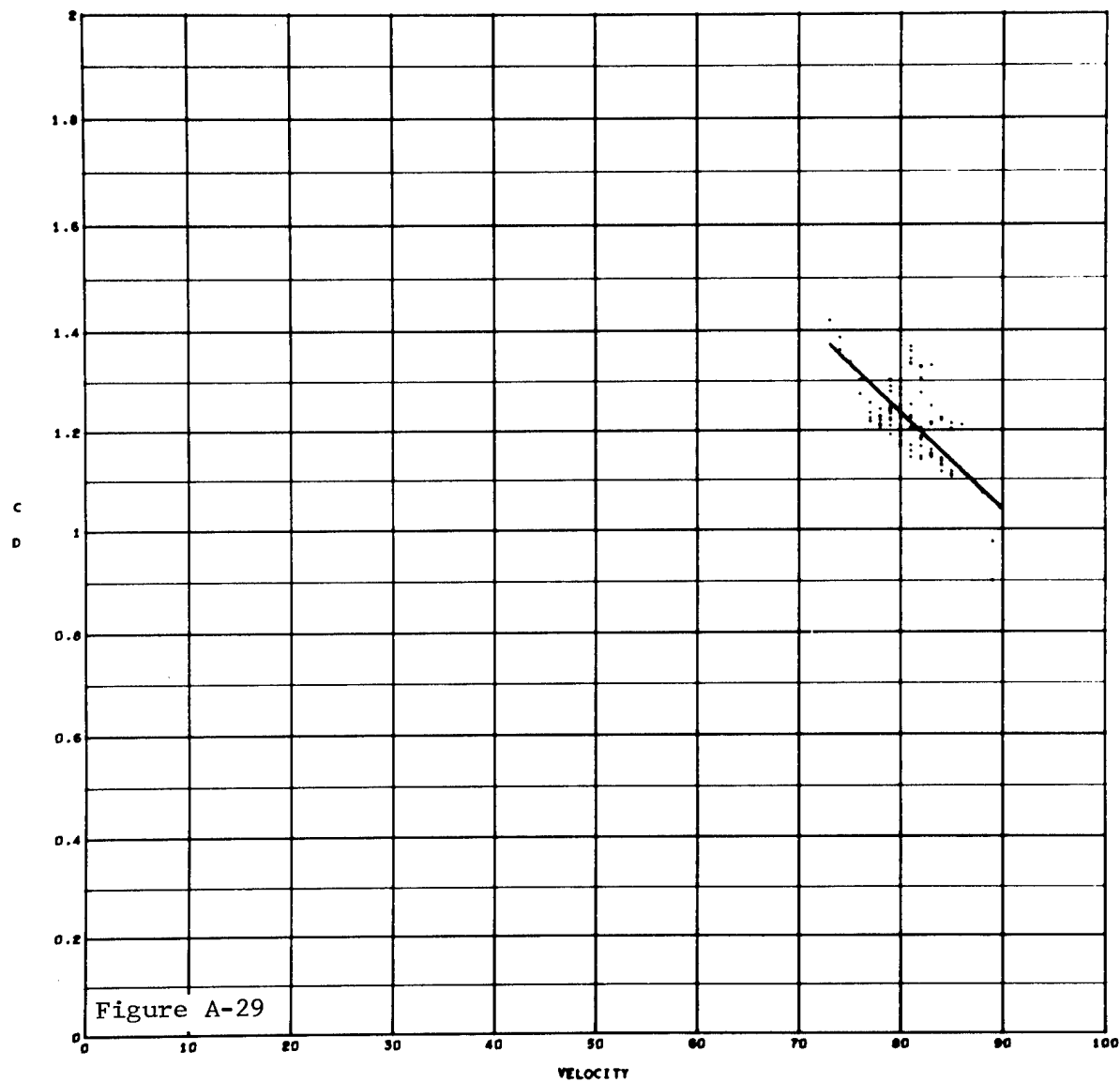


Figure A-29

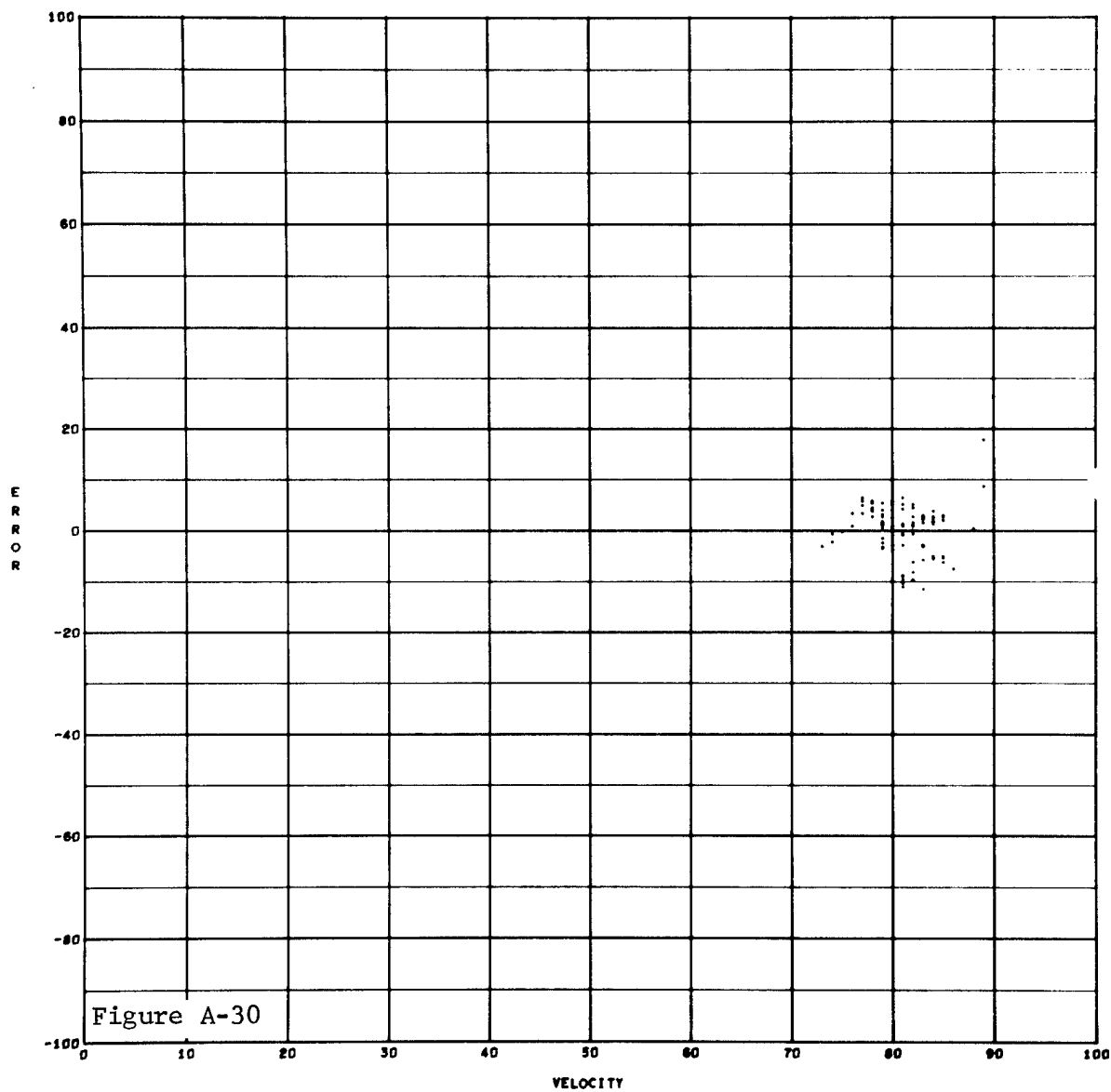
VELOCITY VS. C/D

PASS 1 ZONE 1

TEST 258 26

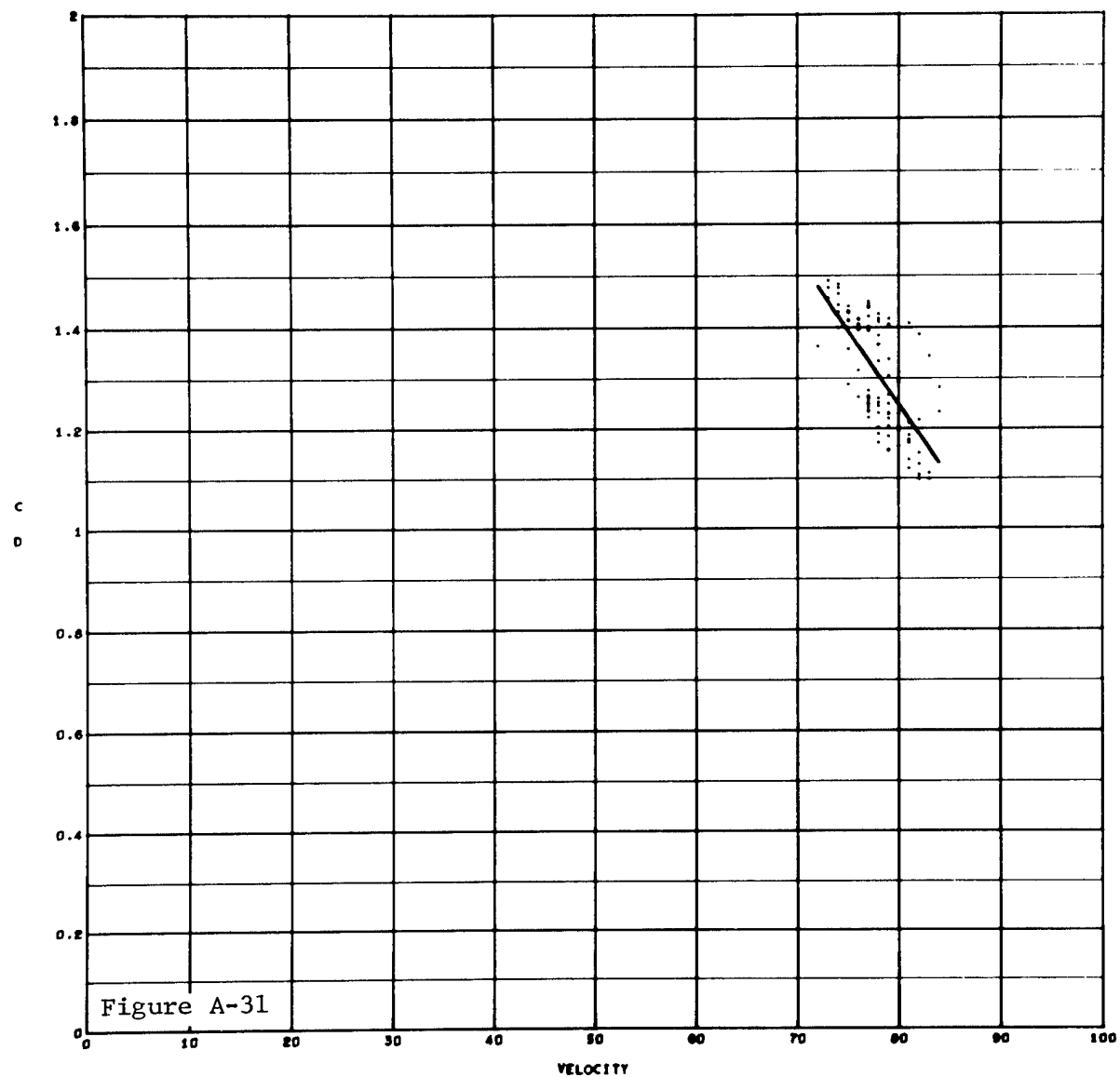
DEGREE 1

LEAST SQUARES



VELOCITY VS. ERROR

PASS 1 ZONE 1 TEST 258 26



VELOCITY VS. C/D

PASS 1 ZONE 1 TEST 250 27

DEGREE 1 LEAST SQUARES

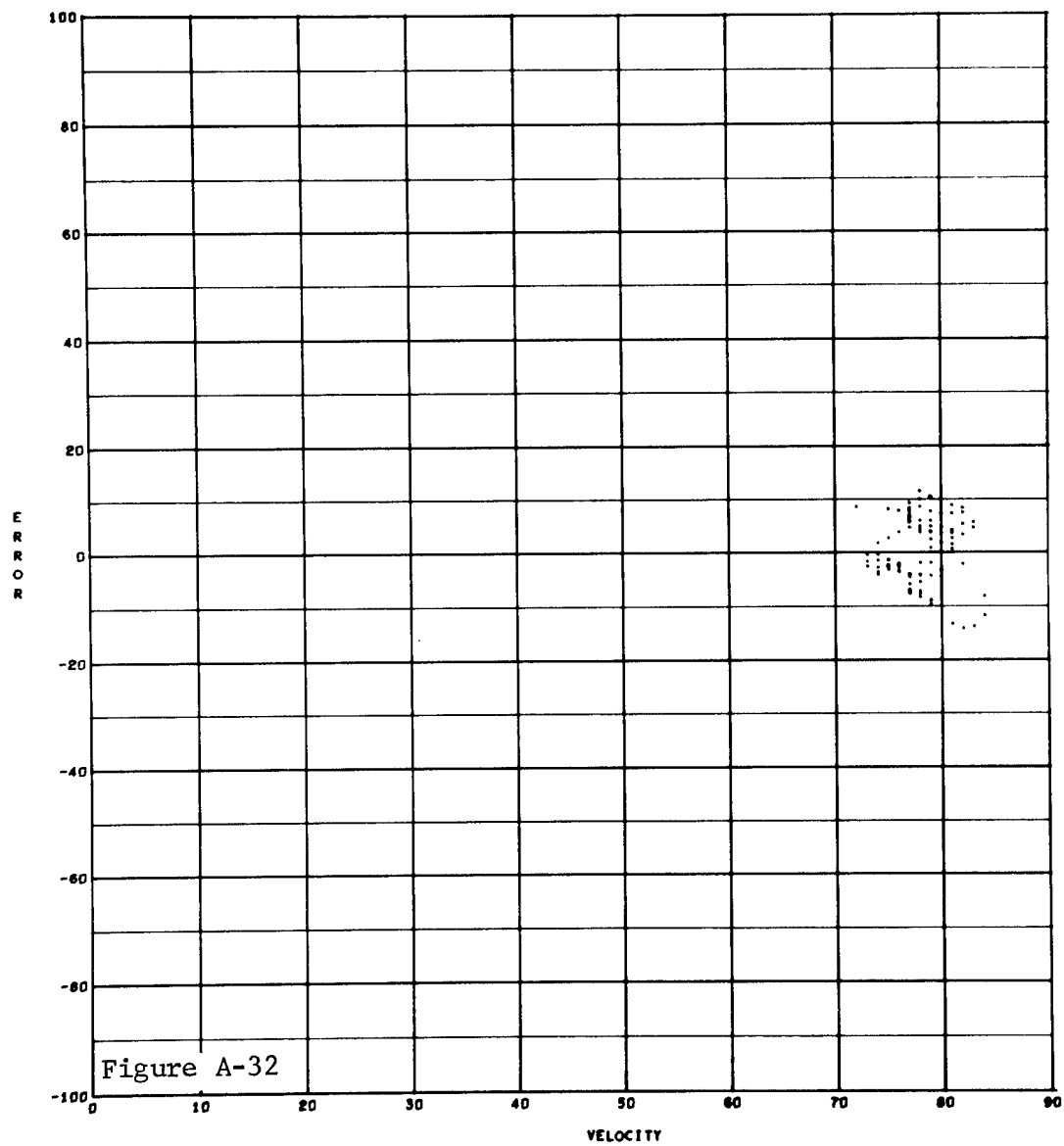


Figure A-32

VELOCITY VS. ERROR

PASS 1 ZONE 1 TEST 258 27

where the Q's are each polynomials which are orthogonal to each other. They are defined by a three-term recurrence relation:

$$Q_{K+1} = XQ_K(X) - \alpha_{K+1}Q_K(X) - \beta_{K+1}Q_{K-1}(X) \quad . \quad (A-3)$$

With  $Q_0(X) = 1$ ,

$$Q_1(X) = X - \alpha_1$$

$$\alpha_{K+1} = \frac{\sum_i X_i Q_K^2(X_i)}{\sum_i Q_K^2(X_i)} \quad (\text{sums over data points}) \quad (A-4)$$

$$\beta_{K+1} = \frac{\sum_i X_i Q_K(X_i) Q_{K-1}(X_i)}{\sum_i Q_{K-1}^2(X_i)} \quad .$$

Thus, the solution in this case yields not only a's but also the  $\alpha$ 's and  $\beta$ 's. This method is stable up through degree 50 (maximum allowed by the program).

Any zone, except the first, whose fit is made using the "normal" least-squares method may be constrained by forcing the value at a given point, and the derivative at that point, to be the values as determined by the curve in the previous zone. The mechanics for doing this involve the use of the Lagrange multipliers. Two functions, g and h, are defined as

$$g = A_0 + A_1 X_0 + A_2 X_0^2 + \dots + A_n X_0^n - Y_0 = 0 \quad (A-5)$$

$$h = A_1 + 2A_2 X_0 + 3A_3 X_0^2 + \dots + nA_n X_0^{n-1} - Y'_0 = 0 \quad , \quad (A-6)$$

where  $Y_0$  is the value at  $X_0$  defined by polynomial over the previous zone.  $Y'_0$  is the derivative defined in same manner.

The function to be minimized is then assumed to be

$$G = f + 2\lambda g + 2\mu h \quad , \quad (A-7)$$

where  $\lambda$  and  $\mu$  are the Lagrange multipliers. The system of equations in  $A_K, \lambda$ , and  $\mu$  are generated in the normal manner. These, together with

Eqs. (A-6) and (A-7) are solved, and the resulting A's are the coefficients to the constrained polynomial. Although  $\lambda$  and  $\mu$  are solved for, they are used only in the formulation and not in the evaluation of the resultant polynomial. It is noted that the previous zone may have been fitted using either "normal" or orthogonal techniques.

Zone determination may be assisted by Figure A-33. Although it is only a rough indication, acceptable results have been obtained using this scheme on all data sets tested.

The error determination is defined as

$$E = \frac{Y_i - Y(X_i)}{Y(X_i)}, \quad (A-8)$$

where  $Y(X_i)$  is the data value and  $Y_i$  is the computed value using the fitted polynomial.

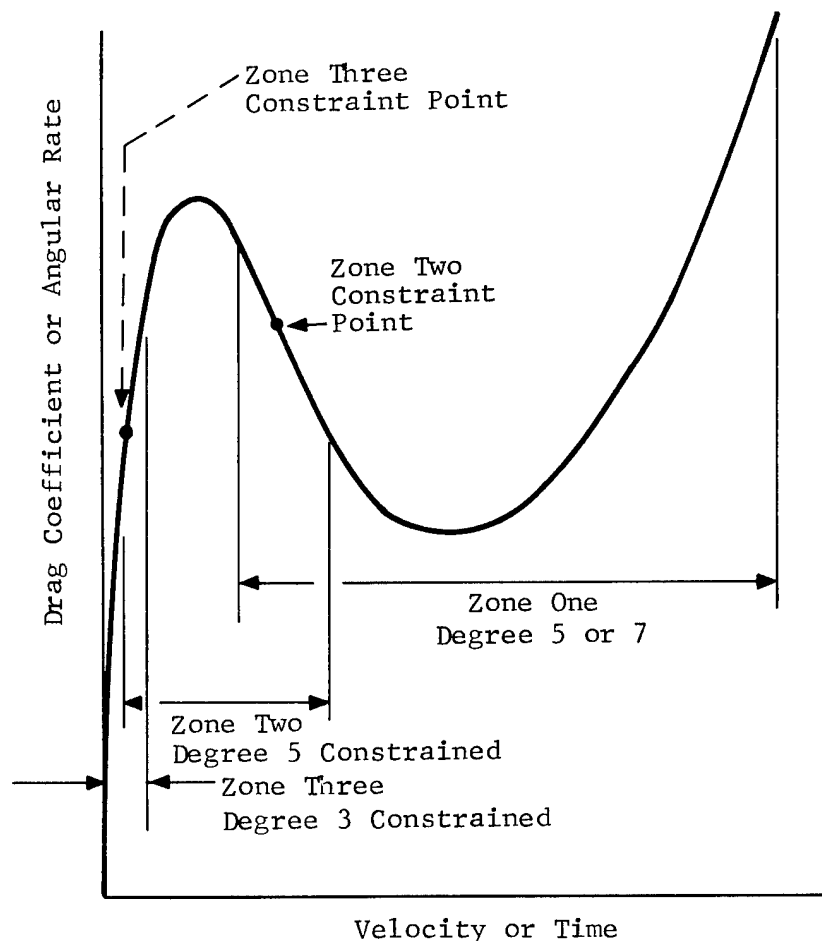


Figure A-33. Illustration of curve fit technique

DISTRIBUTION:

TID-4500 (52 Ed.) UC-36 (201)

U. S. Atomic Energy Commission  
Division of Space Nuclear Systems  
Space Electric Power Office  
Washington, D. C. 20545

Attn: G. A. Newby  
Assistant Director (1)  
G. P. Dix, Chief  
Safety Branch (1)  
R. T. Carpenter, Chief  
Isotope Power Systems Branch (1)  
J. A. Powers, Chief  
Isotopes and Materials Branch (1)  
C. Johnson, Chief  
Reactor Power Systems Branch (1)

U. S. Atomic Energy Commission  
Space Nuclear Propulsion Office  
Washington, D. C. 20545  
Attn: R. S. Decker, Jr.  
Chief, Safety Branch

U. S. Atomic Energy Commission  
Division of Isotope Development  
Washington, D. C. 20545

U. S. Atomic Energy Commission  
Director of Regulation  
Washington, D. C. 20545  
Attn: C. K. Beck  
Deputy Director (1)  
F. D. Anderson  
Regulation (1)

U. S. Atomic Energy Commission  
Division of Biology and Medicine  
Washington, D. C. 20545  
Attn: J. Z. Holland, Chief  
Fallout Studies Branch (1)  
H. D. Bruner, Asst. Director  
Medical and Health Research (1)

U. S. Atomic Energy Commission  
Space Nuclear Propulsion Office  
Albuquerque Extension  
Albuquerque Operations Office  
P. O. Box 5400  
Albuquerque, New Mexico 87115  
Attn: H. P. Smith

U. S. Atomic Energy Commission  
Albuquerque Operations Office  
P. O. Box 5400  
Albuquerque, New Mexico 87115  
Attn: S. A. Upson, Director  
Non-Nuclear Activities Division (1)  
J. F. Burke, Director  
Operational Safety Division (1)

DISTRIBUTION: (cont)

Atomic Energy Commission  
Site Representative  
National Aeronautics and Space  
Administration  
Manned Spacecraft Center  
Houston, Texas 77058  
Attn: W. C. Remini, Bldg. 16, Code ZS-5

Donald W. Douglas Laboratories  
P. O. Box 310  
Richland, Washington 99352  
Attn: S. P. Gydesen

Douglas Aircraft Company  
Missile & Space Systems Division  
3000 Ocean Park Blvd.  
Santa Monica, California  
Attn: Sig Gronich  
Advanced Space Technology

Deputy I. G. for Insp. & Safety  
USAF, Kirtland Air Force Base  
New Mexico 87117  
Attn: Col. D. C. Jameson (AFINSR)

General Electric Company  
Valley Forge Space Technology Center  
P. O. Box 8555  
Philadelphia, Pennsylvania 19101  
Attn: S. M. Scala, Room M9539  
Space Sciences Lab (1)  
G. W. Rivenbark  
Isotope Power Systems  
Operations (1)

Los Alamos Scientific Laboratory  
P. O. Box 1663  
Los Alamos, New Mexico 87544  
Attn: Dr. L. D. P. King (1)  
Dr. Wright Langham (1)  
C. F. Metz, CMB-1 (1)  
F. W. Schonfeld, CMF-5 (1)  
J. A. Leary, CMB-11 (1)

Isotopes  
Nuclear Systems Division  
P. O. Box 4937  
Middle River, Md. 21220

Monsanto Research Corporation  
Mound Laboratory  
P. O. Box 32  
Miamisburg, Ohio 45342  
Attn: G. R. Grove

Thomas B. Kerr  
Code RNS  
National Aeronautics and Space  
Administration  
Washington, D. C. 20545



DISTRIBUTION: (cont)

National Aeronautics and Space  
Administration

Ames Research Center  
Moffet Field, California  
Attn: Glenn Goodwin

National Aeronautics and Space  
Administration  
Goddard Space Flight Center  
Glenn Dale Road  
Greenbelt, Maryland 20771  
Attn: A. W. Fihelly, Nimbus Project

Dr. D. W. Sherwood  
National Aeronautics and Space  
Administration  
Manned Spacecraft Center (MSC-TD)  
Houston, Texas 77058

U. S. Naval Radiological Defense  
Laboratory  
San Francisco, California 94135  
Attn: S. Z. Mikhail  
Nuclear Systems Group

Naval Facilities Engineering Command  
Department of the Navy, Code 042  
Washington, D. C. 20390  
Attn: Graham Hagey

Space Nuclear Propulsion Office  
Lewis Research Center  
21000 Brookpark Road  
Cleveland, Ohio 44135  
Attn: L. Nichols

TRW Systems  
P. O. Box 287  
Redondo Beach, California 90278  
Attn: Dr. Donald Jortner

Union Carbide Corporation  
Nuclear Division  
P. O. Box X  
Oak Ridge, Tennessee 37831  
Attn: R. A. Robinson  
Isotope Development Center (1)  
B. R. Fish  
Health Physics Division (1)

U. S. Public Health Service  
Nat. Ctr. For Radiological Health  
1901 Chapman Avenue  
Rockville, Maryland 20852  
Attn: Nuclear Facilities Section

Jet Propulsion Laboratory  
California Insti. of Tech.  
4800 Oak Grove Drive  
Pasadena, California 91103  
Attn: A. L. Klascius  
Radiation Health and Safety

DISTRIBUTION: (cont)

D. B. Shuster, 1200  
J. R. Banister, 5270  
J. D. Shreve, 5271  
W. V. Hereford, 7216  
L. E. Lamkin, 7300  
G. A. Fowler, 9000  
H. E. Viney, 9130  
A. Y. Pope, 9300  
R. C. Maydew, 9320  
K. J. Touryan, 9340  
L. A. Hopkins, Jr., 9500  
V. E. Blake, 9510  
H. E. Hansen, 9511  
S. L. Jeffers, 9512  
G. H. Elkins, 9512 (2)  
S. McAlees, Jr., 9513  
A. C. Bustamante, 9513 (10)  
J. D. Appel, 9514  
J. D. Appel, 9514 (ARPIC) (2)  
R. J. Everett, 9515  
A. J. Clark, 9520  
J. W. McKiernan, 9521  
J. Jacobs, 9522  
B. F. Hefley, 8232 (5)  
B. R. Allen, 3421  
C. H. Sproul, 3428-2 (10)  
L. C. Baldwin, 3412 (2)  
L. L. Alpaugh, 3412  
W. J. Wagoner, 3413